STUDY OF THE MATERIALS BELONGING TO THE SYSTEM $La_4BaCu_{5-x}M_xO_{13\pm\delta}$ (M: Co, Mn) WITH POTENTIAL APPLICATION AS ELECTRODE ON SOLID OXIDE FUEL CELLS (SOFC)

SILVIA ALEJANDRA DURAN AMAYA

UNIVERSIDAD INDUSTRIAL DE SANTANDER
FACULTAD DE INGENIERÍAS FÍSICO-QUÍMICAS
ESCUELA DE INGENIERÍA METALÚRGICA Y CIENCIA DE MATERIALES
MAESTRÍA EN INGENIERÍA DE MATERIALES
BUCARAMANGA
2018

STUDY OF THE MATERIALS BELONGING TO THE SYSTEM $La_4BaCu_{5-x}M_xO_{13\pm\delta}$ (M: Co, Mn) WITH POTENTIAL APPLICATION AS ELECTRODE ON SOLID OXIDE FUEL CELLS (SOFC)

SILVIA ALEJANDRA DURAN AMAYA

Thesis submitted to obtain the degree of Master in Materials Engineering

Thesis Advisor: Ph. D. GILLES H. GAUTHIER
Co-Advisor: Ph. D. LEOPOLDO SUESCUN

UNIVERSIDAD INDUSTRIAL DE SANTANDER
FACULTAD DE INGENIERÍAS FÍSICO-QUÍMICAS
ESCUELA DE INGENIERÍA METALÚRGICA Y CIENCIA DE MATERIALES
MAESTRÍA EN INGENIERÍA DE MATERIALES
BUCARAMANGA
2018

ACKNOWLEDGEMENTS

A hearty thanks to my mom “my engine”, my brother “bola”, my father, my whole family, and to my boyfriend Cristian, for their deeply love and support through this process.

Special thanks to Dr. Gilles Gauthier (*Profe*) for giving me the opportunity to work with him, his patience, guidance and knowledge, as well as his constant support to achieve this goal and make possible the development of this research. Made me grow professionally and allowed me to love more the research. I also deeply thank Dr. Leopoldo Suescun (*Leo*) for his contributions and to make his laboratory available to me, as well as for his patience and guidance.

I also thank to Dr. Konrad Świerczek and his students for make me or making me feel comfortable being so far from home. Thanks to all the people that is behind technical assistance. I also need to mention “my undergraduate students” at the moment Nathaly Rangel, Maria Camila Silva and Jhoan Francisco Tellez who helped me enormously in experimental development and also for all the hard work and funny moments at the lab.

I appreciate the whole research group INTERFASE for opening the doors and for their contributions in the development of this project, the collaboration of Unité de Catalyse et Chimie du Solide (UCCS), Laboratorio de Difracción de Rayos X (Parque Tecnológico Guatiguará-UIS) and CRYSSMAT-LAB which were fundamental for the experimental development of this thesis. I also thank the financial support of the Vicerrectoría de Investigación y Extensión of the Universidad Industrial de Santander (Project 1801).

I want to thank my friends of the SELVA group (Monica, Claudia, Margarita, Carolina, Zulma and Sebastian) who shared with me so many funny and unforgettable moments for the past years, for sharing good and bad news, for giving me new experiences and values, and to Andres for being my “studying friend”. Finally, I would like to thank all who contributed to the realization of this thesis.

TABLE OF CONTENTS

Pág.

LIST OF FIGURES

LIST OF TABLES

Pág.

LIST OF ANNEXES

Pág.

RESUMEN

TITULO: ESTUDIO DE LOS MATERIALES PERTENECIENTES AL SISTEMA $La_4BaCu_{5-x}M_xO_{13\pm\delta}$ (M: Co, Mn) CON POTENCIAL APLICACIÓN COMO ELECTRODO EN CELDAS DE COMBUSTIBLE DE ÓXIDO SÓLIDO (SOFC).[1]

AUTOR: DURAN AMAYA SILVIA ALEJANDRA[**]

PALABRAS CLAVES: SOFCs, Perovskita, Difracción de Rayos-X, Conductividad Eléctrica, Reactividad, Espectroscopía de Impedancia Electroquímica.

DESCRIPCIÓN:

Las perovskitas derivadas de $La_4BaCu_{5-x}M_xO_{13\pm\delta}$ (M: Co, Mn) fueron sintetizadas por el método sol-gel. Dos de los compuestos de la serie $La_4BaCu_{5-x}Co_xO_{13\pm\delta}$ (x=2 y 5) y uno de $La_4BaCu_{5-x}Mn_xO_{13\pm\delta}$ (x=5) fueron estudiados estudiadas como materiales de electrodo para celdas de combustible de óxido sólido (SOFC).

Los compuestos de Co no son estables en hidrogeno, al contrario de la manganita $La_4BaMn_5O_{13\pm\delta}$ (LBMn). Además, de manera similar a lo que sucede con otras cobaltitas, esos materiales presentan valores de coeficientes de expansión térmica (CET) que no son compatibles con los valores de CET del electrolito de estudio BCZY, al contrario de la manganita LBMn. El estudio termogravimétrico y DRXHT permitió confirmar la no estequiometría presente en esos materiales, además que la manganita presenta un comportamiento reversible al someterse a un ciclo redox a alta temperatura. Ambas series presentan altas conductividades eléctricas: LBCuCo2 con un valor máximo de conductividad en aire de 780 S cm^{-1} (460 °C) mientras que LBMn reporta 178 y 33.3 S cm^{-1}, en aire e hidrogeno a 800 °C, respectivamente.

Las propiedades electroquímicas de las cobaltitas, LBCu ($La_4BaCu_5O_{13\pm\delta}$) y LBMn fueron investigadas por EIS en atmosfera oxidante, observando la influencia de la temperatura de sinterización (serie cobalto). De manera general, para una temperatura de sinterización a 950 °C se identifican etapas de adsorción y de transferencia de carga e incorporación iónica al electrodo como procesos limitantes, mientras que, para una temperatura de sinterización de 1000 °C, se identifica la difusión gaseosa dentro de los poros del electrodo como el transporte de O^{2-} en la interfaz electrodo/electrolito. De las cobaltitas, LBCo presenta la más baja resistencia de polarización a 1000 °C. En el caso de LBMn, los valores fueron mayores, con un posible mejoramiento a futuro, al aumentar la temperatura de sinterización.

---

[1] Proyecto de Grado

[**] Facultad de Ingenierías Fisicoquímicas. Escuela de Ingeniería Metalúrgica y ciencia de materiales.

Director: Ph. D. Gilles H. Gauthier. Codirector: Ph. D. Leopoldo Suescun.

ABSTRACT

TITLE: STUDY OF THE MATERIALS BELONGING TO THE SYSTEM $La_4BaCu_{5-x}M_xO_{13\pm\delta}$ (M: Co, Mn) WITH POTENTIAL APPLICATION AS ELECTRODE ON SOLID OXIDE FUEL CELLS (SOFC).[*]

AUTHORS: DURAN AMAYA SILVIA ALEJANDRA[**]

KEY WORDS: SOFCs, Perovskite, X-Ray Difraccition, Electrical Conductivity, Reactivity, Electrochemical Impedance Spectroscopy.

DESCRIPTION:

The perovskites derived from $La_4BaCu_{5-x}M_xO_{13\pm\delta}$ (M: Co, Mn) were synthesized by the sol-gel method. Two of the compounds of the series $La_4BaCu_{5-x}Co_xO_{13\pm\delta}$ (x = 2 and 5) and one of $La_4BaCu_{5-x}Mn_xO_{13\pm\delta}$ (x= 5) were studied as electrode materials for solid oxide fuel cells (SOFCs).

The compounds of Co are not stable in hydrogen, unlike the manganite $La_4BaMn_5O_{13\pm\delta}$ (LBMn). In addition, in the same way as other cobaltites, these materials present values of Thermal Expansion Coefficients (TEC) that are not compatible with the TEC values of the BCZY study electrolyte, in contrast to the LBMn manganite. The thermogravimetric study and HT-XRD confirmed the non-stoichiometry present in these materials and, in addition, the manganite has a reversible behavior when subjected to a redox cycle at high temperature. Both series have high electrical conductivities: LBCuCo2 has a maximum conductivity value in air of 780 S cm^{-1} (460 °C) while the conductivity of LBMn is 178 and 33.3 S cm^{-1}, in air and hydrogen at 800 °C, respectively.

The electrochemical properties of the cobaltites, LBCu ($La_4BaCu_5O_{13\pm\delta}$) and LBMn were investigated by EIS in oxidizing atmosphere, observing the influence of sintering temperature (case of cobaltites). In general, for a sintering temperature at 950 °C, the adsorption and charge transfer stages and ionic incorporation to the electrode are identified as limiting processes, while, for a sintering temperature of 1000 °C, both the gaseous diffusion within the pores of the electrode as the transport of O^{2-} at the electrode/electrolyte interface. From the cobaltites, LBCo presents the lowest polarization resistance obtained at 1000 °C. In the case of the manganite LBMn, the values were higher, with a possible improvement in the future, increasing the sintering temperature.

---

[*] Thesis

[**]Physicochemical Engineering Deparment. School of Metallurgical Engineering and materials science.

Advisor: Ph. D. Gilles H. Gauthier. Co-Advisor: Ph. D. Leopoldo Suescun.

INTRODUCTION

In recent years, there have been major changes in energy systems that have led to more diversified energy baskets with a tendency to incorporate cleaner energy and technologies, for better energy use. Security and reliability in the supply of energy are fundamental for the development of the economic activities and the well-being of the inhabitants of any country. Although Colombia has a diversity of resources that have made it possible to meet the demand of energy from households, transportation and industry, it is necessary to move towards a diversification of the energy portfolio.

Among these technologies we find the high temperature fuel cells called SOFC (Solid Oxide Fuel Cell), devices that generate low levels of GHG due to their high efficiency and the types of fuels that can be used. Among them is natural gas, an easily accessible resource for the country. The Unidad de Planeación Minero Energética (UPME) reported that between 2015 and 2017 the maximum production of this resource would be close to 1,380 GBTUD, with a capacity to increase the percentage of probable reserves by 5% since it is presumed that there is a significant volume of gas to be discovered, indicating stability in the production of such resource [1].

Therefore, considering the relevance of the SOFC technology for Colombia, this thesis is a contribution to solve the issues presented by the state-of-the-art electrodes for SOFCs. These electrode materials must be able to operate at a lower temperature to limit their degradation and allow to reduce the cost of the system, *i.e.* more durability, higher thermodynamic efficiency and lower cost of interconnects. In certain cases, these materials can also have the advantage of being used in symmetric cells, a recent concept that offers the advantage of lowering the fabrication costs since the electrode material can be used on both sides of the cell (cathode and anode). For this reason, in recent years, research has focused on finding better electrocatalysts for electrode reactions. The first mixed oxide materials which have been developed for this purpose have been of a perovskite type structure since, according to the state of the art, these may exhibit relatively mobile oxygen vacancies, giving them a mixed conductivity, *i.e*. electronic and ionic mobility at the same time [2,3]. However, recently, new structural arrangements, generally derived from perovskite, but not only, and presenting a certain anisotropy (structure in sheets, among others), allowed to discover new mixed conductors, particularly, for the cathodic side. As an example, the mixed oxide materials of K_2NiF_4 structure type (Ruddlesden Popper phases) are compounds which have structural and transport properties that make them promising materials for the SOFC cathode [4–6]. Our research focuses precisely on similar arrangements with ordered vacancies as the $REBaCo_2O_{5+\delta}$ [7–11] and $LnBaCo_{2-x}M_xO_{5+\delta}$ [12–15] that give the structure a low dimensionality character, in order to find improved characteristics with respect to existing materials, based on the achievements that have been obtained in recent years in this area.

In this order of ideas, this research has directed us to the material $La_4BaCu_5O_{13+\delta}$, which was first reported by Michel *et al*. [16]. This compound presents an anisotropic structure with the presence of ordered oxygen vacancies in tunnels, a good electrical conductivity and also provides the possibility of being doped with other transition metals, typically with Co and Mn. Such doping elements would possibly enhance the electrocatalytic properties or stability in reducing conditions, respectively, since cuprates and reduced La/Sr manganites (LSM) can exhibit similar structural features, *i.e.* an ordering of the formed oxygen vacancies [17,18].

Concretely, this work deals with a study of the $La_4BaCu_5(Co,Mn)O_{13\pm\delta}$ series, materials that are derived from the oxygen deficient perovskite $La_4BaCu_5O_{13+\delta}$. Their possible use as cathode and/or anode will depend on the evaluation of stability and reactivity in both oxidizing and reducing atmosphere, as well as the relationship between the structural characteristics and the improvement of the electrochemical behavior of the cell. The first chapter describes the state of art (scientific context), the operation of SOFCs and the general requirements of the main components (anode, cathode and electrolyte). Additionally, a review of the electrodes mainly used as advances of them in the past years. Chapter 2 presents the methodology applied to obtain pure phases within $La_4BaCu_5(Co,Mn)O_{13\pm\delta}$ series, and the techniques used to analyze the compounds *i.e.* structural characterization (XRD), thermogravimetric analysis (TGA), thermodifraction (HT-XRD), electrical conductivity (4-probe technique) and electrochemical impedance spectroscopy (EIS). Finally, chapter 3 and 4 concerns the results of $La_4BaCu_{5-x}Co_xO_{13\pm\delta}$ and $La_4BaCu_{5-x}Mn_xO_{13\pm\delta}$, respectively. From the structural characterization performed by X-ray Diffraction data and the thermal stability at high temperatures in oxidizing and reducing conditions, it will be possible to make a first selection of potential electrode materials that can be used as a cathode only or as anode and cathode, an important aspect to evaluate their viability for symmetrical SOFC. The latter will include the determination of their aptitude for oxygen non stoichiometry, their electrical properties in air and hydrogen and preliminary results of Electrochemical Impedance Spectroscopy in anode and/or cathode conditions.

1. STATE OF THE ART

1.1. FUEL CELLS

A fuel cell is an energy conversion device that, electrochemically, transforms the chemical energy of a combustion reaction into electrical energy [19]. The process develops continuously as long as the cell is supplied with enough fuel and oxidant (external source). Figure 1 shows the simplified structure of a SOFC fuel cell as well as the principle of operation, where its structure is composed of a layer of dense electrolyte that lies between two porous electrodes (cathode and anode), within which the following reactions take place:

Cathode: $$O_2 + 4e^- \leftrightarrow 2O^{2-} \qquad \textit{(1-1)}$$

Anode: $$2H_2 + 2O^{2-} \leftrightarrow 2H_2O + 4e^- \qquad \textit{(1-2)}$$

$$C_nH_{2n+2} + (3n+1)O^{2-} \leftrightarrow nCO_2 + (n+1)H_2O + (6n+2)e^- \qquad \textit{(1-3)}$$

In reaction *(1-1)*, oxygen reacts with the electrons entering the external source generating oxide ions that migrate through the electrolyte. In reaction *(1-2)* or *(1-3)*, for *(1-2)* hydrogen fuel and for *(1-3)* any type of hydrocarbon fuel, the latter is oxidized by the oxide ions releasing electrons flowing through the external electric circuit; this charge flow is balanced by an ionic flow through the electrolyte [20,21].

Figure 1. Operation scheme of a Solid Oxide Fuel Cell (SOFC).

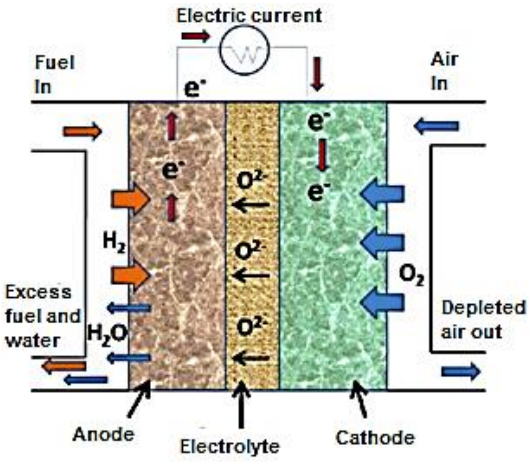

Fuente: [22]

These devices are highly effective for the direct conversion of fuels into electricity, with fuel/electricity yields ranging from 50% to 75%, much higher than classical combustion cycles (thermal plant) [23,24]. In addition to being able to adapt to different scales, the High Temperature Fuel Cells (*Solid Oxide Fuel Cell*, SOFC) have the theoretical (thermodynamical) advantage of operating with any kind of carbon-containing fuel, such as hydrocarbons, alcohols, synthesis gas, among others, which may be possible thanks to its operating temperature (600-1000°C) [23,24]. It should be noted that the operating temperature depends mainly on the nature of the electrolyte and the mechanism in which the cells operate; Table 1 summarizes some current types of fuel cells [25].

Table 1. Types of fuel cell and their ranges of operating temperature.

Cell type	Electrolyte	Operating temperature
PAFC	Phosphoric Acid	200°C
PEM	Proton Exchange membrane	80°C-100°C
MCFC	Molten carbonate	650°C
SOFC	Solid Oxide (ceramic)	600°C-1000°C

Fuente: [25]

In this work, SOFC is the system of interest. However, the thermal conditions under which it operates become one of the major drawbacks of these devices due to the decrease in the life time as a result of the degradation of the constituting materials, the limitation in the use of costly interconnectors, stability problems owing to phenomena of diffusion, chemical reactivity, etc. [26]. In this context, most research is directed towards the search for new electrolyte, anode and cathode materials that can overcome these operational disadvantages and allow operation in the range of lower temperatures (600-800°C and ideally 600-700°C). These devices are called IT-SOFCs for operating in an intermediate temperature range (*IT for "Intermediate Temperature"*) [27]. With this race to new electrode materials, the concept of symmetrical cells has emerged [28–31]; this last configuration leads to an assembly where the electrode can be used as cathode and anode simultaneously, therefore requires a single thermal treatment, reducing problems of chemical incompatibility and thermal coefficient with the electrolyte. However, the electrodes for symmetrical cells must meet the requirements for both cathode and anode materials shown in Table 2.

In addition, it is important to mention that the materials commonly used for the anode and cathode still present problems; therefore, the development of new materials to carry out the possible applicability of the IT-SOFCs as well as that of the symmetric cells is in the understanding and solving the mechanisms of degradation and improving the properties of those materials at low temperatures. Thus, the commercial success of these devices lies in the synthesis and characterization of new materials in order to (i) improve the kinetics of cathodic reaction (oxygen reduction) and anodic reaction (oxidation of fuel), and (ii) replace the use of nickel cermet, which is intrinsically unstable in redox cycles, leads to carbon formation and is sensitive to impurities, such as H_2S, when hydrocarbon fuels are used.

Based on the above, the general requirements of the components that make up a SOFC type cell, are summarized in Table 2*.*

Table 2. General requirements of the components and state-of-art materials of a SOFC.

Component	**Material**	**General requirements**
Anode	Cermet Ni/YSZ (Ni/ZrO_2 stabilized with Y_2O_3) Cermet Ni/GDC (Ni/CeO_2 stabilized with Gd_2O_3)	*(i)* To be porous in order to have a better catalytic activity and diffusion of the gas for oxygen reduction (cathode) or fuel oxidation (anode). *(ii)* Good chemical stability and with the electrolyte material and similar coefficient of thermal expansion. *(iii)* High electronic conductivity (minimum 1 S cm^{-1} and if possible higher than 100 S cm^{-1}) and ionic conductivity (>0.01 S cm^{-1}) under the operating conditions in order to increase the surface area of the effective reaction zone. *(iv)* Dimensional and thermodynamic stability over wide ranges of partial pressure of oxygen and temperature [32].
Cathode	$La_{1-x}Sr_xMnO_3$ (LSM) $Ba_{0,5}Sr_{0,5}CoO_3$ $La_{1-x}Sr_xCo_{1-y}Fe_yO_3$	
Electrolyte	YSZ (ZrO_2 stabilized with Y_2O_3) GDC (CeO_2 stabilized with Gd_2O_3)	*(i)* Elevated ionic conductivity (>0.01 S cm^{-1}). *(ii)* Low electronic conductivity (t_e *electronic transport number* <10^{-3}). *(iii)* No chemical reactivity with electrode materials. *(iv)* Coefficient of Thermal Expansion compatible with electrode materials and interconnectors. *(v)* Stable structure throughout the thermal cycle of the device. *(vi)* High density (>90%) in order to avoid interconnected porosity. *(vii)* Ability to withstand a wide range of oxygen partial pressures [33].

1.2. MATERIALS FOR ELECTRODES

The materials summarized in Table 2 are considered state-of-the-art materials because of their generally good compatibility with electrolyte, durability and electrical/electrochemical properties. However, it is worth mentioning that the materials commonly used for the SOFC anode and cathode still present problems: Ni/YSZ cermet, a composite between nickel metal grains and YSZ ceramics (zirconia stabilized with yttrium oxide) used as anode, is intolerant to hydrocarbon fuels due to the presence of sulfur impurities contained in most of the real fuels, besides giving rise to the formation of carbon deposits; it is also unstable against redox cycles that may occur during the system operation. On the other hand, the state-of-the-art cathode, strontium doped lanthanum manganite (LSM) of formula $La_{1-x}Sr_xMnO_3$, needs a high operating temperature, generally higher than 800°C, so that the material does not present electrochemical limitations, that means a higher degradation rate of the system and the use of expensive interconnect materials [2]. However, the structural flexibility in this type of perovskite compounds has allowed a great advance in the search for new materials for SOFC cells (particularly electrodes).

1.2.1. Materials of perovskite and derived structure.

The perovskite presents the chemical formula ABX_3, constituted by three different chemical elements, where cations A are generally alkaline earths or lanthanide, cations B are essentially transition metals and X anions may be mainly chalcogenides (typically oxygen) or halides (iodine or bromine). The perfect perovskite structure presents a cubic cell that can be described as follows: a cation A located in the center of the cube and the cations B occupying the eight vertices (octahedron frame BX_6, that is, bound to the six anions that surround it) of shared corners, where X anions will be found in the middle of the twelve edges of the cube (Figure 2) [26,34,35].

Figure 2. Graphical representation of the perovskite structure.

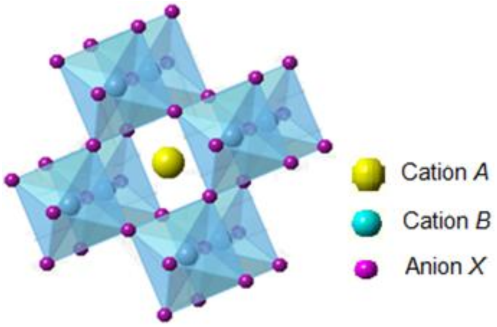

Thanks to the fact that the structure presents a great flexibility, most of the elements of the periodic table can be found in perovskite compounds, resulting in a large family with a wide diversity of properties. Sometimes, the doping in the structure results in the formation of network defects, which are of great importance for some properties such as ionic, electron and mixed conductivity, or even superconductivity, among others [36].

1.2.2. Anode. The anode materials [2] commonly used in these SOFCs are cermets (ceramics-metal compounds) between them the Ni/YSZ material. Although Ni/YSZ cermet is the most widely used anode material due to its high mixed conductivity (at the microstructure level) and excellent electrocatalytic activity, it has a number of drawbacks such as the high tendency to form carbon deposits when hydrocarbons are used, sulfur poisoning due to sulfides that may be contained in real fuels, intolerance to the redox cycles that may occur in those systems, and aging of the microstructure by agglomerations of the nickel particles [20]. On this anodic side, the complexity of using other fuels than hydrogen, like methane, the main constituent of natural gas, makes that few cases have been considered up to now. It has been found that the Ni/YSZ cermet based composite anode material, which is the state of the art material, is rapidly poisoned with pure natural gas because the catalytic cracking reaction is kinetically faster than the oxidation or steam reforming with the water produced by the cell [3,37–40]. This poisoning occurs due to the presence of nickel, which catalyzes not only the reactions necessary for the cell operation but also parallel reactions. In order to solve the disadvantages caused by the presence of a high content of Ni in the anode, the possible replacement of Ni/YSZ with mixed oxide-type monophasic materials has been proposed, which can theoretically exhibit both electronic and ionic conductivity (*MIEC for Mixed Ionic and Electronic Conductors*), increasing the area of the oxidation reaction, mitigating the problems of redox stability, sulfur sensitivity and carbon formation due to the increased availability of oxygen near the reaction site. This is why the perovskite oxides ABO_3 have been proposed as alternatives for anode materials as they normally exhibit good resistance to coke formation in comparison to the Ni/YSZ cermet [36]. Of these perovskite oxides, $La_{1-x}Sr_xCrO_3$ (LSCr)-based materials are considered the state of art perovskite for the anodic side, being in particular $La_{0.75}Sr_{0.25}Cr_{1-x}Mn_xO_3$ (LSCM) the composition which exhibits good performance as anode in fuel cells where the fuel is pure hydrogen showing a polarization resistance close to 0.2 Ω cm^2 at 900 ºC [41–45] and a comparable polarization resistance when operating with methane at 950 ºC [46]. In addition, several doped titanates have been reported with relatively good behavior, *i.e.* $La_xSr_{1-x}TiO_3$ [47–50]. Gauthier *et al*., reported that $La_{0.23}Ce_{0.1}Sr_{0.6}TiO_{3+\delta}$ compound is a potential anode material for SOFC when operating with methane gas at 900 ºC [51]. On the other hand, Irvine *et al*. [4] reported that titanates of general formula $La_4Sr_8Ti_{12-x}Mn_xO_{38-d}$ exhibit low polarization resistances of 0.3 y 0.7 Ω cm^2 at 950 ºC in hydrogen gas and methane, respectively. It confirms that the substitution with Mn improves the electrochemical performance of these anodes, especially at high temperatures.

1.2.3. Cathode. In the case of the cathode, the high operating temperatures (800–1000 °C) make it possible to use cheaper materials compared to noble metals such as Pt or Pd, which, although having adequate properties, cannot be considered for commercial application. In this sense, the first realistic and also most commonly used cathode material for this application is strontium doped lanthanum manganite (LSM), of formula $La_{1-x}Sr_xMnO_3$ ($x= 0.2 - 0.5$), and of perovskite structure. These compounds present good conducting properties (mainly electronic since ionic conductivity is very low) and acceptable electrocatalytic behavior, but at temperatures between 800 and 1000 ºC. Currently, the decrease in operating temperature (T< 800ºC) becomes one of the requirements to *(i)* avoid the use of interconnect materials (part of the individual cell system) of high cost, and *(ii)* limit the degradation on all components of the cell. From this perspective, there are some problems with LSM, among which we can mention that *(i)* It presents a high cathodic polarization resistance below 800 ºC *(ii)* and can react with the electrolyte material during the cell elaboration at high temperatures, forming insulating phases at the interface of the two components [2].

Therefore, according to the aforementioned problematic, many studies have focused on new compositions oriented towards the search of materials for use as SOFC cathode keeping the perovskite or derived structure type, like the Ruddlesden-Popper (RP) K_2NiF_4 compounds [5,6] or the double perovskites [52,53], among others. In this sense, materials such as Rare Earth cobaltites of perovskite structure result attractive compounds for use as cathodes, mainly due to their possible oxygen deficiency, especially at high temperature. For example, Sr-doped lanthanide cobaltites $Ln_{1-x}Sr_xCoO_{3-\delta}$ (Ln= Pr, Nd, Sm and La) have been investigated as IT-SOFCs cathodes due to their good electrical properties and high catalytic activity [54–57]. However, some of these materials have shown mechanical incompatibilities with the electrolytes due to elevated thermal expansion coefficients caused by a strong variation of oxygen content with temperature. Solutions have been proposed to reduce the high chemical and thermal expansion by adequate substitution of cobalt for example with iron. $La_{1-x}Sr_xCo_{1-y}Fe_yO_3$ (LSCF) perovskite presents high electron and ionic conductivity (mixed conductor) by increasing the Sr or Co content, respectively, that results in a remarkable electrocatalytic activity although their compatibility with YSZ zirconia is still questionable [58]. Nonetheless, the use of other electrolytes, such as doped ceria, can allow operation at lower temperatures with those materials. Another rare earth-free cobaltoferrite, namely

$Ba_{0.5}Sr_{0.5}Co_{0.8}Fe_{0.2}O_3$ (BSCF), has been proposed as a good alternative for operating temperatures below 600 ºC since such compound exhibits interesting electrocatalytic properties [59]; unfortunately, it presents poor thermomechanical stability and its desired cubic structure collapses at temperatures below 850 °C due to a change in oxidation state of the Co ion [60].

Continuing with other materials containing cobalt, compositions based on laminar perovskites having oxygen vacancy ordering have been recently proposed as interesting alternatives to classical disordered perovskites like LSCF or BSCF, thereby seeking an improvement of the cathode properties in the fuel cells. Ordered oxygen deficient perovskites generally present a good mixed (electronic and ionic) conductivity due to the presence of 3*d* transition metals with the capacity to vary their valence and sphere of coordination [61]. Among them, we can find $REBaCo_2O_{5+\delta}$ materials with structure-ordered vacancies according to (2D) planes, in which the barium arrangement in the structure stabilizes oxygen vacancies exhibiting high electrical conductivity in the range of temperature 100-850ºC. Those materials present high electrocatalytical activity for Oxygen Reduction Reaction (ORR) and are able to operate at low temperatures reaching good performance with power densities higher than 1 W cm^{-2} at 600 ºC, which makes them promising for the cathodic side of the cell [7–11]. Unfortunately, the application of those pure cobaltite cathode materials is impeded by high thermal expansion coefficient (TEC). However, various studies containing the Lanthanide group with substitution on the B-site have demonstrated that $LnBaCo_{2-x}M_xO_{5+\delta}$ (Ln = Pr, Nd, Sm, Gd, M = Fe, Cu, Ni) oxides possess lower TEC values than $LnBaCo_2O_{5+\delta}$. For example, the material $SmBa_{0.5}Sr_{0.5}CoCuO_{5+d}$ (SBSCCo) has been described for its good chemical compatibility with the electrolyte GDC and LSGM at temperatures below 950 ºC, a TEC value of 16.14×10^{-6} K^{-1} in the temperature range 30–850 ºC, good electrical conductivity between 110 and 206 S cm^{-1} for T=200-850ºC in air, and low ASR values (0.0378 and 0.0488 Ω cm^2) what makes it ideal for IT-SOFCs [62] compared to the $SmBaCo_2O_{5+\delta}$ cathode [63]. Furthermore, studies reported the comparison between ordered/disordered perovskite cobaltites where disordered structures present higher conductivities and better stability than ordered phases in air, argon and oxygen; suggesting the disordered structure as a promising cathode for SOFCs [64,65]; on the other hand, ordered phases present low ASR values compared to disordered structures making them also promising for the cathodic side [66]. Those materials are a clear example of how the structure ordering can be very interesting for performant cathode materials.

Finally, cuprate materials have not been very far studied for SOFC applications (in comparison to superconductors, for example). Recently, Yu *et al*. reported an interesting investigation on strontium-doped lanthanum cuprates of composition $La_{1-x}Sr_xCuO_{2.5}$ as possible materials for cathode. In these materials, the substitution of 30% strontium for lanthanum resulted in a considerable increase of the electrical conductivity (830 S cm^{-1} at 800 ºC in air). No chemical reaction was reported between $La_{1-x}Sr_xCuO_{2.5}$ (0.2< x<0.3) and 8YSZ at 800 ºC, with a lower polarization resistance than the strontium doped lanthanum manganites (LSM) normally used as cathodes [67]. The use of these materials as cathode of intermediate temperature cells was proposed by demonstrating that the mixture $La_{1-x}Sr_xCuO_{2.5}$ (0.2<x<0.3) with 8YSZ was stable until 800 ºC (for 1000 h) without generation of secondary phases, but led to the formation of the insulating phase $SrZrO_3$ at 900 ºC. An additional advantage was the low polarization resistance of $La_{0.7}Sr_{0.3}CuO_{2.5}$/YSZ (0.25 Ω cm^2 at 800 ºC), which can be explained by the presence of oxygen vacancies that improve the transport of O^{2-} ions from the electrode surface to the electrode/electrolyte interface [68]. Likewise, the effect of doping at A and B sites in the structure $La_{1-x}A_xCu_{1-y}B_yO_{2.5}$, (A: Ba, Sr; B: Ni) was reported, where barium-doped cuprates showed good electrical conductivity and a significant loss of oxygen at temperatures below 700 ºC. Additionally, it was found that doping with Ni at B site markedly decreased conductivity [69]. It is very important to note that in these works, cuprates did not have a structure with ordered vacancies, but a classical pseudo-cubic perovskite structure. On the other hand, another material in which it was possible to improve the properties thanks to the substitution with Cu is the cobaltite $Ca_3Co_2O_6$ following the general formula $Ca_3(Co_{1-x}Cu_x)_2O_6$ and finding that the substitution with Cu leads to a disordered structure deficient in oxygen, presenting for x=0.05 a power density of the cell as high as 550 mW cm^{-2} at 800 ºC, due to the strong improvement of the electronic and ionic transport properties [70].

1.3. PURE AND DOPED $La_4BaCu_5O_{13+\delta}$ MATERIALS

Taking into account the properties of the previous materials and the recent interest within the scientific community for structures with ordered vacancies, our analysis leads us towards the oxygen deficient perovskite $La_4BaCu_5O_{13+\delta}$, which was first reported by Michel *et al.* [16] as a tetragonal structure with space group *P*4/*m* ($a = \sqrt{5a_p} = 8.644\ \text{Å}, b = a_p = 3.867\ \text{Å}$ where a_p refers to as the parameter of the cubic perovskite sub-cell). The structural model consists of groups of four pyramids CuO_5 sharing corners and linked through octahedra CuO_6, so that each octahedron shares four corners with four pyramids and two corners with four octahedra; each pyramid is connected to four other pyramids and one octahedron (Figure 3). The crystal network exhibits a perovskite tunnel and two hexagonal tunnels per cell, where Ba^{2+} cation acquires a coordination of 12 in the perovskite tunnels and La^{3+} a coordination of 10 in the hexagonal tunnels [71,72]. In $La_4BaCu_5O_{13+\delta}$, the oxygen content is sensitive to the processing conditions in a range of values from 12.5 to 13.2; for example, when heating the material to 500 ºC in reducing atmosphere (15%H_2 / 85%Ar), three phases are stabilized with δ= -0.5, -1.0 and -2.0, where $La_4BaCu_5O_{11}$ is tetragonal while $La_4BaCu_5O_{12}$ and $La_4BaCu_5O_{12.5}$ are monoclinic [73]. In addition, Gauthier *et al.* recently reported that $La_4BaCu_5O_{13+\delta}$ presents stability up to 900 C with a reasonable TEC value of 17.3×10^{-6} K^{-1} and high electrical conductivity about 500 S cm^{-1}. Nonetheless, very limited oxygen excess δ was evidenced in the tunnel until at least 700 °C in air. Additionally, the non-doped compound exhibits a strong reactivity with classical YSZ and GDC electrolytes but an excellent chemical compatibility with doped barium cerate and zirconate (BCG[2] and BZY[3]) opening new perspectives to this material as a possible cathode in SOFC cells [74] and a probably good chemical compatibility with BCZY[4] electrolyte which has been reported as a possible electrolyte material for PCFC *(Proton Conducting Fuel Cell)* [75], owing to its higher proton conductivity values (one or two orders of magnitude) than common SOFC electrolytes [12], since the doped barium zircono-cerate BCZY combine the high proton conductivity of barium cerate (BCY) and the good chemical stability of barium zirconate (BZY) [76–78].

Figure 3. Graphical representation according to the direction [001] of the crystal structure of $La_4BaCu_{5-x}O_{13+\delta}$.

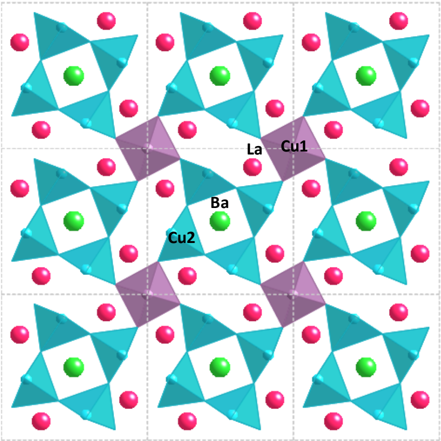

Knowing that the properties of these cuprates are attributed to the ordering of the oxygen vacances and that the conduction properties can be modified by the value of δ, some subsequent investigations suggested the substitution of copper for other cations such as Co and Ni, elements that are also recurrent in the best compositions of IT-SOFC cathode materials. Shivakumara *et al.,* demonstrated that using a synthesis method with flux of NaOH/KOH, the substitution of Cu with Ni or Co could

---

[2] $BaCe_{0.9}Gd_{0.1}O_{2.95}$

[3] $BaZr_{0.85}Y_{0.15}O_{2.925}$

[4] $BaCe_{0.2}Zr_{0.7}Y_{0.1}O_{3-\delta}$

tend to the formation of the phases $La_4BaCu_4CoO_{13+\delta}$ y $La_4BaCu_4NiO_{13+\delta}$, which maintain the tetragonal structure (*P*4/*m*) with Ni^{3+} o Co^{3+} occupying partially the octahedral and penta-coordinated sites of the system $La_4BaCu_5O_{13+\delta}$ [79]. Additionally, Anderson *et al*. [73] reported the synthesis of $La_4BaCu_{5-x}M_xO_{13+\delta}$ (M=Fe, Co, Ni, Zn) compounds prepared by solid state at 1000 ºC, finding that the limit of the solid solution was x=1 for Fe, x=1.1 for Co, x=1.56 for Ni and x=0.47 for Zn. At the same time, neutron diffraction experiments allowed to confirm that, for Fe and Ni, the substitution was preferential over the octahedral site, and for Co the substitution could take place in both the octahedral site and the square pyramidal site [80].

It is worth noting that neither $La_4BaCu_5O_{13+\delta}$ nor their homologues doped with Co or Ni should have the sufficient stability in reducing atmosphere (anode) what makes it necessary to try to stabilize this material in an environment of H_2. Fortunately, in the literature, the structure of some $La_{1-x}Sr_xMnO_{3-\delta}$ manganites has been described that corresponds to an ordering of their oxygen vacancies, generated by a reduction in hydrogen atmosphere. The obtained materials, which can be written $(La_xSr_{1-x})_5Mn_5O_{13}$ (x= 0.1-0.3), exhibit the same structure as $La_4BaCu_5O_{13+\delta}$, *i.e.* they correspond to the ordering of four $Mn^{3+}O_5$ pyramids and an octahedral Mn cation that changes its charge from Mn^{4+} for x=0 to Mn^{3+} in x=0.3, allowing the formation of tunnels [17]. In addition to the stability in reducing atmosphere, our interest is precisely the existence of a possible $La_4BaCu_{5-x}Mn_xO_{13+\delta}$ solid solution with possibly new electrical and electrochemical properties as cathode and anode. It is important to mention the existence of other similar structures, that means with ordering of oxygen vacancies, in the case of pure lanthanum at the A site: $La_8Mn_8O_{23}$ ($LaMnO_{2.875}$) and $La_4Mn_4O_{11}$ ($LaMnO_{2.75}$) [81].

Considering the above, our first objective is the possibility of replacing Cu by Co in $La_4BaCu_5O_{13+\delta}$ matrix, with the aim to possibly increase oxygen nonstoichiometry at high temperature in air and to obtain improvements of the cathodic properties. In addition, the substitution of Cu by Mn in the same framework is proposed to stabilize the cuprate in reducing (anodic) atmosphere; the underlying idea is indeed the use of the same material (or the same structure at least) on both sides of the cell.

This bibliographic analysis provides methodological and structural advances that will serve as a basis for preparing possibly new materials with similar structures within the $La_4BaCu_{5-x}M_xO_{13+\delta}$ (M: Co, Mn) series, hoping that they have conduction and electrocatalytic properties suitable for use as an electrode (cathode and/or anode) in SOFC.

2. METHODOLOGY

In this chapter, the synthesis of $La_4BaCu_{5-x}M_xO_{13\pm\delta}$ (M=Co, Mn) compounds is described, as well as a brief description of the characterization techniques for the study of the properties of the materials, using the following sequence.

2.1. SYNTHESIS OF $La_4BaCu_{5-x}M_xO_{13\pm\delta}$ (M=Co, Mn) COMPOUNDS

Different routes of synthesis can be applied to synthesize oxide materials derived from the perovskite structure. The solid-state reaction leads to large size particles due to calcination at high temperatures and requires several steps of grinding. On the other hand, wet chemical routes such as sol-gel or auto-combustion allow a perfect mixt of the elements at an atomic level resulting in lower sintering temperatures [82,83].

In this work, we used the polymeric gel method aiming to obtain higher solubility limits, lower sintering temperature and small particle size very useful for further experimental procedures like cell preparation. The polycrystalline samples (solid solutions) of the family $La_4BaCu_{5-x}M_xO_{13\pm\delta}$ (M=Co, Mn) were prepared at different values of x ($0 \leq x \leq 5$), using the synthesis method described below and illustrated in Figure 4.

In both families, the precursors were pre-calcined at determined temperatures before using in order to remove hydration and carbonation products to facilitate the weighing of the precursors in stoichiometric proportions; La_2O_3 at 1000 °C, $BaCO_3$ and CuO at 500 °C, and Co_3O_4 at 200 °C for 1 hour each. In the case of Mn compound, a test of weight loss to fire was performed to $MnCO_3$ precursor at 700 °C/5 h in order to obtain the conversion factor to Mn_2O_3 precursor. In this regard, stoichiometric amounts of CuO (≥99,9% Alfa Aesar), Co_3O_4 (≥99,9% Alfa Aesar), $BaCO_3$ (≥99,9% Aldrich), La_2O_3 (≥99,9% Alfa Aesar), $MnCO_3$ (≥99,9% Aldrich), chelating agent Ethylene Diamine Tetraacetic acid (EDTA, ≥99.4% Sigma Aldrich) in a molar ratio of EDTA:(cation)$_{total}$ = 1:1 [84] adding NH_4OH (28.0-30.0% Sigma Aldrich) in order to dissolve the EDTA and maintain the pH value to 9-10. Citric acid (CA, ≥99,5% Merck) was added in a molar ratio of EDTA:CA = 1:1.5 to obtain a homogeneous and stable solution [85]. The resulting deep blue-purple (Cu/Co) or blue-yellow (Cu/Mn) solution was heated at 70-90 °C under constant stirring. The temperature was gradually increased until reaching 110 °C in order to evaporate the water, and polymerization agent ethylene glycol (≥99% Panreac) was added in a proportion of 1.5 mL per gram of final product, initiating gel formation. The resulting viscous gel was subsequently heated at T~200 °C so that a dry dark gel was obtained, that was subsequently calcined at 300 °C and 500 °C for 3 - 4 hours in air to make sure total organic matter decomposition and to obtain ashes.

Figure 4. Illustrated polymeric gel method of synthesis.

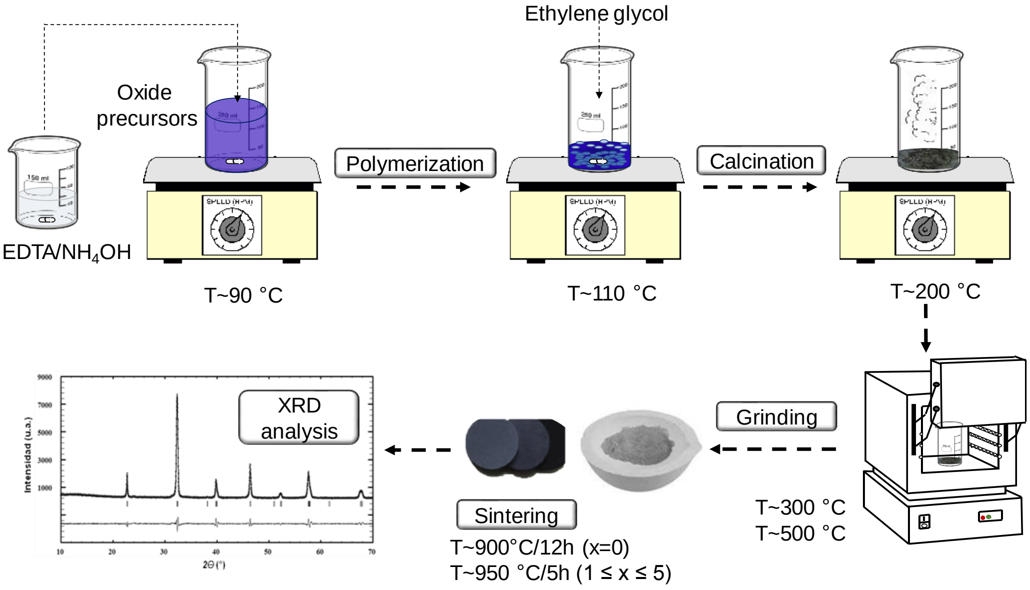

Finally, the powder was grinded in an agate mortar and then pressed into pellets of 1 cm in diameter, to be then sintered in air at 900°C for 12 hours for x= 0 and 950 °C for 5 hours for 1 ≤ x ≤ 5.

2.2. CHARACTERIZATION TECHNIQUES

Structural characterizations were carried out for all samples of both families in the range 0≤x≤5; considering those results, the rest of our study (electrical/electrochemical measurements) was dedicated to the $La_4BaCu_3Co_2O_{13+\delta}$ (LBCuCo2), $La_4BaCo_5O_{13+\delta}$ (LBCo) and $La_4BaMn_5O_{13+\delta}$ (LBMn) compositions, as representative members of the fully ordered (with highest Co and Mn content) and disordered phase, respectively.

2.2.1. Structural characterization

X-ray Powder Diffraction (XRD) technique was used to analyze the samples, looking for the formation of single phases. The data were recorded using a D8-AVANCE Bruker diffractometer in a Bragg-Brentano type focusing geometry and a $CuK_{\alpha1,2}$ radiation (λ = 1.540598 and 1.54439 Å). The patterns were collected at Room Temperature (RT) in an angular range of 5-70° (2θ) for qualitative and Rietveld analysis, using a 2θ step size of 0.01526°. XRD pattern obtained from each of the phases was compared with the diffraction profiles reported in the ICDD database (International Center for Diffraction Data). After checking the purity of the phase, structural refinement was carried out by the Rietveld method, using the Fullprof program and its WinPLOTR graphical interface [86,87] (Annex A), with which the cell parameters and the agreement factors were determined. These results were compared with those obtained by other authors or eventually reported in the ICDD database.

2.2.2. Material stability

2.2.2.1. Stability at high temperatures (HT). A stability test of the materials in air at high temperature is necessary, taking into account that the adhesion of the electrodes on the electrolyte in the EIS test or the pellet densification for conductivity measurements will require higher temperatures than the temperature of synthesis. For this purpose, pellets from each material were subjected to the following thermal process: 1000, 1050 and 1100 °C for 6h in air. After each thermal treatment, the samples were studied by XRD as described in section 2.2.1.

2.2.2.2. Stability in reducing atmosphere. To estimate the ability of the materials prepared in air to be used as SOFC anode, the as-synthesized powders (0.2-0.5 grams) were reduced in a tubular furnace at 850 °C. Experimentally, a constant flow of N_2 was first circulated inside the oven for 15 minutes at Room Temperature (RT) in order to remove all the air present inside the oven and generate inert conditions. Then, a flow of 3% H_2/N_2 (Q=2.5 L/h) was introduced while the oven temperature started to raise until reaching 850 °C with a heating ramp of 300 °C/h. Once the desired temperature was reached, the flow was increased to 6 L/h and maintained for 6 hours, then decreased again to 2.5 L/h until the temperature of the oven dropped to 250 °C. The resulting materials were characterized by XRD to study their stability in reducing atmosphere (anode conditions) as described in section 2.2.1.

2.2.2.3. Chemical reactivity with $BaCe_{0.2}Zr_{0.7}Y_{0.1}O_{3-\delta}$ (BCZY) electrolyte. Based on the state of art, the composition $BaCe_{0.2}Zr_{0.7}Y_{0.1}O_{3-\delta}$ (thereafter referred to as BCZY) was chosen as the electrolyte to carry out the EIS and the chemical compatibility test due to its stability in the oxidizing and reducing atmospheres [77], the dense electrolyte pellets of BCZY were supplied by the Colorado School of Mines (Colorado, USA), prepared by solid state reactive sintering (SSRS) at 1500 °C [88]. In that order of ideas, to corroborate the stability of the materials to be studied in the presence of the electrolyte at high temperatures, a reactivity test was carried out. Each of the as-synthesized materials were mixed with BCZY powder in a 50:50 weight ratio, which was homogenized in an agate mortar and pressed into pellets to undergo a heat treatment chosen from the stability tests (1000 °C/6h). In the same way, the resulting powders were analyzed by XRD as described in section 2.2.1

2.2.3. Thermal behavior (HT-XRD) and thermogravimetric analysis. The structural behavior of the materials was studied using HT-XRD (High Temperature – X Ray Diffraction) technique in which, for Cu/Co family, data were collected in air every 50 °C from Room Temperature (RT) to 850 °C using a Panalytical Empyrean diffractometer equipped with an Anton Paar HTK 1200N oven chamber using a beam of CuK$\alpha_{1,2}$ radiation. On the other hand, for the LBMn compound, a redox cycling was performed following a sequence of three continuous cycles of heating/cooling from RT to 800 °C in air, diluted hydrogen (3% H_2/N_2) and, lastly, in air to study the compound re-oxidation. The data were collected every 25 °C with heating/cooling rates of 5 °C min^{-1} using a D8 Bruker diffractometer equipped with an Anton Paar XRK900 oven chamber, a CuK$_{\alpha1,2}$ radiation incident radiation with a Lynxeye detector. XRD patterns were refined using the "cyclic refinement" option implemented in the Fullprof program and its graphical interface WinPLOTR [86,87] using a profile matching approach. The Thermal Expansion Coefficients (TECs) have been obtained considering the case of axial tetragonal and rhombohedral symmetries [101]:

$$TEC = 1/3\ (2\alpha_a + \alpha_c) \qquad (2\text{-}1)$$

, where α_a (normal to the c-axis) and α_c (along the c-axis) are the two coefficients of linear expansion along *a* and *c*.

Additionally, to determine the absolute oxygen stoichiometry of the samples after synthesis and study its evolution in air as a function of temperature, thermogravimetric (TG) measurements were carried out; about 20 mg of target product was placed on a holder in a Discovery TGA 5500 thermobalance using an artificial air flow (5 mL min^{-1}). The measurements were performed using two cycles (heating/cooling) from Room Temperature (RT) to 800 °C in air, with a ramp rate of 1.5 °C min^{-1} (the first cycle only for cleaning from adsorbed undesirable species). Also, TG analyses were carried out in anodic conditions using a Hiden-Isochema gravimetric analyzer (model IGA-003) to evaluate the stability of the materials in reducing atmosphere; the compounds were initially reduced at 1000 °C for 18 h in

5% H_2/Ar with a heating ramp rate of 1°C min^{-1} then characterized by XRD to observe the total decomposition and quantify the exact initial stoichiometry after synthesis.

2.2.4. Conductivity measurements. Electrical conductivity was determined with the collaboration of UCCS institute (Lille, France) using the 4-probe DC technique in air at variable temperature and a BioLogic SP-300 Potentiostat-Galvanostat from 60 to 800 °C with 50 °C step, only in oxidizing atmosphere for the Cu/Co materials. In the case of LBMn, three consecutive cycles were performed following a sequence of heating/cooling from 60 to 800 °C in air, diluted hydrogen (3% H_2/N_2) and, finally, in air (re-oxidation). Each powder was previously pressed in the form of dense cylindrical pellets (4 mm in diameter and 9 mm in thickness) and sintered at 1200 °C for 6h leading to relative density higher than 70%. Figure 5 shows the schematic representation of the measurements performed using gold wires and gold paste for contacts in air. A direct current was injected through the two outside terminals, being between 10 and 100 mA in air, and the voltage was measured between the two inside terminals.

Figure 5. Schematic representation of the samples for the four-points probe DC measurement of electrical conductivity.

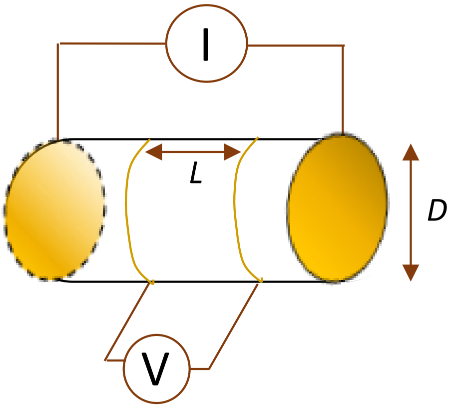

Following Ohm's Law, total conductivity was estimated as:

$$I = \frac{V}{R} \tag{2-2}$$

Where I is the current (amperes) through the conductor, V is the voltage (volts) measured across the conductor and R is the resistance (ohms) of the conductor. The electrical conductivity (σ) with [S cm^{-1}] units is the reciprocal of electrical resistivity (ρ) according to:

$$\sigma = \frac{1}{R}\left(\frac{L}{A}\right) \quad ; \rho = R\,\frac{A}{L} \qquad (2\text{-}3)$$

Where L is the wire length of the material and A is the cross-sectional area of the cylindrical pellet.

Additionally, conductivity values were corrected from porosity according to the empirical equation proposed in [89] as follows:

$$\sigma_{fix} = \frac{\sigma_{measured}}{\left[1-\left(\frac{porosity\,\%}{100}\right)\right]^2} \qquad (2\text{-}4)$$

When a thermally activated behavior was observed, the activation energy (E_a) in [eV] was calculated from standard Arrhenius model, where the temperature dependence of the conductivity can be described by the small polaron hopping mechanism [54]; where A is the pre-exponential factor, T is the absolute temperature in [K] and k_B is the Boltzmann constant.

$$\sigma = \frac{A}{T}e^{\left(\frac{-E_a}{k_B T}\right)} \qquad (2\text{-}5)$$

2.2.5. Electrochemical Impedance Spectroscopy measurements

2.2.5.1. Spin coating technique. Spin coating technique was employed in order to coat the electrolyte pellets of BCZY supplied by the Colorado School of Mines (Colorado, USA) with a layer of the electrode material to probe. By this technique, an ink is dropped on the center of the pellet, which is spinned at high speed in order to spread the coating material by a centrifugal force. Deposition was carried out in a VTC-100 Vacuum spin coater and inks were prepared based on the literature [90] and modified in order to obtain a better result depending on our materials. We proceeded to weigh each of the ink components according to Table 3 and deposited them in an agate mortar with constant grinding until a uniform ink was formed.

Table 3. Components for the preparation of the electrode inks

Components	Amount [g]	% Wt
Electrode	0.75	35.63
Isopropanol	0.831	39.48
Terpineol	0.505	23.99
Polyvinylpyrrolidone (PVP)	0.019	0.90

Once the equipment has been assembled (Figure 6), using a 5 mL plastic Pasteur pipette, 3 drops of the ink solution were placed on the surface of the electrolyte while it was spinned under the equipment conditions of 4000 rpm for 20 seconds. After making the deposit, the pellet was dried at 110 °C for 15 minutes, before making a new deposit on top of the previous one in the same conditions. This process was repeated 5 more times and subsequently the same procedure was performed on the opposite side of the electrolyte, *i.e.* 6 layers were deposited on each side of the pellet.

Figure 6. Schematic illustration of the spin coating technique.

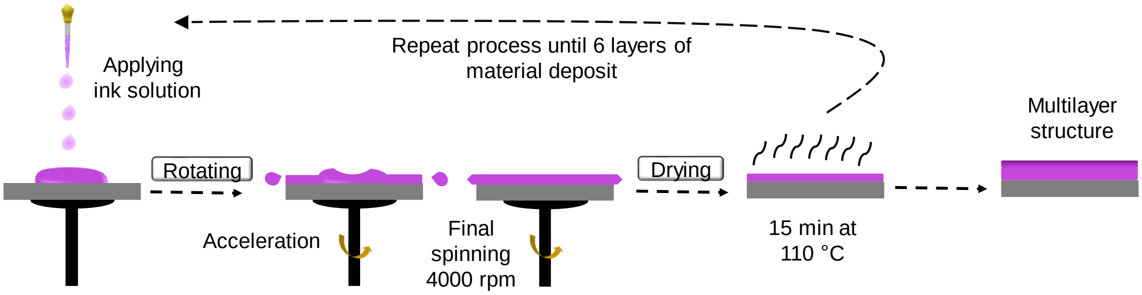

The process of adhesion of the electrode/electrolyte interface was performed at two sintering temperatures of study for the cobalt series (x = 2 and 5): 950 °C (synthesis temperature) and the second one of 50 °C above the synthesis temperature (1000 °C) for 2 hours each. For the manganese series (x = 5) and the cuprate (x = 0) the study was performed at the sintering temperature of 950 °C (synthesis temperature) for 2 hours each, obtaining in all cases a symmetrical cell assembly.

2.2.5.2. EIS experimental conditions. The cells prepared under the conditions mentioned above were introduced in an EIS assembly (ProboStat™ device from NorECs - Norwegian Electro Ceramics AS) as shown in Figure 7.

Figure 7. EIS experimental set up for symmetrical cells.

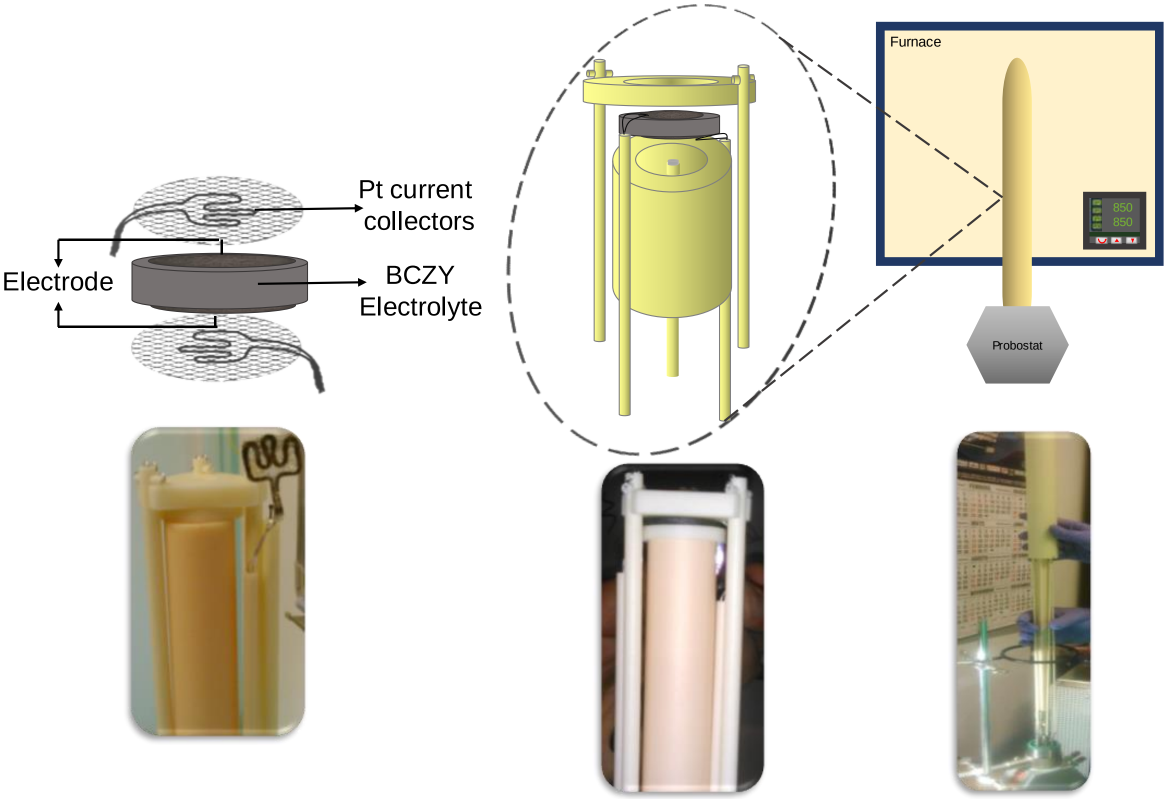

The measurements carried out for the sintering temperature of 1000 °C were performed using a Gamry reference 3000 potentiostat/galvanostat/ZRA equipment, while at the sintering temperature of 950 °C a IviumStat potentiostat/galvanostat. These measurements were taken in a frequency range of 1 mHz to 1 MHz at the open circuit voltage (OCV) with a signal amplitude of 10 mV in an oxidizing atmosphere without gas flow. The tests were carried out in the temperature range 600-800 °C; before starting each measurement, each sample was stabilized at 800 °C until no variation of the impedance spectra was observed. Data were collected then every 50 °C with a cooling rate ramp of 1°C/min, remaining at each temperature a time long enough to obtain consistent impedance spectra.

2.2.5.2.1. Equivalent circuits. The impedance spectra data were normalized with respect to the electrode surface area (0.78 cm^2) in order to fit the spectra to equivalent circuits using Zview software [91], which allowed to condense the information and to transform it into quantitative parameters that are involved in the elementary steps of the electrochemical process.

Figure 8. Illustration of an equivalent circuit that involves one elementary step R_1//CPE_1.

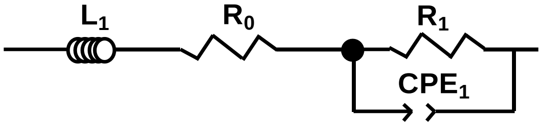

The circuit shown in Figure 8 consists of an inductance (L), that generally is only related to the electrical connections of the device and not to the sample itself, an ohmic resistance (R_0) that is mainly due to the electrolyte conductivity and contact resistances, eventually, and one R_1//CPE_1, that means only one limiting step in the electrode resistance (generally more complex in practice). The latter is composed of a resistance (R_1) and a constant phase element (CPE_1) connected in parallel. The CPE is characterized by two values CPE-T and CPE-p, having a impedance $Z_{CPE} = 1/(T(jw)^P$; P can take values between 0 and 1, when $0.9 \leq P \leq 1$ is related to porous systems, while P= 0.5 is to diffusive process and if P= 1, the response is of a pure capacitor (ideal) [92,93]. In a Nyquist plot, the corresponding spectrum is a depressed semicircle arc (see Annex B).

The capacitance values (C_i) were obtain following the equation [92,94,95]:

$$C_i = R_i^{\frac{1-P_i}{P_i}} T_i^{\frac{1}{P_i}} \tag{2-6}$$

Where T_i is the pseudo-capacitance, R_i is the resistance and P_i is an exponent. With the value of *Ci*, it is possible to calculate the characteristic frequency f_i of each limiting step as:

$$f_i = \frac{1}{2\pi R_i C_i} \tag{2-7}$$

Figure 9. Illustration of an equivalent circuit that involves a Warburg element.

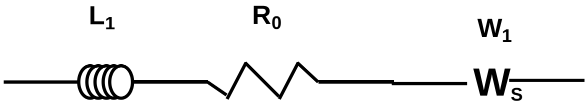

On the other hand, Figure 9 shows a circuit that consists also of an inductance (L), an ohmic resistance (R_0) but with a Warburg element W which impedance is:

$$Z_w = \frac{R\,tanh(jw\,W_T)^{W_P}}{(jw\,W_T)^{W_P}} \tag{2-8}$$

where W_p cannot take values lower tan 0.5, since the characteristic generated spectra corresponds to a straight line with 45° of slope followed by a depressed semicircle in a Nyquist plot [92,93] (see ANNEX B).

In this case, the capacitance values (C) are obtained following the equation [92]:

$$C = \frac{\left(\frac{W_T}{2.53}\right)^{1/2}}{R} \tag{2-9}$$

Where W_T is the pseudo-capacitance and R is the resistance. The characteristic frequency follows:

$$f = \frac{2.53}{W_T} \tag{2-10}$$

Finally, the ASR (area specific resistance in [Ω cm^2]) associated to the electrode polarization is extracted based on the polarization resistance (R_p), which corresponds to the sum of individual resistances R_i present in the circuit; the factor

2 corresponds to the fact that we have a symmetrical cell and A is the electrode surface area (cm^2):

$$ASR = \frac{R_P * A}{2} \tag{2-11}$$

3. RESULTS AND DISCUSSION – THE $La_4BaCu_{5-x}Co_xO_{13\pm\delta}$ SERIES

Previous studies have demonstrated the interest to examine the oxygen vacancy-ordered tunnel-like family based on the structure of the cuprate $La_4BaCu_5O_{13+\delta}$ (referred to as LBCu in this work); this material is stable until 900 °C and counts with a good compatibility with BCG[5] and BZY[6] electrolytes, reasonable TEC value of 17.3×10^{-6} K^{-1} and high electrical conductivity around 500 S cm^{-1} in the 600-800 °C temperature range, making it of special interest as cathode material [74]. Nevertheless, very limited oxygen excess δ was evidenced in the tunnel until at least 700 °C in air in the pure cuprate and such structural feature is of importance for the MIEC behavior of the material. As a consequence, the present work concerns the synthesis and preliminary evaluation of Co substitution in $La_4BaCu_5O_{13+\delta}$, with the aim to possibly increase oxygen non stoichiometry at high temperature in air. A second goal of our study is to compare the cathode behavior of materials with ordered and disordered (cubic-like perovskite) structure, respectively within the $La_4BaCu_{5-x}Co_xO_{13+\delta}$ series.

3.1. STRUCTURAL ANALYSIS BY X-RAY DIFFRACTION (XRD)

The XRD patterns of $La_4BaCu_{5-x}Co_xO_{13\pm\delta}$ materials (x= 0, 1, 2, 3, 4 and 5) are shown in Figure 10, after synthesis by the sol gel method in air, showing the composition range that permit to obtain single phase materials.

---

[5] $BaCe_{0.9}Gd_{0.1}O_{2.95}$

[6] $BaZr_{0.85}Y_{0.15}O_{2.925}$

Figure 10. XRD patterns of $La_4BaCu_{5-x}Co_xO_{13\pm\delta}$ (x=0, 1, 2, 3, 4, 5) after synthesis in air. In inset, zoom on the range 2θ=30-50°.

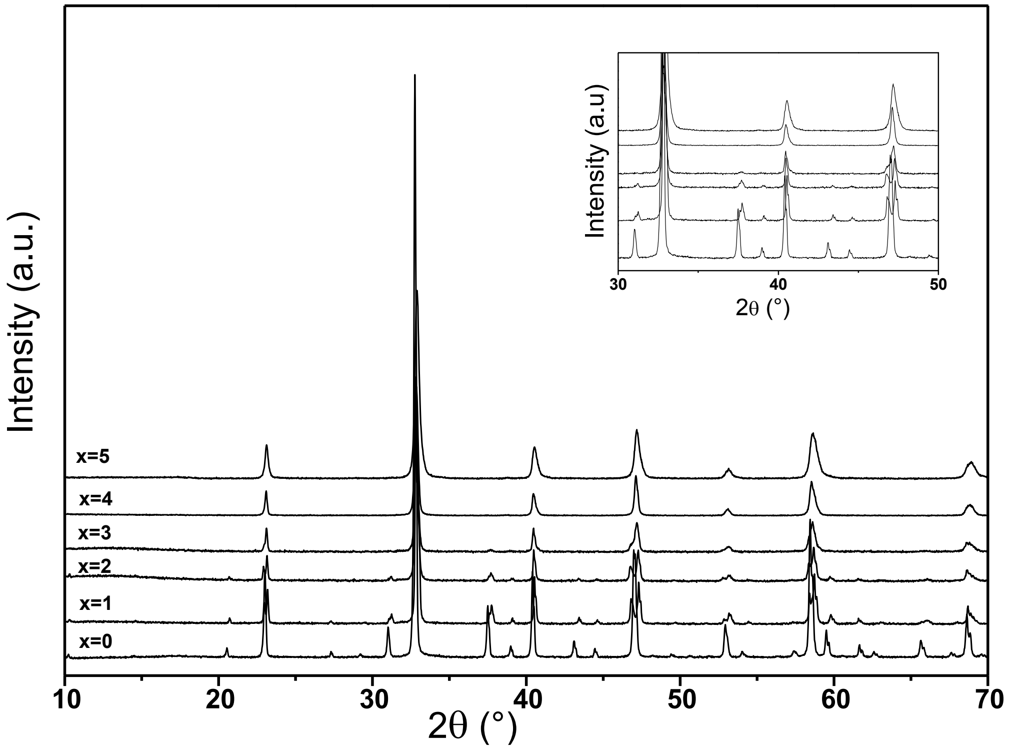

Based on the previous results of Michel *et al.* [16] and the recently cell parameters reported by Macías *et al.* [74] of the ordered structure of the cuprate $La_4BaCu_5O_{13+\delta}$ (LBCu) with space group *P4/m* (a = b = 8.6480(1) Å and c = 3.86101(6) Å), for x=1 and 2 compositions, the XRD patterns can be successfully indexed with a single phase of tetragonal space group *P4/m*. In the inset of Figure 10, we can observe the displacement and disappearance of characteristic peaks as the amount of Co increases. For the x=5 composition, a disordered rhombohedral perovskite with $R\bar{3}c$ space group is formed, which can be explained using as structural model the pure cobaltites $La_{0.8}Ba_{0.2}CoO_{3-\delta}$ [90] or $La_{0.85}Ba_{0.15}CoO_{3-\delta}$ [96] which corresponds to a structure composed of octahedra of Co connected by vertices (Figure 11). Finally, when x= 3 and 4, the two phases coexist.

Figure 11. Rhombohedral structure of the cobaltite perovskite with space group $R\bar{3}c$ [97].

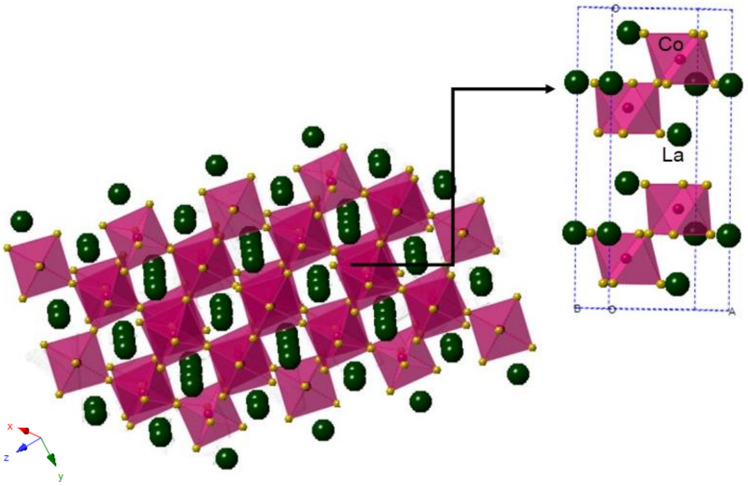

In order to further study those compositions, the value of the lattice parameters and unit cell volume, obtained from the Rietveld refinement (see Annex C) using XRD data, are reported in Table 4 and the graphical evolution of the cell parameters as a function of Co composition in Figure 12.

Table 4. Structural parameters of $La_4BaCu_{5-x}Co_xO_{13\pm\delta}$ after synthesis in air, calculated by Rietveld refinement using XRD data.

x	**Crystal system**	**Space group**	***a* = *b* (Å)**	***c* (Å)**	**V (Å^3)**	**R$_p$**	**R$_{wp}$**	**χ^2**
0	Tetragonal	*P4/m*	8.6478(2)	3.8605(2)	288.70(1)	4.53	5.97	1.96
1	Tetragonal	*P4/m*	8.6015(9)	3.8830(9)	287.29(6)	4.42	5.55	1.62
2	Tetragonal	*P4/m*	8.6031(1)	3.8853(1)	287.57(7)	3.94	4.99	1.39
3	Tetragonal	*P4/m*	8.6190(1)	3.8792(8)	288.18(7)	2.74	3.48	1.45
	Rhombohedral	$R\bar{3}c$	5.4672(1)	13.314(3)	344.6(1)			
4	Tetragonal	*P4/m*	8.6280(2)	3.8660(1)	287.80(4)	2.55	3.18	1.42
	Rhombohedral	$R\bar{3}c$	5.4694(1)	13.307(3)	344.80(2)			
5	Rhombohedral	$R\bar{3}c$	5.4667(7)	13.27(2)	343.69(8)	3.28	4.16	1.36

Figure 12. Evolution of (a) *a*-parameters, (b) *c*-parameters and (c) volume against Co composition in $La_4BaCu_{5-x}Co_xO_{13\pm\delta}$ (a_R and c_R correspond to de Rhombohedral perovskite parameters).

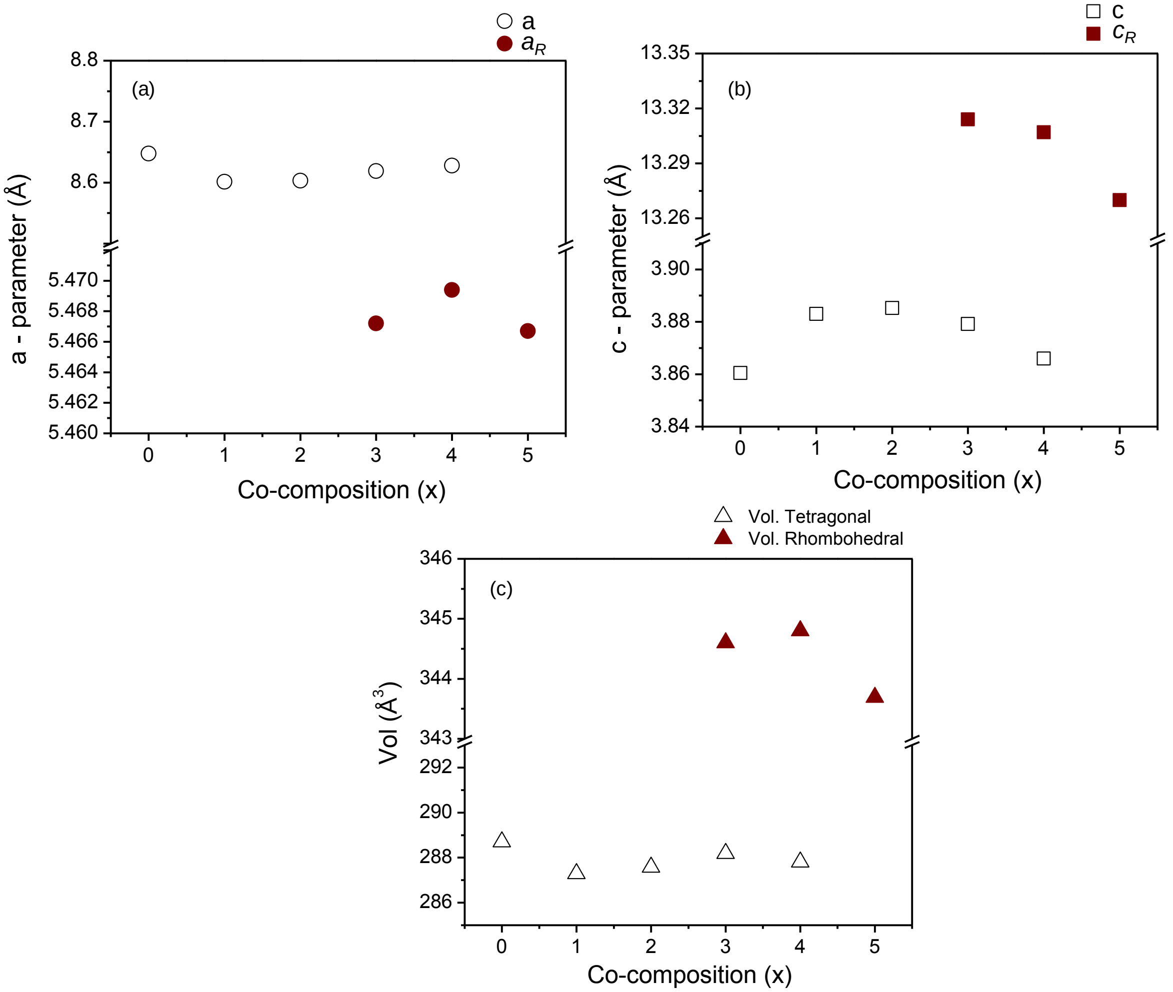

LBCu (x=0) parameters are in good agreement with those reported previously [16,73,74,80] whatever the synthesis technique, *e.g. a*= 8.644(4) Å and *c*= 3.867(3) Å for Michel *et al.* [16]. The minimum deviation of the parameters is due to the slight differences in the oxygen content (13±δ) which depends on the synthesis method. For example, the oxygen stoichiometry of the pure cuprate has been determined as $La_4BaCu_5O_{13.4}$, $La_4BaCu_5O_{12.9}$ or $La_4BaCu_5O_{13.20}$ by Michel *et al.* [16], Anderson *et al.* [73] and Shivakumara *et al.* [80], respectively.

We can observe that, for the tetragonal structure, the *a*-parameter initially decreases from x=0 to x= 1, then remains constant for x=2 before increasing for x>2 (two phases system). On the other hand, the value of c-parameter presents first an increase, but in smaller proportion than for *a*-parameter, a tendency that changes for x≥3, for which *c* slightly decreases with x. The variation of the cell parameters as a function of the composition of Co does not follow a linear relationship that is characteristic of a solid solution probably because of the complexicity of the oxidation state equilibrium between Co and Cu in the series and the presence of a second (perovskite) phase for x>2. As a consequence, the cell volume of the ordered (tetragonal) phase tends to decrease between x=0 and x=1 compositions but doesn´t present a clear evolution for x>1. Such behavior is similar to what was reported by Anderson *et al.* [73] with *a*=*b*=8.6094(4) Å and *c*=3.8861(4) Å for $La_4BaCu_4CoO_{12.98}$; it is worth noting that the same authors could not prepare the x=2 composition as a pure phase, probably due to the use of the solid state synthesis route. In the case of x=5, the obtained parameters are in good agreement with reported values for x=0.2 in $La_{1-x}Ba_xCoO_{3-\delta}$ series [90] with *a*=*b*=5.465 Å and *c*=13.278 Å or the ones by Luo et al. [97], *i.e.* *a*=*b*=5.4658(1) Å and *c* = 13.253(1) Å. On the other hand, the evolution of the cell parameters with x is not in agreement with the results reported by Shivakumara *et al.* [79] where an increase of the cell volume of x= 1 was observed (*a* and *c*-parameter expansion) due to an increase in oxygen content related to the strongly oxidizing medium used (NaOH–KOH fluxes at 450 °C) obtaining an oxygen stoichiometry for x=1 of $La_4BaCu_4CoO_{13.29}$ and $La_4BaCu_4CoO_{13.35}$, calculated by thermogravimetric analysis or iodometric titration, respectively.

For the disordered rhombohedral perovskite, the fact that only one composition (x=5) corresponds to a pure phase does not allow to clearly evidence any cell parameter/volume evolution with x.

Considering those first results, and in particular the formation of pure phases for specific compositions, the rest of our study was dedicated to $La_4BaCu_3Co_2O_{13+\delta}$

(LBCuCo2) and $La_4BaCo_5O_{13+\delta}$ (LBCo) compositions, as representative members of the fully ordered (with highest Co content) and disordered structures, respectively, in comparison to pure cuprate phase LBCu.

3.2. THERMAL STABILITY IN REDUCING ATMOSPHERE

Macias *et al.* [74], reported that LBCu starts to decompose at T~ 500 °C in Ar atmosphere, leading to a phase change that is accompanied by the total or partial destruction of the material phase structure where for LBCu [98]. The thermal stability of LBCuCo2 and LBCo was evaluated in 3% H_2/N_2 at 850 °C during 6 hours. Figure 13 (a) and (b) show the XRD patterns before and after reduction for LBCuCo2 and LBCo, respectively.

Figure 13. XRD patterns before and after reduction at 850 °C of (a) LBCuCo2 and (b) LBCo.

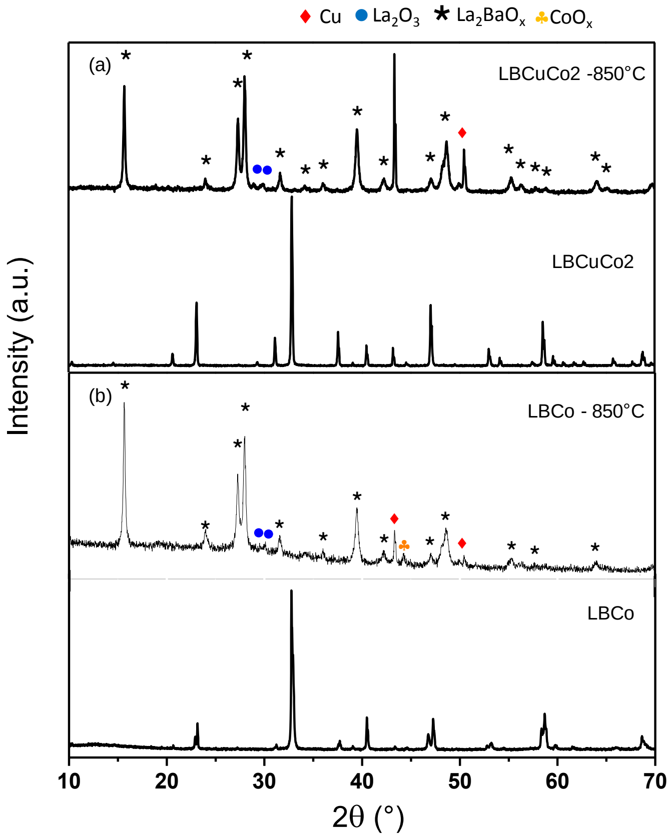

As observed in Figure 13, a complete decomposition of both materials occurs in reducing atmosphere. The test that has been carried out shows the formation of a mixture of phases, leading to the presence of new peaks that do not match with the starting XRD patterns. The different phases were identified with the Crystallographic Search Match software, determining the presence of a Lanthanum Barium Oxide (La_2BaO_x), as well as phases in lower proportion of Copper, cobalt oxide and Lanthanum oxide (La_2O_3), the latter being one of the precursors employed in the synthesis method.

This behavior is quite common for cobalt phases, as the case of $SrFe_{0.7}Co_{0.2}Ti_{0.1}O_{3-\delta}$ which shows a secondary cobalt phase after reduction in 5% H_2/Ar at 700 °C [99] and the $Sm_{0.95}Ce_{0.05}Fe_{1-x}Co_xO_{3-\delta}$ heated at 5% H_2/N_2 at 800 °C [100]. As a conclusion, the presence of Co does not stabilized the system due to the similar reducibility of Co ions as for Cu in reducing atmospheres.

According to this result, we focused the rest of the study concerning Co compositions on oxidizing atmosphere, in order to study the possible application of the material as cathode for a SOFC or IT-SOFC.

3.3. THERMAL BEHAVIOR IN AIR

In order to evaluate the behavior of these compounds at high temperatures in air, a thermo-diffraction test was carried out. The corresponding patterns are shown in Figure 14.

Figure 14. HT-XRD patterns of as-synthetized (a) LBCuCo2 and (b) LBCo from room temperature up to 850 °C in air.

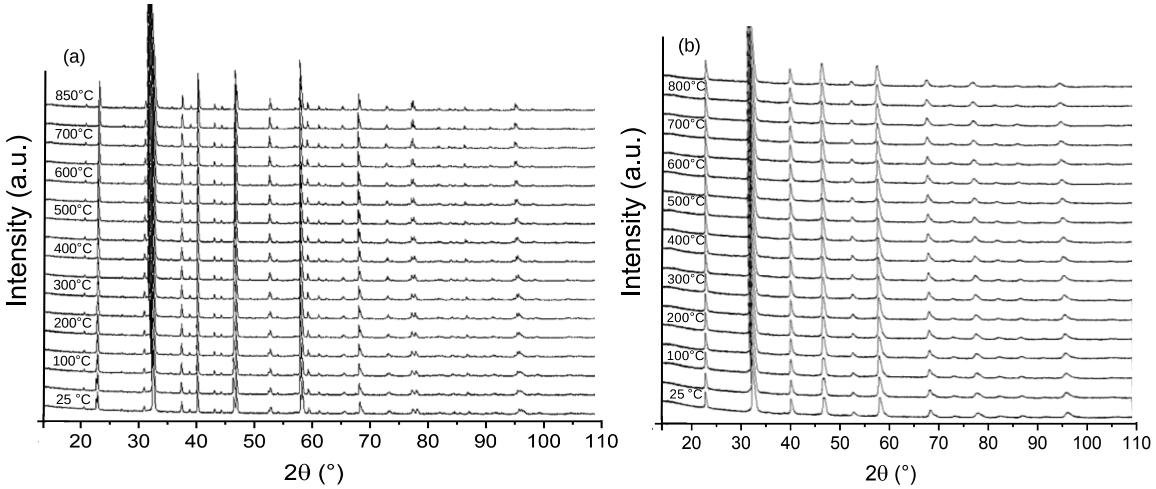

During the heat treatment, in both cases, there is no evidence of peaks corresponding to undesired phases. LBCuCo2 XRD patterns shows an absence of symmetry change in the whole range of temperatures. On the other hand, we observed a symmetry change from rhombohedral to cubic perovskite around 700°C for the pure cobaltite LBCo, that can be evidenced following, in particular, the integrated intensities of (110) peaks around $2\theta \sim 33°$ that becomes unique with temperature, as depicted in Figure 15.

The cell parameters were extracted considering that, for LBCuCo2, the tetragonal *P*4/*m* space group could be indexed to all temperatures and, for LBCo, the patterns were indexed with the rhombohedral (RT-650°C) and cubic cell (700-850°C) with space group $R\bar{3}c$ and $Pm\bar{3}m$, respectively. For comparison, the cell parameters were normalized with respect to the perovskite pristine cell, in which $a_p = a/\sqrt{5}$ for LBCuCo2 and $a_p = a/\sqrt{2}$ and $c_p = c/2\sqrt{3}$ for LBCo (rhombohedral structure).

Figure 15. Variation of symmetry of LBCo with the temperature represented in the peak of higher intensity (2θ~33°).Where 25 °C-1 and 25 °C-2 referers to the RT measurement heating and the cooling cycle, respectively.

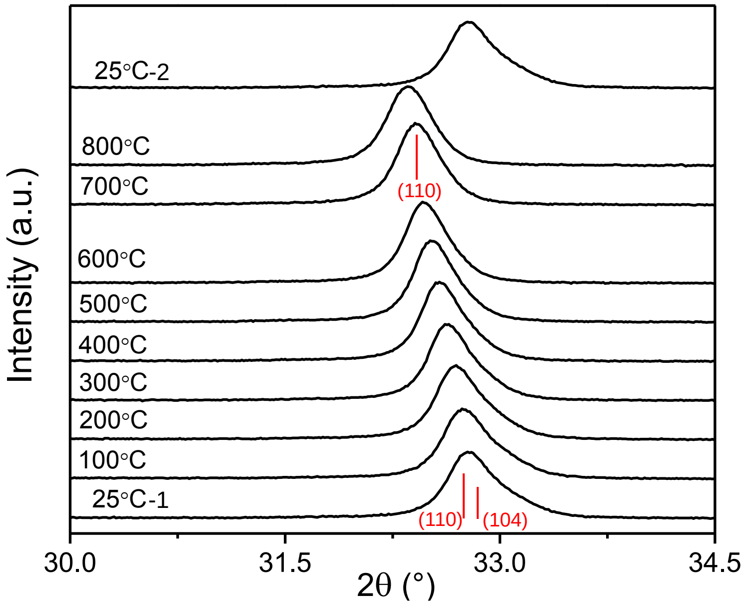

Figure 16. Evolution of the cell parameters as function of temperature for (a) LBCuCo2 and (b) LBCo.

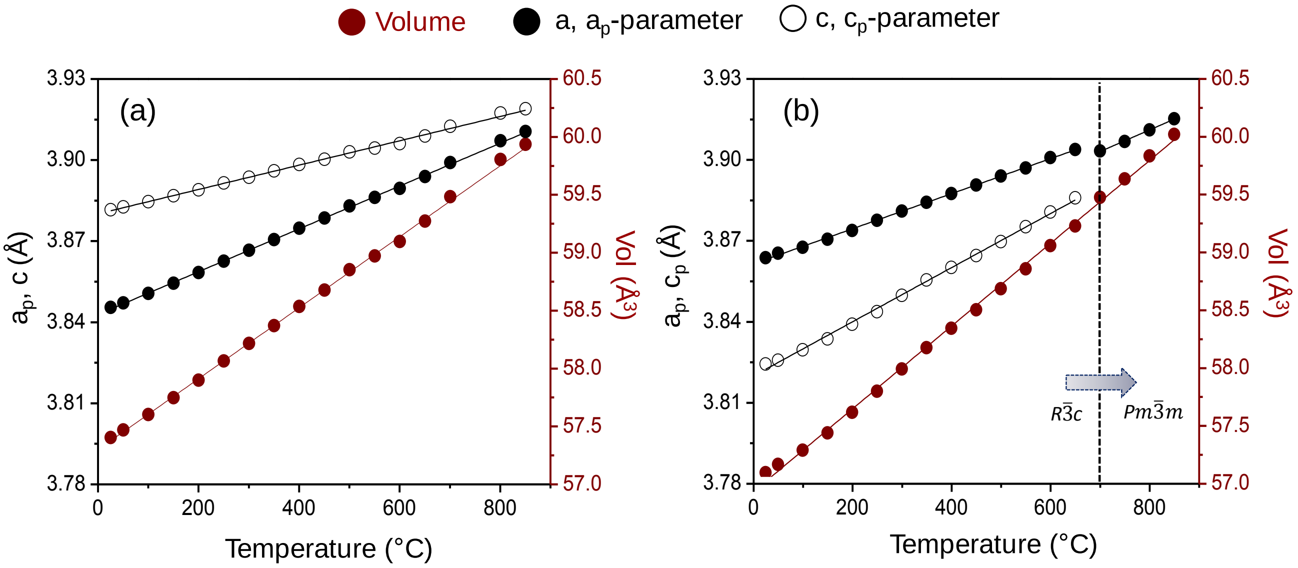

Figure 16 (a) and (b) show the evolution of the normalized cell parameters and volumes for LBCuCo2 and LBCo, respectively. We evidence a linear dependence with temperature for LBCuCo2 and, in the case of LBCo, independently of the structure change around 700 °C (Figure 16(b)). In the case of LBCuCo2, the Thermal Expansion Coefficients (TEC) values in both crystallographic directions *a* and *c* can be obtained from the linear adjustment of the cell parameters with temperature, giving 20.2 x 10^{-6} K^{-1} and 11.3 x 10^{-6} K^{-1}, respectively. Such difference evidences an anisotropic thermal expansion with the *a*-parameter increasing more rapidly than the *c*-parameter. For LBCo, the opposite happens, *i.e.* the *c*-parameter increases much more rapidly than the *a*-parameter, with TEC values of 25.8 x 10^{-6} K^{-1} and 16.6 x 10^{-6} K^{-1}, respectively.

The thermal compatibility of an electrode material with an electrolyte depends on the respective Thermal Expansion Coefficients (TECs). The TEC values have been obtained considering the equation described in section 2.2.3. LBCuCo2 and LBCo present TEC values of 17.3 × 10^{-6} K^{-1}, 19.7 × 10^{-6} K^{-1} (25-650 °C) and 20.4 × 10^{-6} K^{-1} (700-850 °C), respectively. Those values are much higher than typical TEC values for the conventional electrolyte materials use in SOFCs like YSZ (10-11 × 10^{-6} K^{-1}), GDC (12-13 × 10^{-6} K^{-1}), LSGM (11-12 × 10^{-6} K^{-1}) and BCZY (10 × 10^{-6} K^{-1}) [75,102–104], what is unfortunately common for perovskite cobaltites, *i.e.* $La_{0.7}Sr_{0.3}CoO_{3-\delta}$, $Pr_{0.7}Sr_{0.3}CoO_{3-\delta}$, $SmBa_{0.5}Sr_{0.5}CoCuO_{5+\delta}$ and $La_{0.8}Ba_{0.2}CoO_{3-\delta}$ with TEC of 17.5-19.2 × 10^{-6} K^{-1}, 18.8 × 10^{-6} K^{-1} [105], 16.14 × 10^{-6} K^{-1} [62] and 18.2 × 10^{-6} K^{-1} [93], respectively. Concerning the latter value, considering that LBCo can be written as $La_{0.8}Ba_{0.2}CoO_{3-\delta}$, the slight difference of TEC values with literature can be due to the measurement technique (dilatometry) that has been employed in [93].

Despite the high Cu content in LBCuCo2, the TEC value is as high as for pure cobaltite and the high Cu content is not able to mitigate such effect. Indeed, it is worth mentioning that the pure cuprate itself (LBCu) had a TEC coefficient of 17.3 × 10^{-6} K^{-1} [74], what is exactly the same value as for the Co-substituted LBCuCo2 material in this work. Considering the high TEC values, grading electrode can be a possible solution to mitigate such thermal expansion mismatch with the electrolyte, as described in [106] for similar $La_{0.4}Ba_{0.6}CoO_{3-\delta}$ composition.

By subjecting a transition metal cation to a temperature increase, its oxidation state generally tends to decrease in a reduction process. This causes the concentration of oxygen to decrease, with formation of oxygen vacancies. In order to determine the oxygen content as a function of temperature in air, thermogravimetric analyses (TGA) have been carried out. The variation of the non-stoichiometric oxygen content up to 800 °C in air for LBCuCo2 and LBCo was obtained from TGA measurement, considering two consecutive cycles in air (the first one to eliminate the adsorbed species), followed by a destructive reduction cycle in 5% H_2/Ar until 900 °C to obtain the absolute oxygen content.

Figure 17. Thermogravimetric profile for (a) LBCuCo2 and (b) LBCo in air (black and blue curves for the first and second cycles, respectively).

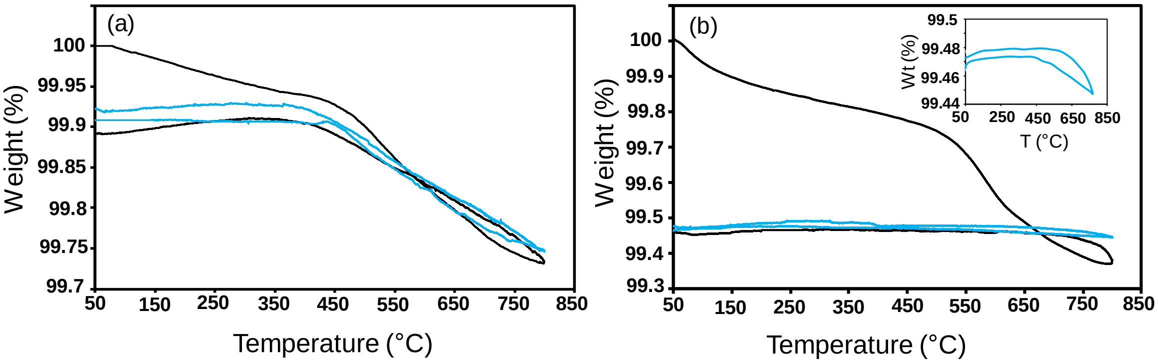

Figure 17(a) and (b) show TG curves in air for LBCuCo2 and LBCo compounds, respectively. In both cases, during the first heating, the materials experience some higher weight losses between Room Temperature (RT) and 700 °C, that are attributed to the desorption of undesirable species (probably H_2O and carbonates). The second cycle in air up to 800 °C indicates that both materials present a weight loss upon heating as a result of the loss of oxygen from the crystal lattice, but in the case of LBCo, we can observe there is no significant weight change, *i.e.* no major variation of oxygen stoichiometry, emphasizing the structural stability of the material in air. Except this point, both samples exhibit the same behavior, the oxygen content decreases as the temperature rises indicating loss of O atoms from the structure. Figure 18(a) represents the oxygen content of LBCuCo2, which correspond to the tetragonal phase of stoichiometry $La_4BaCu_3Co_2O_{13+\delta}$, up to 800 °C. The value of δ is δ= 0.49 at RT and decreases to δ=0.37 at 800 °C, the weight loss occurring mainly for T>450 °C. Additionally, the calculated value of δ= 0.49 of LBCuCo2 at RT is in agreement with the δ=0.1 of $La_4BaCu_5O_{13.1}$ (LBCu) [74] and δ=0.35 for $La_4BaCu_4CoO_{13.35}$ [79], taking into account that Co concentration present in LBCuCo2 is higher, showing that the oxygen content increases with the Co concentration due to generally higher valence of Co with respect to Cu cations in such oxides.

Figure 18. Total oxygen content as function of temperature, in air, for (a) $La_4BaCu_3Co_2O_{13\pm\delta}$ (LBCuCo2) and (b) $La_{0.8}Ba_{0.2}CoO_{3\pm\delta}$ (LBCo)

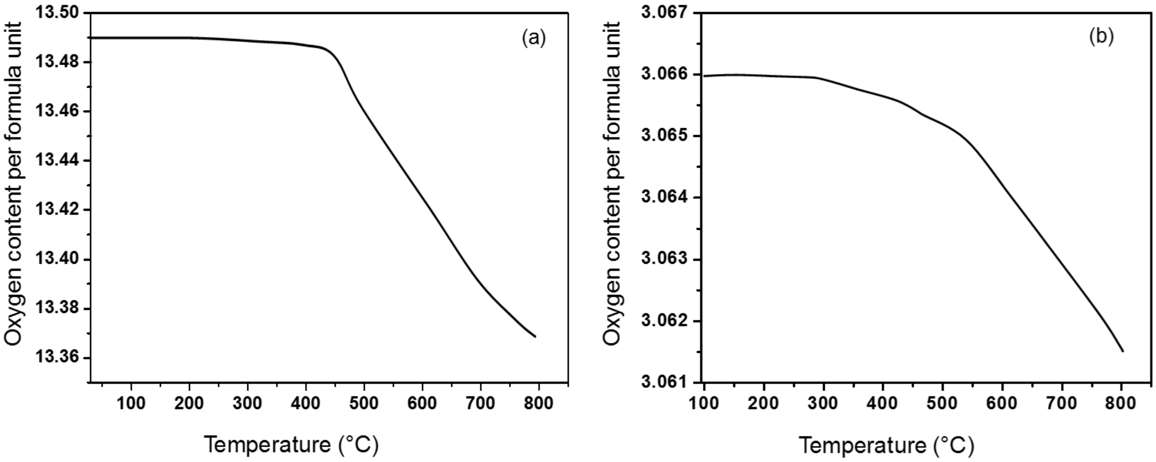

Considering that LBCo can be written as a $La_{1-x}Ba_xCoO_{3-\delta}$ perovskite, and that the oxygen content obtained from titration in H_2 indicates and oxygen excess with respect to perfect ABO_3 perovskite content, the formula can be rewritten as $La_{0.8}Ba_{0.2}CoO_{3.06-\delta}$. Such value of 3.06 is high, but such behavior has been observed in perovskite-like manganites ($La_{1-x}Sr_xMnO_{3-\delta}$) on the range x< 0.2, for which the authors reported an oxygen content that exceed 3 with values of 3.01 to 3.17 [107,108]. Moreover, similar values has been reported, for example in $La_{0.8}Ba_{0.2}CoO_{3-\delta}$ with 3-δ=3.04 [90] or $Pr_{0.7}Sr_{0.3}CoO_{3-\delta}$ (3-δ=3.03) [55]. In the case of LBCo, a nearly continuous but smaller weight loss is observed in air as a function of temperature, which can be associated to the valence of Co reduced from Co^{4+} to Co^{3+} at high temperatures, and is more pronounced for temperatures higher than ~400 °C for which the rate of oxygen vacancy formation increases rapidly and corresponds to an equivalent oxygen loss δ=0.0045 at 800 °C (Figure 18(b)). A similar behavior has been observed in $Sm_{0.7}Sr_{0.3}CoO_{3-\delta}$ [109]. In the case of LBCuCo2, the high concentration of oxygen excess with respect to $A_5B_5O_{13}$ stoichiometry even at high temperature in air is an advantage as such oxygen excess could be associated to enhanced MIEC properties [54,110–114] as it means a much higher oxygen content in the tunnels described in Figure 3 with respect to the pure cuprate [74].

3.4. CHEMICAL COMPATIBILITY WITH ELECTROLYTE

Aiming to detect undesirable phases that could be formed during the electrode elaboration on the electrolyte necessary to prepare samples for the EIS measurements, the chemical reactivity test was studied with BCZY electrolyte at high temperature (1000 °C) for 6 hours, since above >1000 °C LBCuCo2 starts to decompose (see Annex D, Figure D5). It is worth remembering that LBCu compound has been previously found compatible with BCG and BZY similar compositions [74].

Figure 19. XRD patterns after reactivity test in air with (a) LBCuCo2 and (b) LBCo at 1000 °C.

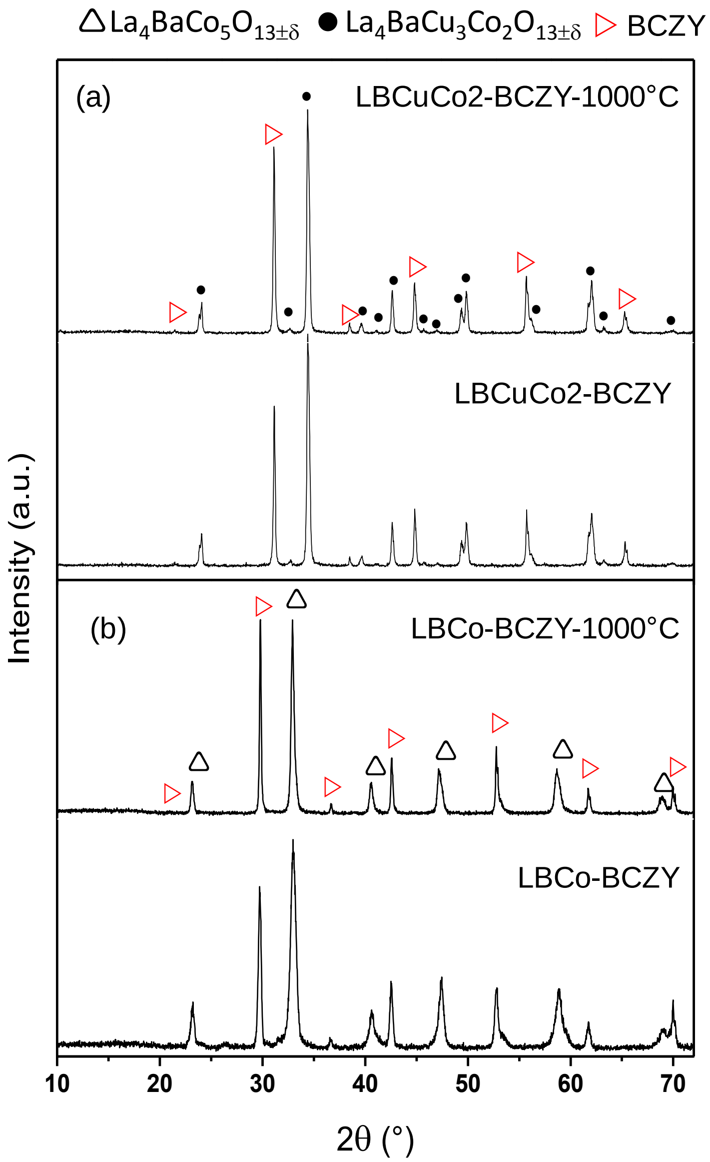

Figure 19(a) and (b) show the XRD patterns for LBCuCo2/BCZY and LBCo/BCZY mixtures before and after the heat treatment in air, respectively. Both materials remain globally unchanged as no additional peaks or major modification of XRD pattern is observed after test. Structure refinements using the XRD data (see Annex D) show a slight variation of the lattice parameters and volume of the cell, summarized in Table 5, confirming the good chemical compatibility of the cobalto-cuprate compounds with BCZY electrolyte at high temperature.

Table 5. Structural parameters of mixtures before and after the reactivity test between LBCuCo2 or LBCo with BCZY in air, using XRD data.

	Before treatment		**After treatment**		**Before treatment**		**After treatment**	
			1000 °C				**1000 °C**	
	LBCuCo2	BCZY	LBCuCo2	BCZY	LBCo	BCZY	LBCo	BCZY
a (Å)	8.600(3)	4.250(1)	8.62(1)	4.244(2)	5.464(3)	4.249(2)	5.467(3)	4.253(1)
c (Å)	3.884(2)	4.250(1)	3.879(2)	4.244(2)	13.274(9)	4.249(2)	13.280(7)	4.253(1)
***V* (Å^3)**	287.3(2)	76.81(4)	288.4(4)	76.44(7)	343.2(4)	76.73(6)	343.7(3)	76.93(5)
R_p	21.60		10.1		11.60		11.6	
R_{wp}	22.90		14.1		17.30		16.8	
χ^2	1.25		1.28		1.57		1.63	

The slight increase of LBCuCo2 and LBCo cell volume after heating can be a consequence of the cationic interdiffusion that could occur between the cations of the electrode and the electrolyte materials. In both cases, there is a possibility that some large ions *i.e* Ce^{4+}, Zr^{4+} or Y^{3+} ($R^{IX}_{Ce^{4+}}$=1.02 Å, $R^{IX}_{Zr^{4+}}$=0.89 Å, $R^{VI}_{Y^{3+}}$=1.075 Å [115]) substitute the position of smaller Co^{3+} or Co^{4+} cations ($R^{VI}_{Co^{3+}}$=0.61 Å, $R^{VI}_{Co^{4+}}$=0.53 Å [115]). If the presence of the small $Co^{3+/4+}$ cations at the B site of BCZY can explain the decrease of cell volume after the treatment in the case of LBCuCo2+BCZY mixture; on the other hand, the BCZY cell volume increase in the case of LBCo+BCZY could be a consequence of the preferential diffusion of Zr^{4+} from the electrolyte with respect to Ce^{4+} or Y^{3+} as the former cation is smaller than the two others or the substitution by a larger cation like La^{3+} ($R^{IX}_{La^{3+}}$=1.216 Å [115]); Ba is no consider in the interdifussion since it is present in both structures have it. However, a complementary technique such as FIB-SIMS

(*Focused ion beam secondary ion mass spectrometry*) must be done in order to confirm the above.

3.5. CONDUCTIVITY MEASUREMENTS

Figure 20 shows the evolution of the electrical conductivity of LBCuCo2 as a function of temperature up to 800 °C in air, as well as the inset that represents the evolution of the conductivity using an Arrhenius plot in the low temperature region where the conductivity is thermally activated. Contrary to the pure cuprate [74] which exhibits a pure metallic-type behavior, the Co-doped cuprate (LBCuCo2) presents at low temperature (up to 400 °C) a semiconductor-type behavior; in this case the conductivity increases as the temperature rises starting with a value of σ = 495 S cm^{-1} at 60 °C and reaching its maximum of σ = 780 S cm^{-1} at 400°C. Such dependency is followed by a decrease down to σ = 560 S cm^{-1} at 800°C, exhibiting a metallic-like behavior.

Figure 20. Temperature dependence of the total conductivity of La$_4$BaCu$_3$Co$_2$O$_{13\pm\delta}$ (LBCuCo2) in air.

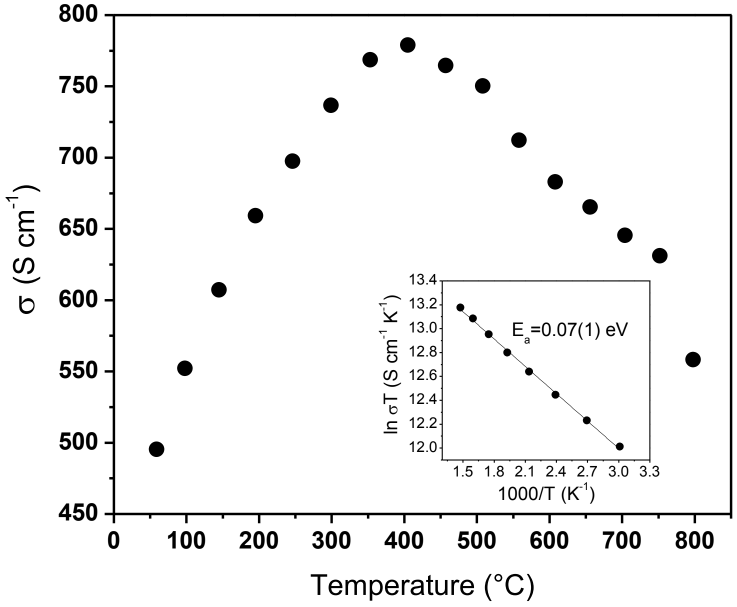

Ordered like cobaltites such as $GdBaCo_2O_{5+x}$ show a typical semiconductor-type [116]. The inset presents the Arrhenius plot corresponding to the low temperature conductivity curve, in the range of 60-460°C, that allows to extract a low activation energy value of E_a = 0.07(1) eV. Such value is slightly higher but similar to what is observed for example in $PrBaCo_2O_{5+\delta}$ (E_a = 0.04 eV) and suggests a temperature activated hole small polaronic mobility [117][111]. Indeed, the decrease of conductivity for temperatures above 400 °C could be related to the cobalt reduction (associated to oxygen vacancy formation) observed by TGA data the oxygen loss starts ~400 °C (in section 3.3). Such kind of phenomenon has been observed in literature for temperature values approximately greater than 400 °C [12–14]. Similarly, Cu-substituted materials generally decreases the electronic conductivity as the temperature rises showing a typical metallic-like behavior reaching maximum values in the range 200-500 °C [13]. The conductivity and behavior (temperature dependency) of LBCuCo2 is in good agreement with $La_{0.5}Ba_{0.5}CoO_{3-\delta}$ (x= 0.5) composition studied by other authors in the temperature range of a SOFC [113] passing from a metallic to a semiconducting behavior.

LBCo electrical conductivity has not been measured, considering that several works report the electrical behavior in air of the $La_{1-x}Ba_xCoO_{3-\delta}$ perovskites [97,106,111,113]. For example, Luo *et al.* [97], and Kriener *et al.* [118], reported the conductivity within the series up to 300 K, evidencing for compositions x> 0.18 or x≥ 0.25, respectively, that the Ba-doped samples are metallic above ~100 K, this latter being the critical temperature for the metal-insulator transition depending on the composition [97]. Such behavior has also been observed in the $La_{1-x}Sr_xCoO_{3-\delta}$ system, in which $La_{0.8}Sr_{0.2}CoO_{3-\delta}$ exhibits a metallic behavior with σ= 1338 S cm^{-1} at 800 °C [119]. Setevich *et al.* explained that the pseudometallic behavior of $La_{1-x}Ba_xCoO_{3-\delta}$ up to 900 °C can be explained by the formation of oxygen vacancies above T= 400 °C (similar to what has been already described in section 3.3) where, for all samples with x≤ 0.7, the conductivity decreases when the temperature raises. Such dependency is related to the reduction of cobalt from Co^{4+} to Co^{3+}, *i.e.* the diminution of the hole concentration. Despite this fact, at 800 °C, a conductivity value of $\sigma \sim 300$ S cm^{-1} has been mentioned for x= 0.3, 0.5 and 0.6 [93], that is more than sufficient for the considered application. It is therefore highly possible that such conductivity level can be reached for LBCo ($La_{0.8}Ba_{0.2}CoO_{3-\delta}$) composition.

3.6. ANALYSIS OF THE ELECTROCHEMICAL PROPERTIES (EIS)

From the above study, LBCuCo2 and LBCo present sufficient total electrical conductivity in oxidizing atmosphere as well as chemical compatibility and themomechanical with the yttria-doped barium zirconocerate (BCZY) electrolyte. This section describes the electrochemical behavior as cathode material for Symmetrical Solid Oxide Fuel Cell (SSOFC) in air of both cobaltites, in comparison to the pure cuprate (LBCu). In all cases, the data were analyzed with equivalent circuits that are associated to the limiting processes that possibly occur at the electrodes. It is worth noting that the measurements in this work were not very accurate; indeed, some of the circuits presented in the literature where used since the impedance spectra showed a similar asymmetric shape, however, the results based on the literature circuits [8,9,62,90,92,120,121] did not present a good fit; therefore, the circuits proposed in this work were implemented finding a better fit. It should be noted that although the fits presented are not of the better quality, we wanted to give a quantitative and qualitative explanation in order to associate the physical phenomena that could be occurring in the electrodes. For this reason, the study is considered as preliminary results aiming to know the influence of the sintering temperature on the system response.

The preparation conditions for the cells have been described in section 2.2.5. Both cobalt-containing electrodes performance have been evaluated at the sintering temperatures of 950 and 1000 °C, considering that sintering conditions have an aftereffect on electrochemical performance due to the influence of temperature on the adhesion between the electrode and the electrolyte but also on ceramic sintering and grain coarsening. In contrast, LBCu electrode was only sintered at 950 °C, since LBCu materials starts to decompose above this temperature. Additionally, in view of the description of the processes that contributes to the polarization resistance R_p, the EIS spectra were fitted to equivalent circuits employing Zview software [91], that allowed to transform the data into quantitative parameters (*i.e.* capacitance, characteristic frequency and area specific resistances (ASR)), following the equations also described in section 2.2.5. For clarity, the series resistance R_s that corresponds to the ohmic resistance and is mainly due to the electrolyte and the contact resistance, has been removed from all the figures shown in this section in order to obtain a better comparison; the values are shown in the corresponding tables.

3.6.1. Reference composition LBCu. As shown in Figure 21 (a), at all temperature between 600 and 800 °C, the obtained impedance spectra of the cuprate sample sintered at 950 °C are asymmetric in shape, indicating that more than one limiting step maybe take place for the electrode process. Figure 21 (b) shows a spectrum obtained at 650 °C and its corresponding equivalent circuit, which was thereafter applied in the whole temperature range (see ANNEX E). The equivalent circuit is composed of an inductance (L) in series with an ohmic contribution of the cell (R_S) and two (R_i // CPE_i) elements consisting of a resistance (R_i) in parallel with a constant phase element (CPE_i); such circuit allowed to obtain the values of capacitance (C), characteristic frequency (f) and area specific resistance (ASR). From Figure 22(a), we can see that the overall ASR values are relatively large in comparison to values reported for cathodes at similar temperatures; for instance, at 800 °C the ASR is 0.904 Ω cm^2 for LBCu, in contrast with the 0.0378 Ω cm^2 of $SmBa_{0.5}Sr_{0.5}CoCuO_{5+\delta}$ [62] or 0.43 Ω cm^2 of LSCM [122] or 0.125 Ω cm^2 of LSCu [123]. As normally the case, and because of temperature activated limiting phenomena, the ASR increases with T, following globally an Arrhenius behavior; the overall activation energy obtained from the ASR is 1.70(3) eV. This activation energy is high compared to other cuprates such as $SmBa_{0.5}Sr_{0.5}CoCuO_{5+\delta}$ (1.13 eV) [62], $Ba_{0.5}Sr_{0.5}Fe_{0.8}Cu_{0.2}O_{3-\delta}$ (1.17 eV) [124], and such E_a does not probably meet the fundamental requirement of a good oxygen-ion conductor (MIECs) which E_a has to be less than ~ 1.036 eV [125]. Into details concerning the limiting processes, we can say in a first instance that both resistive components contribute to the polarization resistance as depicted in Figure 22(b). For example, at 650 °C the R_p value is 39.26 Ω cm^2, from which R_1 is 19.03 Ω cm^2 and R_2 is 20.23 Ω cm^2, indicating that each contribute with a ~ 50% to the total resistance.

Figure 21. (a) Impedance spectra measured in air between 600 and 800 °C for LBCu cathode sintered on BCZY at 950 °C for 2h in air. (b) Experimental and simulated impedance spectra measured at 650 °C in air for LBCu cathode. The numbers correspond to the logarithm[7].

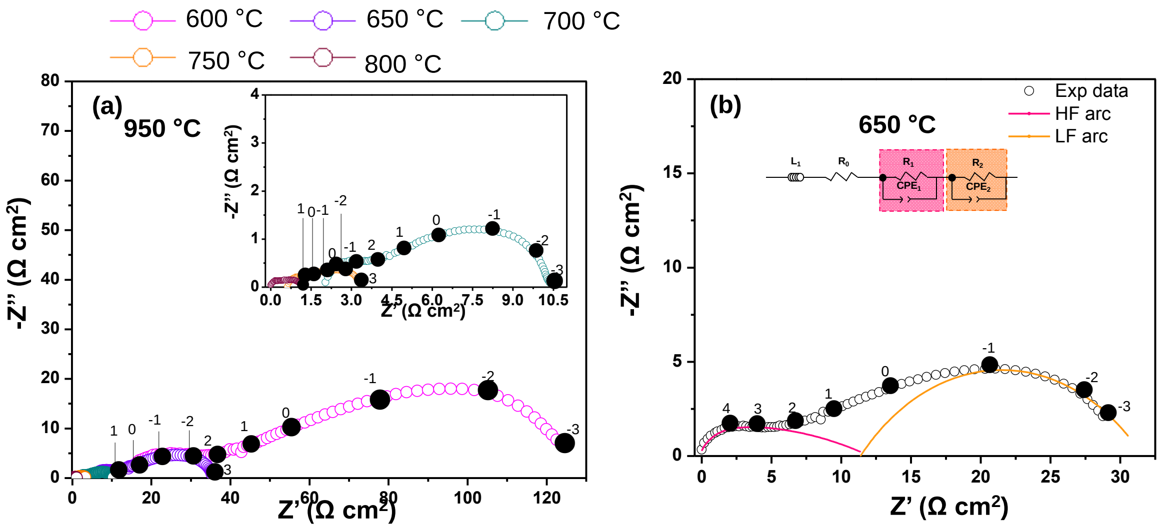

---

[7] To be able to compare easily the variation of R_p

Table 6. Quantitative parameters for LBCu electrode sintered at 950 °C measured in air

T	**R_S**	**HF**			**LF**			**Rp**	**ASR**	χ^2
		R_1	**C_1**	***f***	**R_2**	**C_2**	***f***			
(°C)	**(Ω cm^2)**	**(Ω cm^2)**	**(F cm^{-2})**	**(Hz)**	**(Ω cm^2)**	**(F cm^{-2})**	**(Hz)**	**(Ω cm^2)**	**(Ω cm^2)**	
600	258.7	66.84	7.41E-07	3215.13	78.66	5.59E-02	0.036	145.5	72.75	9.6E-05
650	156.7	19.03	1.58E-06	5295.34	20.23	6.89E-02	0.1143	39.26	19.63	3.2E-03
700	99.07	5.7	2.79E-06	9994.47	5.443	9.45E-02	0.3093	11.143	5.5715	4.4E-05
750	66.66	1.538	8.76E-06	11814.83	2.056	9.83E-02	0.7873	3.594	1.797	1.9E-05
800	58.53	1.13	5.42E-06	25983.44	0.67807	6.93E-02	3.3814	1.80807	0.904035	3.7E-06

Figure 22. Arrhenius plot of the (a) area specific resistance (ASR) and (b) individual resistances for LBCu cathode sintered at 950 °C and measured in air.

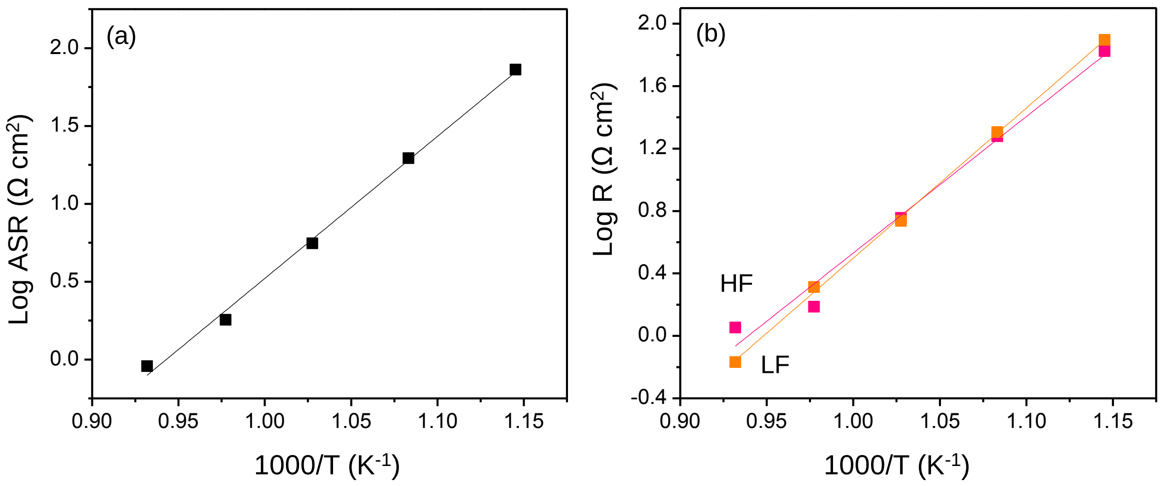

The quantitative parameters, capacitance (C) and characteristic frequency (f), are useful parameters that enables to identify the electrode processes. As shown in Figure 22 (d), the capacitances vary significantly with the temperature in which the HF values are in the range of 10^{-7}–10^{-6} F cm^{-2} and the LF values of 10^{-2} F cm^{-2}, while the characteristic frequencies decreased in almost two orders of magnitude as the temperature decreases. Based on the literature, the HF process can be associated to a charge transfer that could be the electron transfer with ionic incorporation into the electrode [92], this limiting process with capacitances around 10^{-6} F cm^{-2} has been identified in LSCu ($La_{0.7}Sr_{0.3}CuO_{3-\delta}$) in the same range temperature (600-800 °C) sintered at 950 °C [126]. The capacitance values of 10^{-2} F cm^{-2} of LF region could be related to a surface phenomenon as for example dissociative adsorption of oxygen and/or surface diffusion of adsorbed oxygen species (Oad) [92,126–128]. Other possibility, especially considering the low frequency range in which the limiting step occurs, could be the formation of secondary phases at electrode/electrolyte interface as described in [129] even if chemical reactivity study didn't give evidence of such phenomenon. Some more work would be required to definitively prove or discard such hypothesis, especially using TEM studies at the interface between the two components.

3.6.2. LBCuCo2. The effect of the sintering temperature on the electrochemical behavior of an electrode material is important: low temperatures generally allows to keep a large surface area within the porous electrode, what is favorable for the limiting steps related to surface area like adsorption phenomena, but generally leads to a poor electrode/electrolyte contact and grain cohesion within the same electrode layer. In contrast, high temperatures generate a better electrode grains cohesion and electrode-electrolyte adhesion but an increase in grain size, therefore, can decrease is the specific surface area [130]. That's why we decided to optimize the electrode sintering temperature as the main factor of electrode elaboration process. Unfortunately, no higher sintering temperatures than 1000 °C could be used since LBCuCo2 starts to decompose at 1050 °C as shown previously in section 3.4.

The impedance spectra for LBCuCo2/BCZY/LBCuCo2 cells sintered at 950 and 1000 °C are shown in Figure 23.

Figure 23. Impedance spectra measured in air between 600 and 800 °C for LCuBCo2 cathodes sintered on BCZY at (a) 950 and (b) 1000 °C for 2h in air. The serial resistance (R_s) has been removed[8].

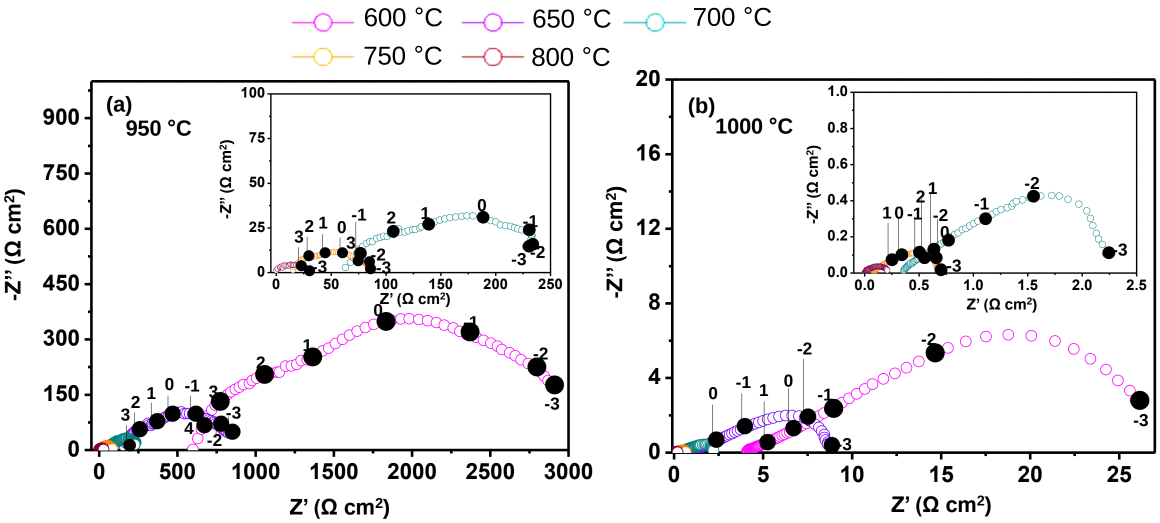

As presented in Figure 23, the different arcs that describe each spectrum are not the same for each cell, in particular their characteristic frequency range and, at a first glance, the effect on the R_p (electrode polarization resistance) of the sintering temperature is quite clear, *i.e.* the higher the temperature, the better the polarization resistance.

Figure 24 shows an example of an EIS spectra obtained at 650 °C for both sintering temperatures. In both cases, an asymmetric shape is observed and can be associated to more than one elementary step presented in the electrode process. In the whole temperature range, the impedance data corresponding to the electrode sintered at 950 °C (Figure 24(a)) were adjusted using an equivalent circuit composed of an inductance (L) in series with an ohmic contribution of the cell (R_s) and two

---

[8] To be able to compare easily the variation of R_p

elements (R_i // CPE_i) consisting of a resistance (R_i) in parallel with a constant phase element (CPE_i). For the electrode sintered at 1000 °C (Figure 24 (b)), the impedance data in the range 600-800 °C were adjusted using an equivalent circuit composed of an inductance (L) in series with an ohmic contribution of the cell (R_s), one element (R_1 // CPE_1) consisting of a resistance (R_1) in parallel with a constant phase element (CPE_1) and a Warburg element (W_2). The choice of a Warburg over a R_i // CPE_i element is due to the better quality of the fits using Warburg element. These circuits allowed to obtain the values of capacitance (C), characteristic frequency (f) and area specific resistance (ASR), ANNEX F and ANNEX G shows the simulated impedance spectra of the remaining temperatures of the electrodes sintered at 950 and 1000 °C, respectively. Table 7 and Table 8 list the quantitative parameters obtained from the spectra simulation.

Figure 24. Experimental and simulated impedance spectra measured at 650 °C in air for LBCuCo2 cathode sintered at (a) 950 °C and (b) 1000 °C on BCZY. The numbers correspond to the logarithm of frequency. The serial resistance (R_s) has been removed[9]

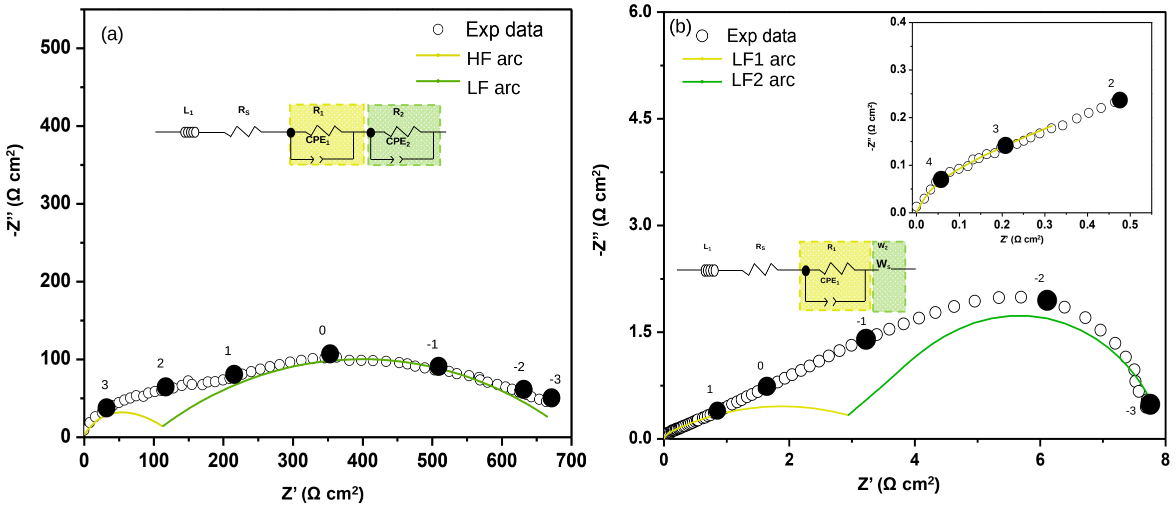

In Figure 25, the evolution of global ASR for each sintering temperature is plotted as a function of temperature of measurement, using an Arrhenius representation. The

---

[9] To be able to compare easily the variation of R_p

increase of the sintering temperature leads to a noticeable decrease of ASR values; for example, at 800 °C from 22.06 Ω cm^2 to 0.1324 Ω cm^2 for the electrodes sintered at 950 and 1000 °C, respectively. In addition, the activation energies (E_a) were obtained from the Arrhenius plot of the ASR as function of temperature, with values of 1.7(5) and 1.8(9) eV at 950 and 1000 °C, respectively, showing again that the temperature has a dramatic effect on the electrode limiting steps. These activation energies are higher compared to values for ordered cobaltites, in particular for the LBCuCo2 electrode sintered at 1000 °C. For example, E_a is 0.96 eV for $GdBaCo_2O_{5+\delta}$, symmetrical cell assembly on a SDC (Samaria-Doped Ceria) electrolyte as reported by Li *et al*. [9] and a value of 1.13 eV has been reported for the cobalto-cuprate $SmBa_{0.5}Sr_{0.5}CoCuO_{5+\delta}$ sintered also at 950 °C on both LSGM and GDC electrolytes [62].

Figure 25. Arrhenius plot of area specific resistance (ASR) for LBCuCo2 electrodes sintered at 950 and 1000 measured in air.

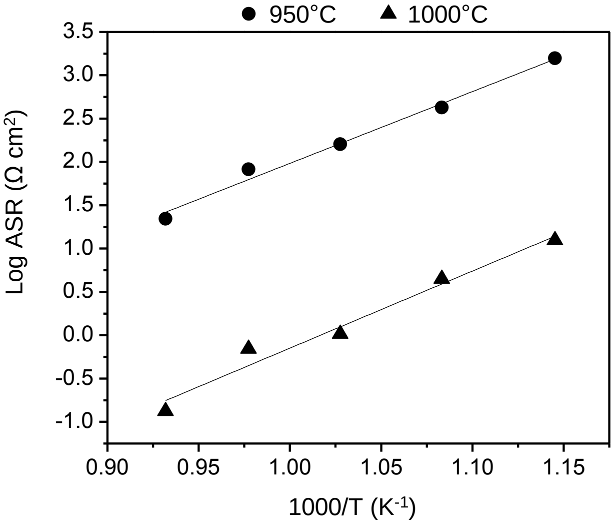

As reported for $GdBaCo_2O_{5+\delta}$ by Li *et al.* [9], the origin of high ASR values for the electrode sintered at 950 °C could be the poor adhesion of the electrode to the electrolyte; the sintering temperature affects the adherence of the cathode to the electrolyte. Using a sintering at 950 °C the cathode layer can be easily peeled off the electrolyte, therefore the cathode performance is deteriorated. The authors concluded that the best electrochemical performance is obtained for T > 950 °C with much lower polarization resistances; on the other hand, Chang *et al.* [131], and Kim *et al.* [132], suggested to attach the same electrode ((Gd,Sm)$BaCo_2O_{5+\delta}$) in conditions of T ≤ 1000 °C since at 1000 and 1050 °C a noticeable degradation on the performance was seen. As observed in Figure 24, the change in the impedance spectra is observed by the presence of a HF contribution for the low sintering temperature, which almost disappears in the case of the electrode prepared at 1000 °C. A relatively low frequency (LF) contribution is the main limiting element for the sintering temperature of 950 °C and decreases also dramatically for T=1000 °C, what makes appear a low frequency (LF1) phenomenon and another Warburg-type contribution at even lower frequency (LF2).

Figure 26. Arrhenius plot of the individual resistances for LBCuCo2 cathode sintered at (a) 950 and (b) 1000 °C and measured in air.

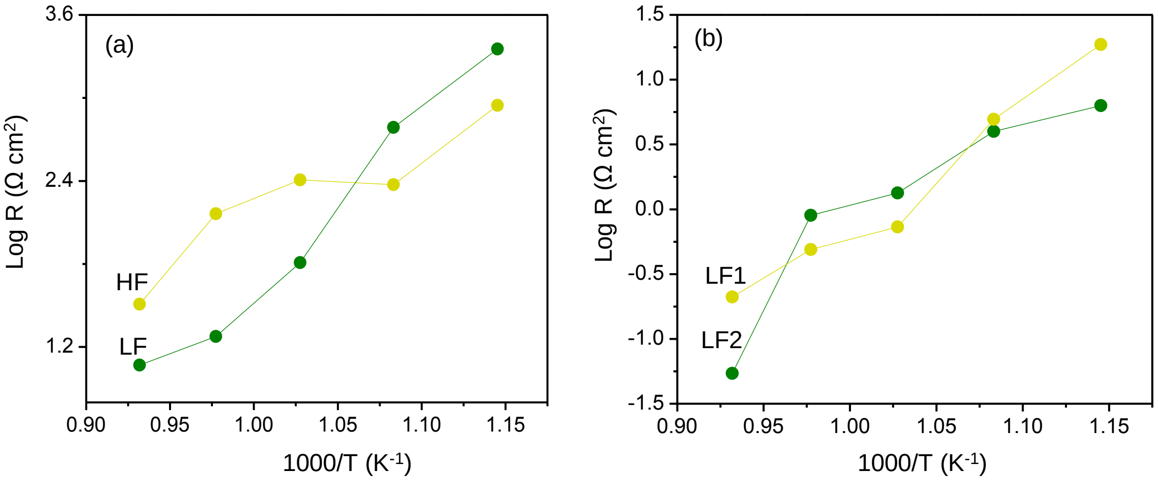

As shown in Figure 26(a) and Table 7, for the electrode sintered at 950 °C, the main contribution at high measurement temperature is the High Frequency (HF) limiting step but such tendency changes in the range T<700 °C for which the LF contribution is predominant. This is due to the difference of activation energy of each limiting step which is found to be E_a (HF)= 1.5(3) eV and E_a (LF)= 2.3(1) eV, respectively. On the other hand, for the electrode sintered at 1000 °C (Figure 26 (b), Table 8), the LF1 and LF2 resistances contribute almost in the same proportions to the global ASR.

Table 7. Quantitative parameters for LBCuCo2 electrode sintered at 950 °C measured in air

T	**R_S**	**HF**			**LF**			**Rp**	**ASR**	χ^2
		R_1	**C_1**	***f***	**R_2**	**C_2**	***f***			
(°C)	**(Ω cm^2)**	**(Ω cm^2)**	**(F cm^{-2})**	**(Hz)**	**(Ω cm^2)**	**(F cm^{-2})**	**(Hz)**	**(Ω cm^2)**	**(Ω cm^2)**	
600	3475	885.3	2.00E-8	8519.85	2260	1.6E-4	0.439	3145.3	1572.65	1.3E-04
650	2658	236.4	4.01E-7	1678.13	612.3	5.3E-4	0.49	848.7	424.35	1.7E-04
700	1541	256.1	4.51E-7	1378.72	64.46	2.46E-3	1.004	320.56	160.28	2.4E-05
750	925.6	145.5	5.08E-7	2154.14	18.9	8.36E-3	1.01	164.4	82.2	3.6E-05
800	645.6	32.37	5.82-6	844.48	11.75	1.51E-2	0.9	44.12	22.06	6.2E-05

Table 8. Quantitative parameters for LBCuCo2 electrode sintered at 1000 °C measured in air.

T	**R_S**	**LF1**			**LF**			**Rp**	**ASR**	χ^2
		R_1	**C_1**	***f***	**W_2**	**C_2**	***f***			
(°C)	**(Ω cm^2)**	**(Ω cm^2)**	**(F cm^{-2})**	**(Hz)**	**(Ω cm^2)**	**(F cm^{-2})**	**(Hz)**	**(Ω cm^2)**	**(Ω cm^2)**	
600	51.91	6.298	0.28	0.09	18.71	0.26	0.04	25.01	12.503	2.4E-04
650	37.9	3.995	0.34	0.12	4.937	0.71	0.08	8.932	4.466	1.2E-04
700	26.96	1.336	0.34	0.35	0.732	2.56	0.13	2.067	1.034	8.7E-05
750	18.82	0.8996	0.32	0.71	0.4889	4.15	0.23	1.388	0.6943	3.5E-05
800	15.95	-	-	-	0.277	4.29	0.70	0.264	0.1324	3.3E-06

According to the literature, the HF phenomenon observed for the electrode sintered at 950 °C corresponds to capacitance values around 10^{-6} F cm^{-2} at 800 °C and should correspond to a charge transfer phenomenon, possibly to the electron transfer with ionic incorporation into the electrode, like in the case of LBCu (see section 3.6.1.) despite the slight difference of the activation energies E_a = 1.6(6) eV for LBCu and E_a = 1.5(3) eV for LBCuCo2. Another possibility would have been a limitation due to oxide-ion transfer through electrolyte grain boundaries [129], due for example to a diffusion from the electrode to the electrolyte but if it is the case, such contribution would have been also present for higher sintering temperature; in this case, the first hypothesis seems more convincing. For the LF contribution, also similar to what is found for the Co-free LBCu electrode (see section 3.6.1.), the capacitance values from around 10^{-2} F cm^{-2} at 800 °C to around 10^{-4} F cm^{-2} at 600 °C seems to correspond to surface phenomena as for example dissociative adsorption of oxygen and/or surface diffusion of adsorbed oxygen species (Oad) [127,128]. Such processes have been identified in SBSCCo ($SmBa_{0.5}Sr_{0.5}CoCuO_{5+\delta}$) sintered at 950 °C in the same temperature range (600-800 °C) on GDC electrolyte [62,92]. As for LBCu, another hypothesis would be the formation of secondary phases at electrode/electrolyte interface [129]. Nevertheless, in both cases, it is not clear why the same limiting step(s) is(are) not clearly present in the same, or even a higher extent for the electrode sintered at 1000 °C. Indeed, for the electroactive layer prepared at 1000 °C, the absence of HF phenomenon means the processes of charge transfer have been improved, probably because of better interphase between the electrode and the electrolyte that is directly related to higher sintering temperature. For the LF1 contribution, the values of capacitance, around 0.3 F cm^{-2}, are quite different from the values obtained for the LF phenomenon of the former case (electrode sintered at 950 °C); it means the phenomenon is not the same and could be adsorption of molecular oxygen at the electrode surface, dissociation of molecular oxygen or gas phase diffusion into the pore of the electrode, for the latter the activation energy should be near zero. [8,133,134]. It also proves that the attribution of the LF limiting step for the first cell (prepared at lower temperature) is not so clear as one expect a surface limiting step or a reactivity phenomenon to increase when the temperature is raised, and this seems not to be the case here. Finally, the Warburg element in the LF2 region possibly involves the process of transport of O^{2-} to the interface electrode/electrolyte, this process has been identified in the same temperature range (600-800 °C) and in the same LF region in $LaBaCo_2O_{5+\delta}$ [8], $GdBaCo_2O_{5+\delta}$ [9] and $LnBaCo_2O_{5+\delta}$ [14], additionally, large capacitances such as 5.76 F cm^{-2} at 800 °C in our case or 8 F cm^{-2} in $LaBaCo_2O_{5+\delta}$ are unlikely to be from any electrode process and are generally assigned to gas phase diffusion into the cathode [8] or as reported by Baqué [92] which presented similar processes with capacitances in the range of 0.16 – 8.5 F cm^{-2} for a Warburg element.

To conclude concerning the comparison between LBCuCo2 and LBCu, it is clear that the substitution of Co for Cu enhances the electrochemical properties of the electrode material, suppressing in particular the contribution at High Frequencies that was the main contribution to ASR in the case of LBCu.

3.6.3. LBCo. The impedance spectra for LBCo/BCZY/LBCo cells sintered at 950 and 1000 °C are shown in Figure 27.

Figure 27. Impedance spectra measured in air between 600 and 800 °C for LBCo cathodes sintered on BCZY at (a) 950 and (b) 1000 °C for 2h in air. The serial resistance (R_s) has been removed[10]

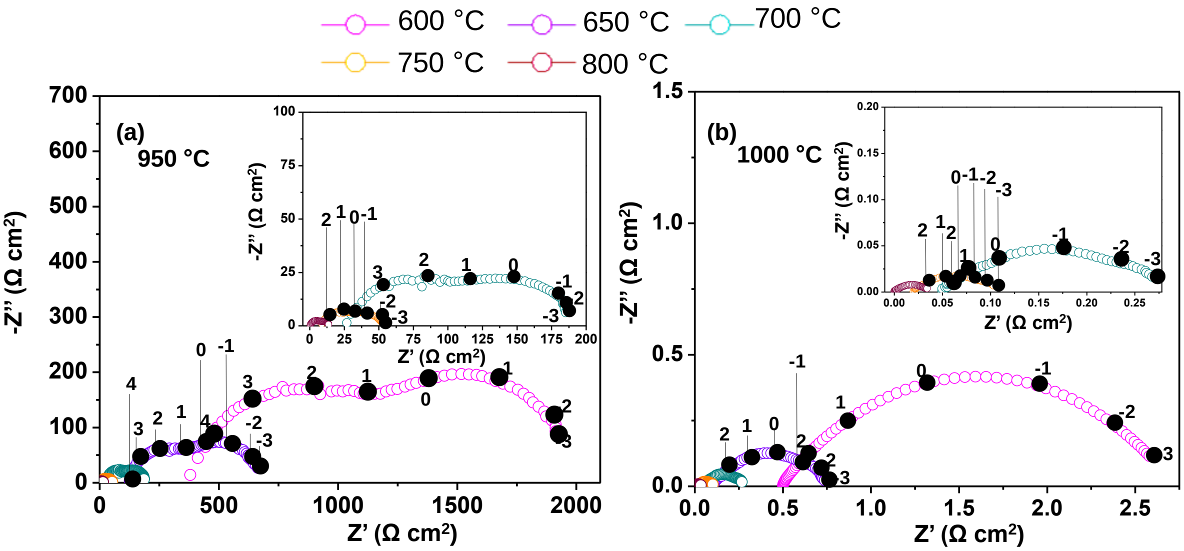

As in the case of LBCuCo2, the spectra plotted in Figure 27 are very different for each cell, *i.e.* the characteristic frequency range and the specific resistance values have changed, showing again the effect of the sintering temperature on the cathode properties. The modification while raising the sintering temperature is observed both for the High Frequency contribution, which completely disappear for the high temperature of sintering, and the Low Frequency phenomenon with a noticeable decrease of the corresponding resistance when the sintering temperature is raised.

Indeed, the EIS spectra obtained in the temperature range 600–800 °C, exhibit an asymmetric shape for the electrode sintered at 950 °C, which can be associated to more than one limiting step for the electrode process as shown in Figure 28(a). In the whole range studied, the impedance data were adjusted using an equivalent circuit composed of an inductance (L) in series with an ohmic contribution of the cell

---

[10] To be able to more easily compare the variation of R_p

(R_S) and two (R_i // CPE_i) elements consisting of a resistance (R_i) in parallel with a constant phase element (CPE_i), one at High Frequencies (HF) and another at Low Frequencies (LF). For the LBCo electrode sintered at 1000 °C, the impedance spectra obtained in the range 600–800 °C, exhibit a different shape, the impedance data were adjusted using an equivalent circuit composed of an inductance (L) in series with an ohmic contribution of the cell (R_S) and one (R_1 // CPE_1) element consisting of a resistance (R_1) in parallel with a constant phase element (CPE_1). Such simulation out in order to obtain the values of capacitance (C), characteristic frequency (f) and the area specific resistance (ASR) corresponding to each limiting step. ANNEX H and ANNEX I shows the simulated impedance spectra of the remaining temperatures of the electrodes sintered at 950 and 1000 °C, respectively.

Figure 28. Experimental and simulated impedance spectra for LBCo cathode sintered on BCZY and measured in air at 650 and 800 °C for cells prepared (a) at 950 °C and (b) at 1000 °C, respectively. The numbers correspond to the logarithm of frequency. The serial resistance (R_S) has been removed[11].

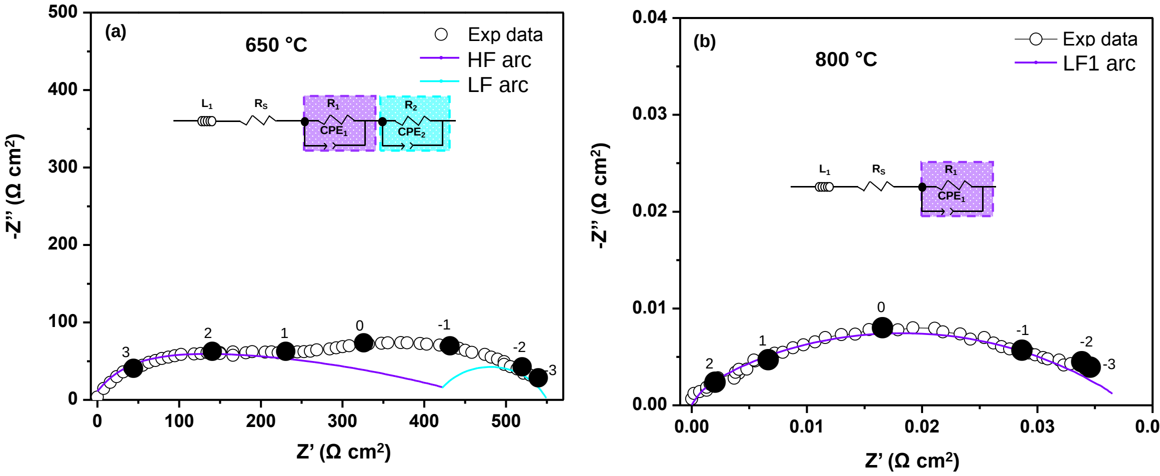

The fitted characteristics of all limiting steps are reported in Table 9 and Table 10 for sintering temperatures of 950 and 1000 °C, respectively. The effect of the increase of the sintering temperature on the electrode is reflected directly in the dramatic

---

[11] To be able to compare easily the variation of R_p

decrease of the ASR in the whole temperature range studied, *e.g.* values of 132.6 Ω cm^2 and 0.1249 Ω cm^2 are found at 700 °C for the sintering temperatures of 950 and 1000 °C, respectively, as seen in Figure 29.

Figure 29. Arrhenius plot of area specific resistance (ASR) for LBCo electrodes sintered at 950 and 1000 °C and measured in air.

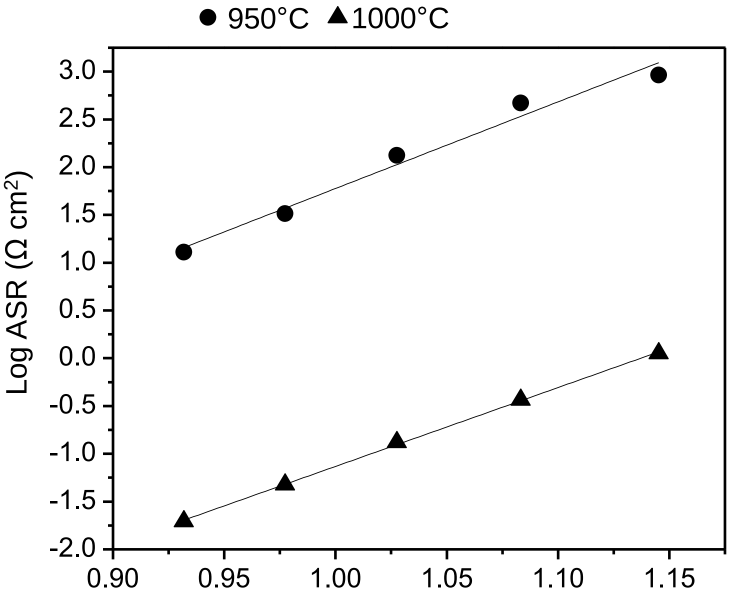

From the Arrhenius plot of the ASR as function of temperature represented in Figure 29, the LBCo electrode sintered at 950 °C exhibits very high ASR values, with quite high activation energy (E_a) of 1.4(8) eV; for the electrode sintered at 1000 °C, the E_a is of the order of 1.8(1) eV, which is quite higher compared to the disordered perovskite $La_{0.4}Ba_{0.6}CoO_3$ which value is 1.31 eV.

Figure 30. Arrhenius plot of the individual resistances for LBCo cathode sintered at (a) 950 and (b) 1000 °C and measured in air.

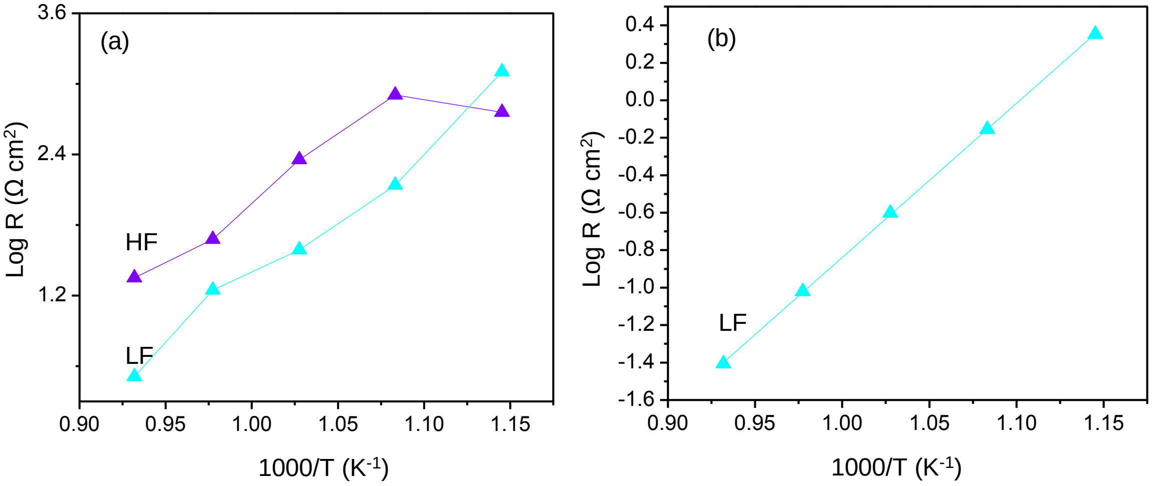

According to the results reported in Table 9 and Figure 30, for the electrode sintered at 950 °C, the first elementary step (HF) represents the main contribution with more than 70% to the R_p. As in LBCuCo2, this main contribution is associated to capacitance values varying in the range 10^{-7}-10^{-5} F cm^{-2} and is related to a charge transfer phenomenon, e.g. the electron transfer with ionic incorporation into the electrode [62,92]. Such limiting step disappears with increasing the sintering temperature, such improvement being explained by a probably better interphase and adhesion between the electrode and the electrolyte.

Concerning the LF arc present for the cell prepared at 950 °C and for which the corresponding capacitances range from 10^{-4} to 10^{-2} F cm^{-2}, a surface phenomenon that may be, typically, the dissociative adsorption of oxygen and/or surface diffusion of adsorbed oxygen species (Oad) is the first hypothesis, the formation of secondary phases at electrode/electrolyte interface being another possibility, as in the case of LBCuCo2.

On the other hand, Table 10, list the equivalent capacitances at 1000 °C in the order of ~0.3 – 5 F cm^{-2} in the whole temperature range for LF arc which can be refer to the limiting step of oxide ion diffusion in the pores as reported in $La_{0.5}Ba_{0.5}CoO_3$ [113,135], similar to $La_{1-x}Sr_xCoO_{3-\delta}$ [57] and as reported by Setevich et al. [90], for the $La_{1-x}Ba_xCoO_{3-\delta}$ system where capacitances varied from 1.1 to 7.7 F cm^{-2} in the temperature range of 450 – 700 °C.

Table 9. Quantitative parameters for LBCo electrode sintered at 950 °C measured in air.

T (**°C**)	**R_S** (**Ω cm^2**)	**HF**			**LF**			**Rp** (**Ω cm^2**)	**ASR** (**Ω cm^2**)	χ^2
		R_1 (**Ω cm^2**)	**C_1** (**F cm^{-2}**)	***f*** (**Hz**)	**R_2** (**Ω cm^2**)	**C_2** (**F cm^{-2}**)	***f*** (**Hz**)			
600	4500	572.7	3.08E-07	902.3	1266	2.74E-04	0.46	1838.7	919.4	3.1E-04
650	2648	803.3	3.68E-07	539.1	137.5	0.0043	0.27	940.8	470.4	7.5E-05
700	1619	226.4	1.64E-06	429.03	38.74	0.0118	0.35	265.14	132.6	4.4E-05
750	890	47.74	7.73E-06	431.03	17.67	0.0232	0.39	65.41	32.71	1.8E-05
800	520.6	22.45	1.13E-05	624.73	3.244	0.0932	0.53	25.694	12.85	1.3E-05

Table 10. Quantitative parameters for LBCo electrode sintered at 1000 °C measured in air.

T	RS	LF			Rp	ASR	χ^2
		R	C	f			
600	20.55	2.25	0.34	0.198	2.25	1.125	1.2E-05
650	14.36	0.6999	0.78	0.29	0.6999	0.35	1.2E-05
700	10.16	0.2499	1.17	0.54	0.2499	0.1249	5.6E-06
750	7.269	0.0953	2.92	0.57	0.0953	0.0476	5.7E-06
800	5.348	0.0392	5.64	0.72	0.0392	0.0196	4.2E-06

Although those measurements are preliminary results, it seems quite clear that the low sintering temperature (T_s=950 °C) does not favor the electrochemical performance of LBCuCo2 and LBCo electrodes; in particular for the pure cobaltite, a sintering temperature of 1000 °C leads to much better performance, although probably promoting the grain growth. Kim *et al.* [13] also discussed that at higher temperatures of preparation there is an improved performance of the cell than those attached at lower sintering temperatures, additionally, reported that no Cu-free samples in $LnBaCo_{2-x}Cu_xO_{5+\delta}$ system improved cathode performances; however, a high Cu content can lead to a decrease in performances, something to have account in this work respect LBCuCo2, which is high in copper content and similar ordered vacancies as the structures mentioned above.

Figure 31. Arrhenius plot of the Rp (polarization resistance) for LBCo, LBCuCo2 and LBCu cathodes measured in air.

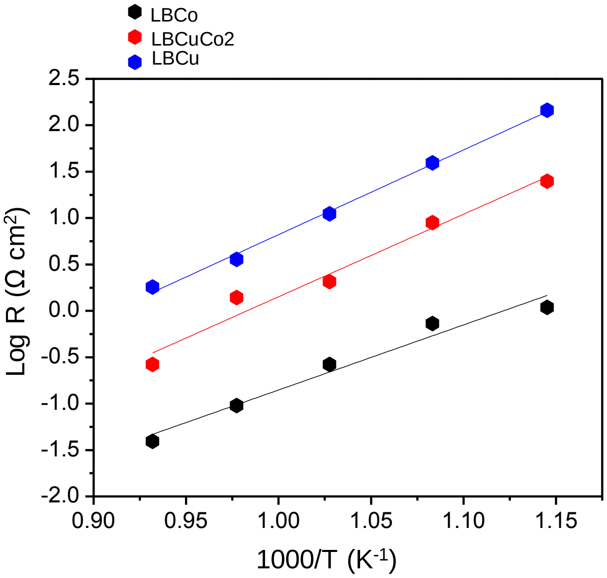

In Figure 31, the best R_p values obtained for LBCo and LBCuCo2 are finally compared with LBCu performance, with similar activation energy values of 1.56(7), 1.65(3) and 1.72(8) eV, respectively. Their R_p at 600 and 800 °C are shown in Table 11. For instance, the R_p values of LBCo are in a better agreement with its homologues such as $La_{0.5}Ba_{0.5}CoO_3$ which R_p is 0.02 at 800 °C which is not that far from the 0.039 Ω cm^2 of LBCo, considering that $La_{0.5}Ba_{0.5}CoO_3$ was sintered at 1050 °C.

Table 11. R_p (polarization resistance) for LBCu, LBCuCo2 and LBCo cathodes measured in air.

	LBCu (950 °C)	**LBCuCo2 (1000 °C)**	**LBCo (1000 °C)**
T (°C)	**R_p Ω cm^2**		
600	145.5	25.01	2.25
650	39.26	8.932	0.7312
700	11.14	2.067	0.2641
750	3.59	1.388	0.0953
800	1.808	0.264	0.0392

Those preliminary results seem to show that cobaltites of the disordered form have better electrochemical behavior than ordered ones, even if the comparison is not so easy as the composition of LBCuCo2 and LBCo is not the same. Additionally, a similar conclusion has been given recently by Garcés *et al.* [136], who reported that disordered perovskite perform better than ordered structures, in this case the phases of study were the ordered $LaBaCo_2O_{6-\delta}$ and disordered $La_{0.5}Ba_{0.5}CoO_{3-\delta}$, the latter presenting lower R_p values with an overall activation energy of 0.42 eV, therefore, the best system would be an hypothetical phase with cationic disorder, but with microstructure optimized by a “soft” chemical method.

4. RESULTS AND DISCUSSION – THE $La_4BaCu_{5-x}Mn_xO_{13\pm\delta}$ SERIES

As we could observed in the first part, the cuprate $La_4BaCu_5O_{13+\delta}$ (and substituted compositions with Co) already presents good cathodic properties. Nevertheless, this structure is not stable in reducing atmosphere (as seen in section 3.2); so, the present work concerns the synthesis and preliminary evaluation of Mn substitution in $La_4BaCu_5O_{13+\delta}$, with the aim to ensure the stability of the material in anodic conditions based on the fact that Sr-based $(La_xSr_{1-x})_5Mn_5O_{13}$ compounds present an identical structure to LBCu [17]. A second goal of our study is to compare in the future the anodic and cathode behavior of materials with ordered and disordered (cubic-like perovskite) structure, respectively within the $La_4BaCu_{5-x}Mn_xO_{13\pm\delta}$ series, if they exist.

4.1. STRUCTURAL ANALYSIS BY X-RAY DIFFRACTION (XRD)

Following the success of the sol-gel method employed in the $La_4BaCu_{5-x}Co_xO_{13\pm\delta}$ series, we prepared the $La_4BaCu_{5-x}Mn_xO_{13\pm\delta}$ by the same technique. Figure 32 shows the XRD patterns of the as-synthesized powders after a heat treatment at 950 °C for 5 hours. From those results, we can conclude that single phase $La_4BaCu_4MnO_{13\pm\delta}$ (x= 1) and $La_4BaCu_3Mn_2O_{13\pm\delta}$ (x= 2) can be obtained after a heat treatment at 950 °C. For x=3, 4 and 5, a very small amount of impurity was detected at $2\theta=31.4°$ in the same conditions. The latter can be due to a problem of synthesis conditions, since in oxidizing medium at 950 °C the two valences of Mn possess are Mn^{3+} and Mn^{4+}, the latter being the most probable as for example in $BaMnO_3$ impurity, which is formed in parallel to the main phase (Table 12).

Figure 32. XRD patterns of the as-synthesized series after 950 C/5h in air.

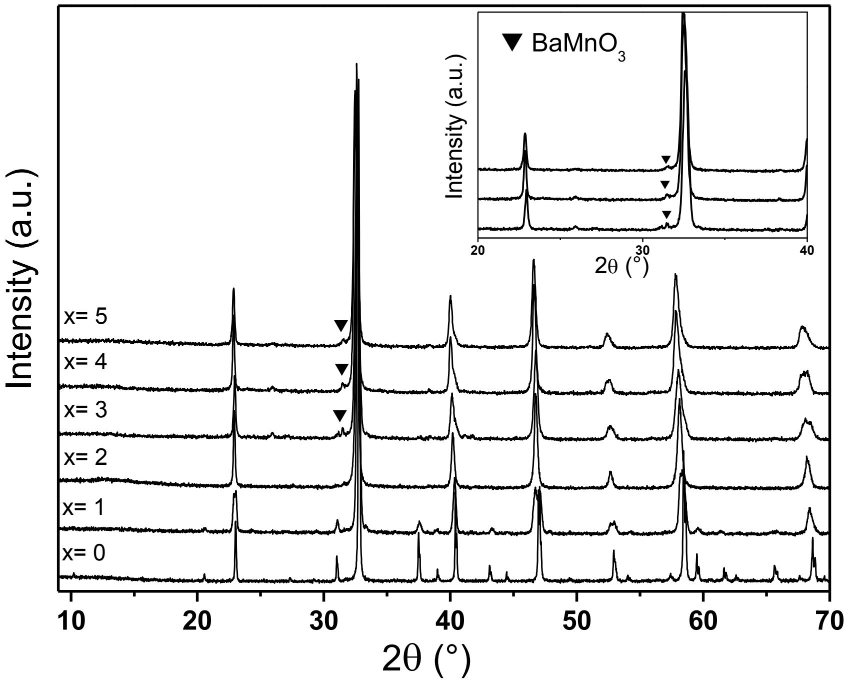

As a consequence, the x= 3, 4 and 5 compositions were subjected to another heat treatment at 1000 °C for 5 hours, obtaining successfully single phases (Figure 33). Rietveld refinement was performed for both samples series, *i.e.* in both cases of synthesis conditions and the respective results are given in Annexes J and K and in Table 12. No major difference is observed in the case of x=0 and 1, but dramatic differences are found for the other compositions, discarding the use of impure phases in the rest of the study. The subsequent tests were carried out with only single phases, that is, single phases sintered either at 950 or 1000 °C (Table 13).

Table 12. Structural parameters of $La_4BaCu_{5-x}Mn_xO_{13\pm\delta}$ after synthesis in air at 950 °C/5h, calculated by Rietveld refinement using XRD data.

x	**Space group**	**a=b (Å)**	**c (Å)**	**V (Å^3)**	**R_p**	**R_{wp}**	**χ^2**
0	P4/m	8,647(1)	3,8600(4)	288,67(4)	5,11	6,6	1,31
1	P4/m	8,642(2)	3,892(1)	290,74(14)	5,54	7,05	1,75
2	P4/m	8.619(4)	3.887(5)	288.8(4)	5,38	6,1	1,65
3	R-3c	5,520(1)	13,404(1)	353,79(33)	4,7	6,53	1,54
	P63/mmc	5,700(3)	4,822(7)	135,88(23)			
4	R-3c	5,530(1)	13,433(5)	355,78(18)	4,95	6,4	1,48
	P63/mmc	5,692(7)	4,806(8)	134,87(33)			
5	R-3c	5,542(1)	13,463(4)	358,17(17)	4,93	6,34	1,31
	P63/mmc	5,704(4)	4,813(12)	135,652(37)			

Figure 33. XRD patterns of the as-synthesized series after 1000 °C/5h in air.

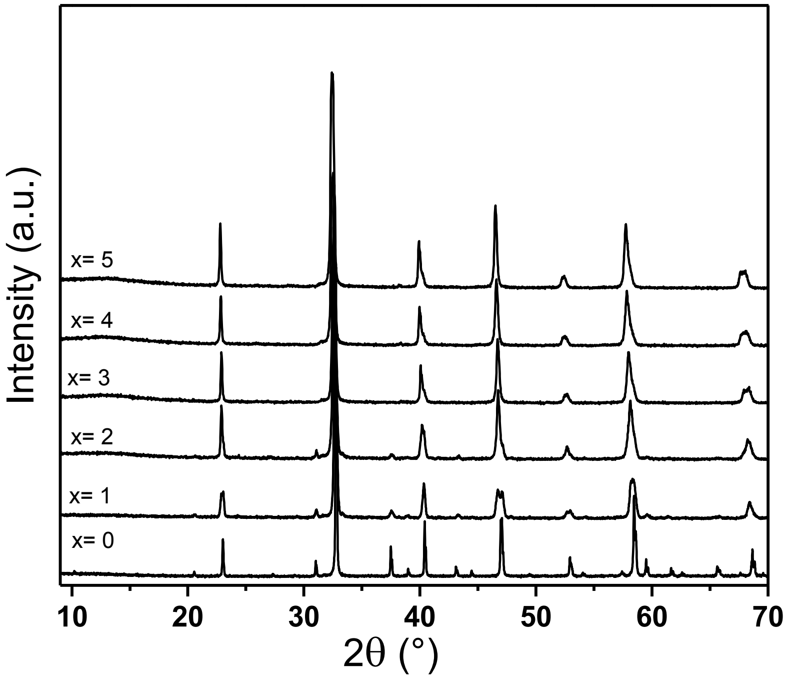

The $La_4BaCu_{5-x}Mn_xO_{13\pm\delta}$ series exhibit a different structural behavior from the homologue Cu/Co compounds (described in section 3.1). For x= 1, the material presents the ordered tetragonal structure similar to x=0 composition (space group *P*4/*m*), recently reported by Macías *et al.* [74]. In contrast to the Cu/Co series, a disordered perovskite is already present for x= 2 and, finally, from the composition x= 3 to x=5, a pure disordered rhombohedral perovskite with space group $R\bar{3}c$ is formed, similarly to the materials described by Dhama *et al.* [137] and Trukhanov *et al.* [138], who reported that compounds rich in Lanthanum in the $La_{1-x}Ba_xMnO_{3\pm\delta}$ series possess a disordered perovskite structure with a rhombohedral space group ($R\bar{3}c$). For the XRD patterns that correspond to x≥ 3 in Figure 32, the hexagonal perovskite with space group $P6_3/mmc$ corresponding to the $BaMnO_3$ impurity (a = b = 5.7041 Å and c = 4.8128 Å) was also considered for the Rietveld refinements (Table 12) [139].

Table 13. Structural parameters of $La_4BaCu_{5-x}Mn_xO_{13\pm\delta}$ after synthesis in air at 1000 °C, calculated by Rietveld refinement using XRD data

x	**Crystal system**	**Space group**	**a = b (Å)**	**c (Å)**	**V (Å^3)**	**R_p**	**R_{wp}**	**χ^2**
0	Tetragonal	P4/m	8.6478(2)	3.8605(2)	288.70(1)	4.53	5.97	1.96
1	Tetragonal	P4/m	8.641(2)	3.892(1)	290.6(1)	5.48	6.93	1.65
2	Tetragonal	P4/m	8.619(4)	3.887(5)	288.8(4)	4.88	6.24	1.69
	Rhombohedral	$R\bar{3}c$	5.503(1)	13.408(5)	351.7(2)			
3	Rhombohedral	$R\bar{3}c$	5.5172(9)	13.414(3)	353.6(1)	4.89	6.35	1.41
4	Rhombohedral	$R\bar{3}c$	5.528(1)	13.435(4)	355.6(1)	4.99	6.51	1.47
5	Rhombohedral	$R\bar{3}c$	5.5382(9)	13.464(3)	357.6(1)	4.62	6.07	1.36

Figure 34 shows the evolution of the cell parameters as a function of Mn content (x). Discarding the compositions for which a phase mixture is formed, we can observe that for the ordered phases (x<2) the *a*-parameter remains nearly constant with x (considering the standard deviation) when *c*-parameter (*i.e.* the cell volume) increases.

Figure 34. Evolution of (a) *a*-parameters (b) *c*-parameters and (c) volume against Mn composition in $La_4BaCu_{5-x}Mn_xO_{13\pm\delta}$ (a_R and c_R correspond to de Rhombohedral perovskite parameters).

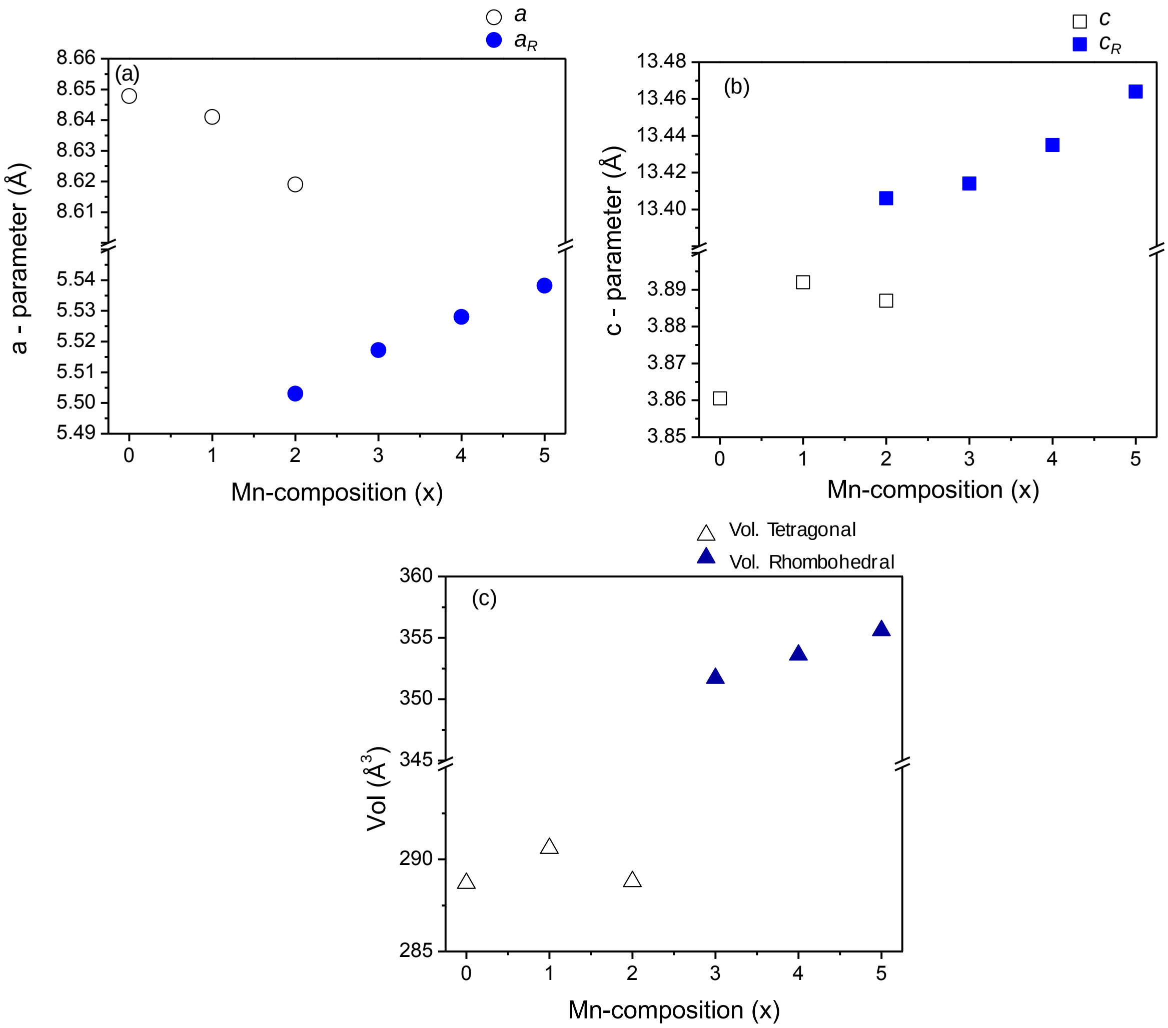

For x>2, *i.e.* when the solid solution presents a disordered perovskite phase, we can observe that both *a* and *c* parameters increase with x. In a first approximation, and even if such kind of evolution is sometimes complex in anisotropic structures, such behavior can be explained according to the change of cation size, where $R^{VI}_{Mn^{3+}}$=0.645 Å [115] and $R^{VI}_{Mn^{2+}}$=0.83 Å are bigger than $R^{VI}_{Cu^{3+}}$=0.54 Å [115] or for instance $R^{VI}_{Cu^{2+}}$=0.73 Å [115] is larger than $R^{VI}_{Mn^{4+}}$=0.53 Å [115].

4.2. THERMAL STABILITY IN REDUCING ATMOSPHERE

In this family, the stability test in reducing atmosphere was evaluated by thermal treatment in 3% H_2/N_2 at 850 °C during 6 hours and carried out for all the compositions (x= 1, 2, 3, 4, 5) in order to determine at what Mn-concentration the material starts to show stability, in other words, the viability of the material as an anode for SOFC or IT-SOFC.

Figure 35. XRD patterns of $La_4BaCu_4MnO_{13\pm\delta}$ (x= 1) before and after reduction at 850 °C.

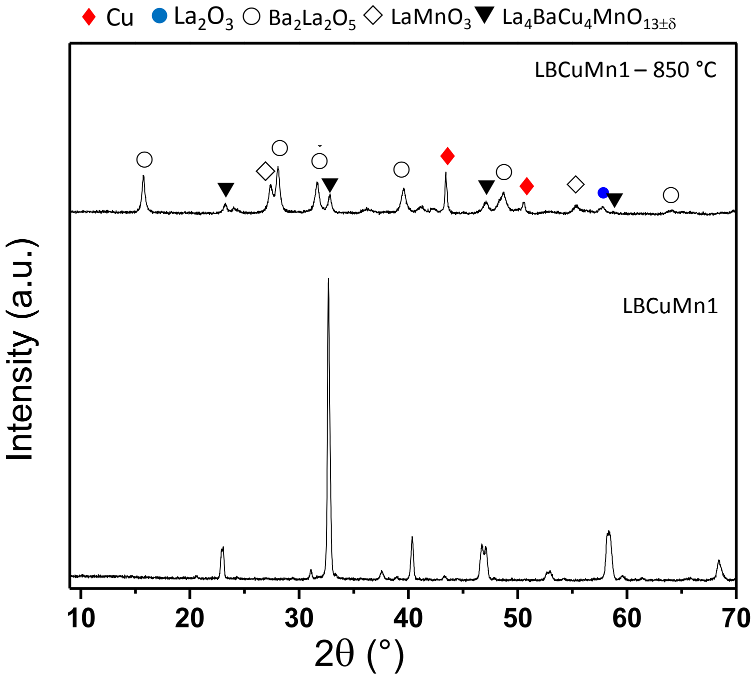

The compounds in the $La_4BaCu_{5-x}Mn_xO_{13\pm\delta}$ series exhibit different behaviors in reducing atmosphere. In the range $0 \leq x \leq 2$, it is possible to easily identify that a decomposition occurs, as observed in Figure 35 for $La_4BaCu_4MnO_{13\pm\delta}$ (x= 1), identifying the presence of Copper in its metallic form, Lanthanum oxide (La_2O_3) (material precursors) and Lanthanum-Barium Oxide ($La_2Ba_2O_5$), as well as other phases in lower proportion that may have formed during reduction. Other figures corresponding to other compositions are presented in Annex L.

Figure 36. XRD patterns of $La_4BaCu_2Mn_3O_{13\pm\delta}$ (x= 3) before and after reduction at 850°C

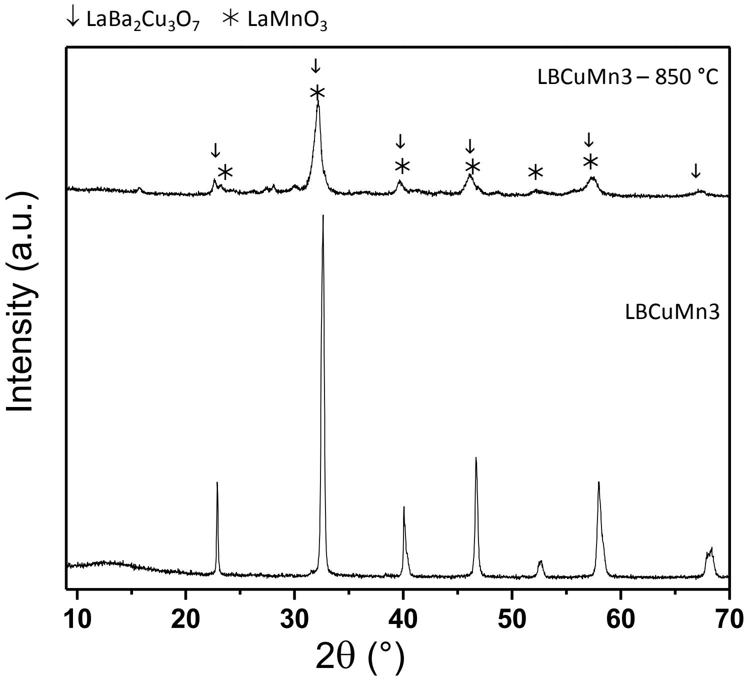

In Figure 36, the XRD patterns of $La_4BaCu_2Mn_3O_{13\pm\delta}$ (x= 3) before and after reduction treatment show that such composition seems to maintain its characteristic peaks; however, these are wider showing that the material structure begin to destroy during the reduction process. The presence of metallic copper is not very clear but the background being not completely straight in the region of Cu diffraction peaks, it is possible to think that Cu and/or other phases are also present in small amount in the material; As a first conclusion, the manganese seems to give the material a certain degree of stability in reducing conditions; but not enough to cancel the instability due to Cu in this phase.

Figure 37. XRD patterns of $La_4BaCuMn_4O_{13\pm\delta}$ (x= 4) before and after reduction at 850°C

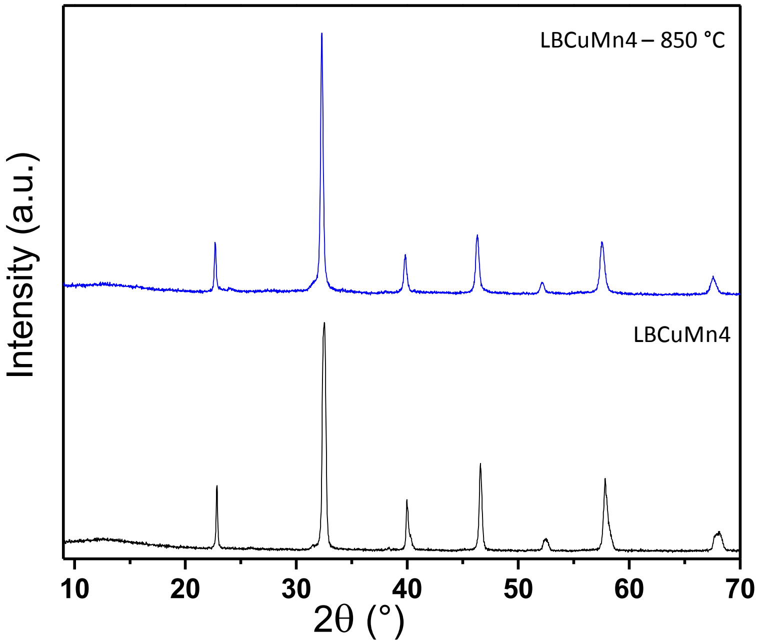

On the other hand, for $La_4BaCuMn_4O_{13\pm\delta}$ (x= 4), the XRD patterns before and after reduction are shown in Figure 37; they are very similar, showing that the material remains stable after reduction as no extra peaks corresponding to impurities are present. A Rietveld refinement was carried out successfully using the rhombohedral space group $R\bar{3}c$, like the as-synthesized sample in air (Table 14).

Table 14. Structural parameters of $La_4BaCuMn_4O_{13\pm\delta}$ (x= 4) before and after the test in 3% H_2/N_2, calculated by Rietveld refinement using XRD data.

	Before treatment	**After treatment**
		850 °C
	LBCuMn4	LBCuMn4-H2
a (Å)	5.528(1)	5.543(5)
c (Å)	13.435(4)	13.59(2)
V (Å^3)	355.6(1)	361.8(7)
R_p	4.99	5.21
R_{wp}	6.51	6.7
χ^2	1.47	1.75

The graphical result of the Rietveld refinement is shown in Figure 38. We can conclude that in the middle of these two Mn-concentrations (x = 3 and 4) can be found the stability limit within the $La_4BaCu_{5-x}Mn_xO_{13\pm\delta}$ series. Finally, x= 5 shows the same behavior as for x=4, *i.e.* the diffractograms conserve the same characteristic peaks of the as-prepared phase (see Annex M). This behavior confirms the ability of the x=4 and 5 materials to be used as possible anode material, in addition to cathode, *i.e.* as an electrode in a symmetric fuel cell.

Figure 38. Graphical result of Rietveld refinement of x=4 after reduction in 3% H_2/N_2 at 850 °C for 6 h.

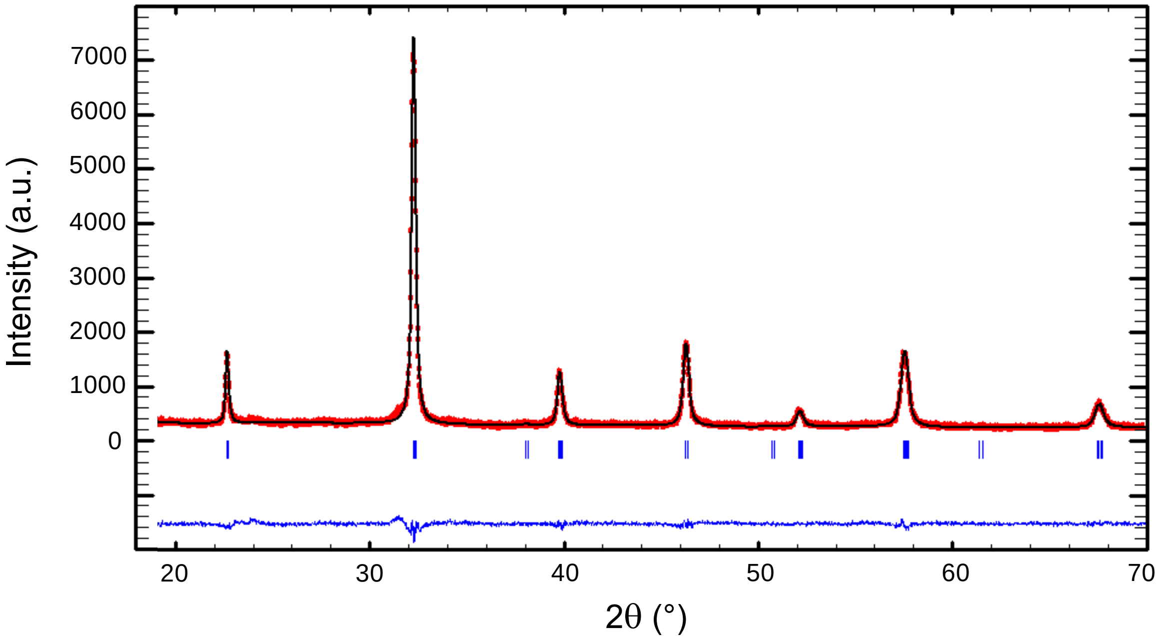

The results for x≥3 are a consequence of the replacement of Cu by Mn within the structure, the latter, taking in oxidizing conditions a Mn^{3+}/Mn^{4+} mixed valence and in reducing conditions Mn^{2+}/Mn^{3+} oxidation states similar to Cu in the air-synthesized phase, which is approximately +2.44, the latter in order to ensure the stability of the structure [74]. In other words, the valence of Mn cations remain in all atmospheres close to that of Cu in the as-prepare LBCu, *i.e.* Mn gives the structure a greater degree of global oxidation than Cu that don't support H_2 atmosphere without being reduced to metallic state. Therefore, when the sample LBCu (x= 0) is subjected to the reducing test, it is destroyed because of the total Cu reduction, obtaining metallic copper inside the structure; on the contrary, for the samples with x≥ 3, although manganese may be reduced, it will not reach valences lower than Mn^{2+}, so that the sample remains stable.

To try to understand such behavior, thermogravimetrical analyses (TGA) in diluted H_2 have been performed for x=4 and 5 from RT to 1000 °C; additionally, TG study was also carried out in air for x=5.

Figure 39. Thermogravimetric analysis (TGA) in 3% H_2/Ar of $La_4BaCu_{5-x}Mn_xO_{13\pm\delta}$ (x= 4 and 5).

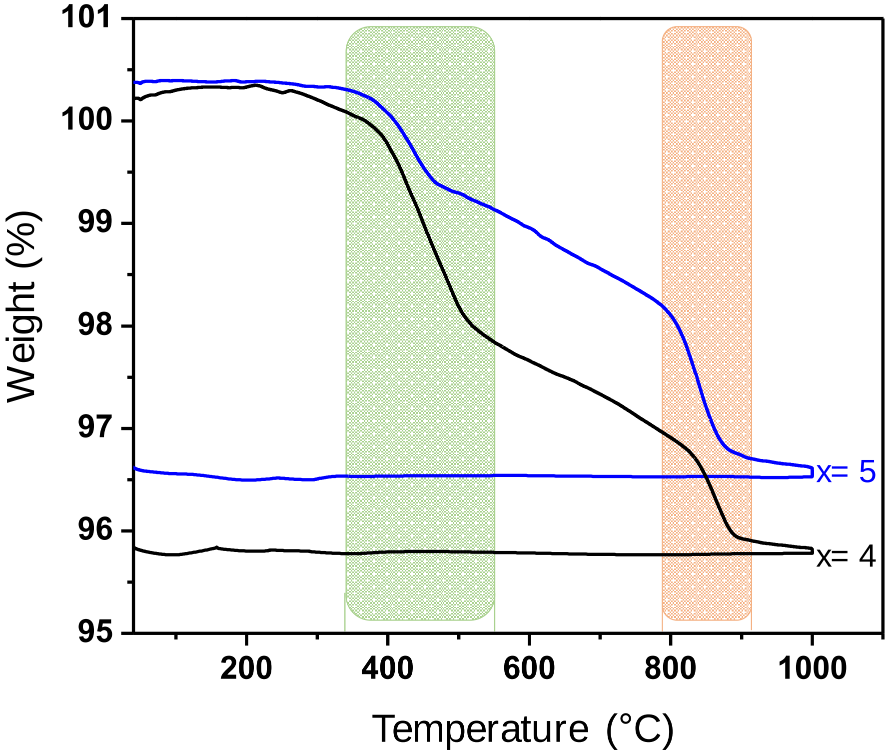

As shown in Figure 39, the TGA profiles in diluted hydrogen are similar; however, for x= 4 the weight loss is sharper than that of x= 5. A first weight loss is distinguished between 350 and ~552 °C, being much smaller for x= 5 around 0.67% (T ~ 485 °C) compared to the 2.04% of x= 4 (T ~ 528 °C). In both cases, the first weight loss tends to be associated to the creation of oxygen vacancies (δ), followed by a second weight loss in the temperature range 790–900 °C, with a 3.26 % and 4.06% for x=5 and 4, respectively. Tentatively, the first weight loss can be associated to the reduction of $Mn^{4+} \rightarrow Mn^{3+}$ or $Mn^{3+} \rightarrow Mn^{2+}$, and the second loss to a reduction of $Mn^{3+} \rightarrow Mn^{2+}$ if the first one is $Mn^{4+} \rightarrow Mn^{3+}$ or $Mn^{3+} \rightarrow Mn^{2+}$ that follows the first reduction $Mn^{3+} \rightarrow Mn^{2+}$ assuming no destruction of the material crystal structure, based on the stability result in H_2 mentioned before (850 °C), however, based on the results of Figure 39 it is probably that the second weight loss may correspond to the start of decomposition of the material at T> 750 °C, this can be due to the fact that the oven where the stability test in H_2 was performed may have a problem at heating and the test may have been carried out at ~750-800 °C. Moreover, from the above TG profile we determined the oxygen content of both x= 4 and 5; for the Cu/Mn structure (LBCuMn4) an oxygen content of $13+\delta=13.006$ was found at Room Temperature, however, since the material presents both Cu and Mn valences makes it difficult to determine the real valence of Cu and Mn present in the system, but is possible to assume that at T>750 °C the structure presents Cu in its metallic form, therefore, at T<750 °C Cu can't assume a valence of 0. As for high Co content, the LBMn (x= 5) sample can be rewritten as $La_{1-x}Ba_xMnO_{3-\delta}$ perovskite which homologous in the literature would be $La_{0.8}Ba_{0.2}MnO_{3-\delta}$ and oxygen content would be presented as $3-\delta$. From Figure 39, we determined an oxygen content of $3-\delta=2.88$ at Room Temperature (RT) suggesting $Mn^{2.96+}$ in $La_{0.8}Ba_{0.2}MnO_{2.88}$, transforming into $Mn^{2.9+}$ at 485 °C; during the second weight loss before it start to decompose (750 °C), we found $La_{0.8}Ba_{0.2}MnO_{2.83}$ stoichiometry with $Mn^{2.82+}$ oxidation state. Such behavior agrees with the assumption mentioned above, starting with an Mn valence ~3+ transforming into a ~2.8+ oxidation state, this behavior explains the stability of the manganites in reducing conditions and possibly as MIEC materials due to the oxygen non-stoichiometry in both air or H_2 conditions.

To complete those results, TG curve of x=5 composition was also measured in air (two cycles) and is given in Figure 40. During the first heating cycle, a continuous weight loss can be distinguished from RT to 800 °C, commonly associated to desorption of undesirable species *e.g.* H_2O or CO_2 in the form of hydroxide or carbonate species. Considered as surface contamination of the sample, these losses are not reproduced during the second heating/cooling cycle in air up to 800 °C and no significant change is indeed evidenced during this second cycle, *i.e.* no major loss of oxygen from the crystal lattice (~0.084%), emphasizing the stability of the material at high temperature in air and its nearly constant stoichiometry.

Figure 40. Thermogravimetric profile for LBMn in air.

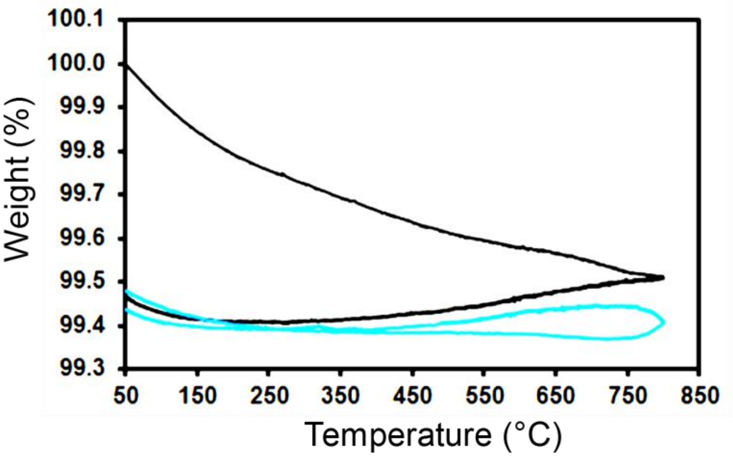

Finally, the structural behavior of LBMn sample from an oxidizing to a reducing atmosphere was examined by High Temperature X-Ray Diffraction (HT-DRX), following a sequence of three continuous cycles of heating/cooling in air, follow by diluted hydrogen and, finally, reoxidation (air) as presented in Figure 41, where at 475 °C a change in structure is observed in all atmospheres with a transition from rhombohedral to cubic space group $Pm\bar{3}m$, and the progression from RT to 800 °C in both heating/cooling cycles.

Figure 41. HT-XRD patterns of as-synthetized $La_4BaMn_5O_{13}$ from Room Temperature to 800 C in air, $3\%H_2/Ar$ and reoxidation (air).

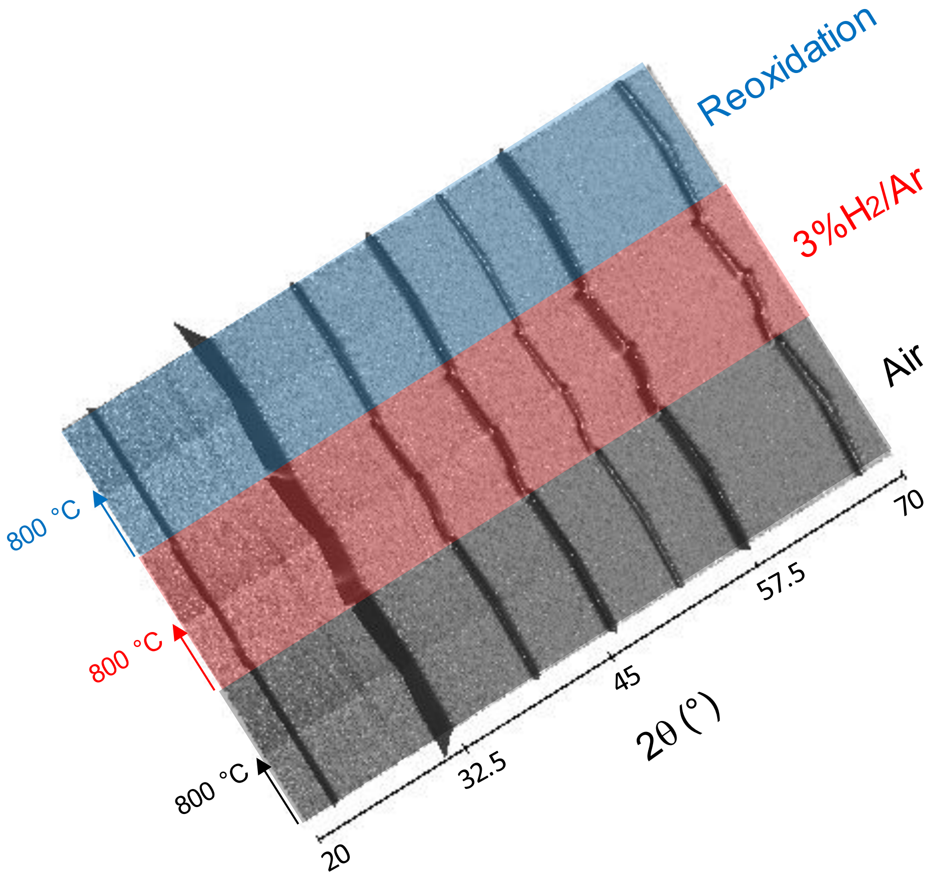

The evolution of LBMn cell parameters during the 3 cycles is presented in Figure 42. For comparison, the cell parameters were normalized with respect to the perovskite pristine cell, in which $a_p = a/\sqrt{2}$ and $c_p = c/2\sqrt{3}$ where *a* and *c* are the parameters of the rhombohedral cell. The thermal behavior during the first heating cycle in HT-XRD (black circles) agrees with the absence of accident in the TG curve in air (Figure 42), *i.e.* a pure dilatation process is found along *a* and *c* parameters, that leads to a global dilation of the material, quite classical for a ceramic. During heating in reducing atmosphere, both *a* and *c* parameters increase dramatically in the temperature range 350-500 °C (red circles in Figure 42), that corresponds nearly perfectly to the first material reduction observed by TGA (Figure 39). As a consequence, an increment of 2 units is observed in the cell volume, passing from 60.4 Å^3 in air to 62.5 Å^3 in diluted hydrogen at 800 °C. After 500 °C, an almost linear evolution of all parameters is observed, that nearly corresponds to the same points during cooling, *i.e.* normal thermal expansion of the material, except the small accident around 475 °C, where the transition from rhombohedral to cubic phase takes place. The cell volume increase during reduction is clearly associated to the change of oxidation state of Mn discussed above ($R^{VI}_{Mn^{3+}}$=0.645 Å [115] to $R^{VI}_{Mn^{2+}}$=0.83 Å [115]). This type of behavior has been reported for the ordered manganite $NdBaMn_2O_{5+\delta}$ [140] and to the Ruddlesden-Popper *i.e.* $La_{0.5}Sr_{1.5}MnO_4$ [141]. The last cycle in air is the material reoxidation and it demonstrates that the redox behavior of LBMn is reversible, since the cell parameters values after the second heating in air returns to the same values of the first heating cycle in air. Another interesting feature of the LBMn material study is the small variation of the parameters which is reflected in the change of cell volume around 1.3%, which is small in comparison to the anode of the state of the art (Ni/YSZ) which is ~50-60% during redox cycles [142,143].

Based on these results, the Thermal Expansion Coefficient (TEC) were deduced from data analysis during cooling in air and hydrogen (black/blue and red open circles in Figure 42), since the compatibility between electrode/electrolyte concerns the thermomechanical behavior. The TEC values have been obtained considering the same formula as for the Co series: TEC = 1/3 $(2\alpha_a + \alpha_c)$ as it is valid in the case of axial rhombohedral symmetries [101]; the obtained values are presented in Table 15.

Figure 42. Evolution of the red parameters and volume cell during redox cycling for LBMn

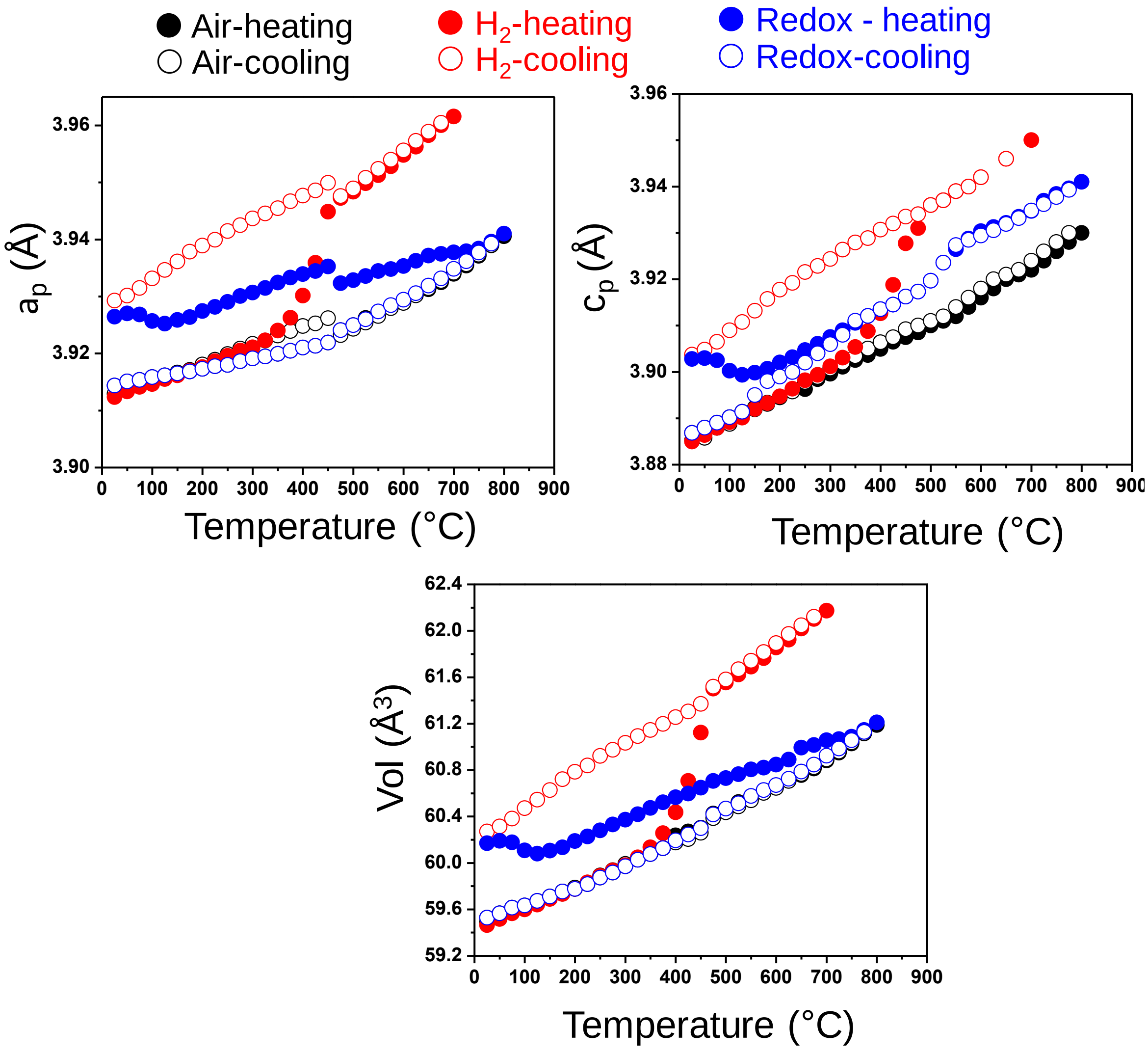

Table 15. Thermal expansion coefficients of LBMn in oxidizing and reducing atmosphere

	TEC × 10^{-6} K^{-1}	
Crystal structure	**Air**	**3% H_2/Ar**
Rhombohedral (25 - 450°C)	10.1(2)	14.2(3)
Cubic (475 – 700 °C)	13.4(2)	16.1(3)

Compared to other perovskite-like manganites, the TEC values of LBMn in air are close to, for example, $Sm_{0.5}Sr_{0.5}MnO_3$ with TEC of 10.7×10^{-6} K^{-1} or $Sm_{0.6}Sr_{0.4}MnO_3$ with 10.4×10^{-6} K^{-1} in the range 20 – 800 °C [120] and not very far from the state of art cathode $La_{0.8}Sr_{0.2}MnO_3$ with TEC=11.4×10^{-6} K^{-1} [144]. Also, a similar behavior of phase transition has been evidenced for the $La_{0.7}Sr_{0.3}MnO_3$ perovskite with a TEC value of 12.23×10^{-6} K^{-1} and 13.23×10^{-6} K^{-1} between 197-650 °C and 650 897 °C [145], respectively, presenting very close values to the LBMn cubic phase. On the other hand, the TEC values in diluted hydrogen are slightly higher than for the Ruddlesden-Popper $La_xSr_{2-x}MnO_{4\pm\delta}$ series which are around 13.7×10^{-6} K^{-1} [141], but in agreement with $NdBaMn_2O_{5+\delta}$ which average thermal expansion coefficient under hydrogen is 15×10^{-6} K^{-1} [140,146]. Globally, and opposite to the case of LBCuCo2 and LBCo, all those values are relatively closer to typical TEC values for the conventional electrolyte materials, *i.e.* YSZ (10-11 × 10^{-6} K^{-1}), GDC (12-13 × 10^{-6} K^{-1}) and LSGM (11-12 × 10^{-6} K^{-1}) [102–104], a good point for the LBMn composition.

4.3. CHEMICAL COMPATIBILITY ELECTROLYTE AND ELECTRODE MATERIALS

As performed in section 3.4, $La_4BaMn_5O_{13}$ single phase was put in contact with BCZY electrolyte in order to test the possible chemical reactivity between electrode and electrolyte at 1000 °C/6h.

As observed in Figure 43, the XRD patterns of the LBMn/BCZY mixture before and after the heat treatment in air show that both materials remain unchanged as neither additional peaks nor major modification of XRD pattern are observed (see Annex N). Into details, structure refinements using the XRD data show a minimum variation of the lattice parameters and cell volume before and after calcination, as shown in Table 16, confirming the good chemical compatibility of these compounds at high temperature.

Figure 43. XRD patterns before and after reactivity test in air of $La_4BaMn_5O_{13\pm\delta}$ (x= 5) at 1000 °C.

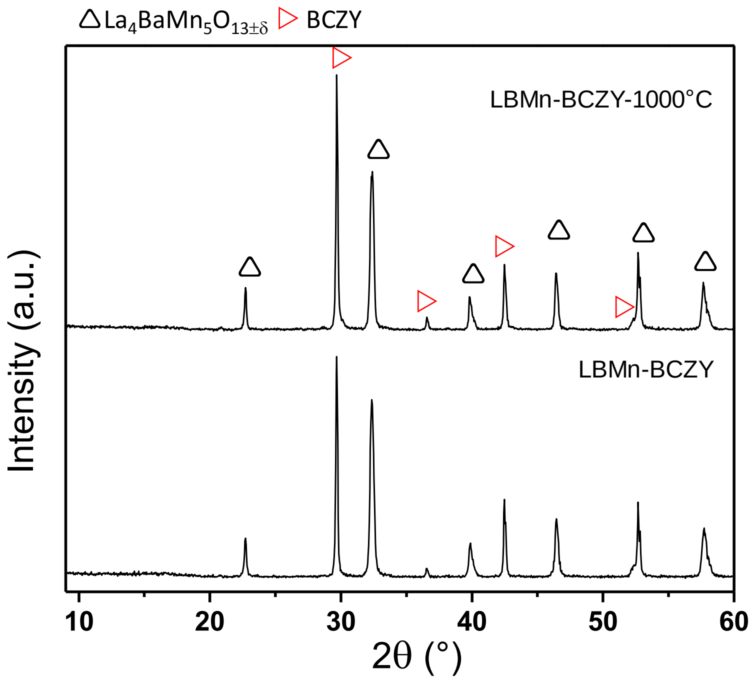

Table 16. Structural parameters of $La_4BaMn_5O_{13\pm\delta}$ (x= 5) before and after the reactivity test, calculated by Rietveld refinement using XRD data.

	Before treatment		**After treatment**	
			1000 °C	
	LBMn	BCZY	LBMn	BCZY
***a* (Å)**	5.5382(9)	4.250(2)	5.539(5)	4.252(2)
***c* (Å)**	13.464(3)	4.250(2)	13.58(1)	4.252(2)
V (Å^3)	357.6(1)	76.79(6)	358.5(5)	76.92(7)
R_p	11.30		12.6	
R_{wp}	16.80		19	
χ^2	1.70		2.13	

The increase of LBMn cell volume after heating can be due to the substitution of some large Ce^{4+}, Zr^{4+} o Y^{3+} ($R^{IX}_{Ce^{4+}}$=1.02 Å, $R^{IX}_{Zr^{4+}}$=0.89 Å, $R^{VI}_{Y^{3+}}$=1.075 Å [115]) cations at the position of smaller Mn^{3+} or Mn^{4+} cations ($R^{VI}_{Mn^{3+}}$=0.58 Å,

$R^{VI}_{Mn^{2+}}$=0.83 Å [115]). On the other hand, the increment on BCZY can be due to substitution of a larger cations such as La^{3+} ($R^{IX}_{La^{3+}}$=1.216 Å [115]) in the structure, Ba is no consider in the interdifussion since both structures have it . Even though the slight change can be due to the cationic interdiffusion between LBMn/BCZY, is difficult to explain without a complementary technique as mentioned before for the Co compositions.

4.4. CONDUCTIVITY MEASUREMENTS

For the composition of interest, LBMn (x= 5), the conductivity test was carried out in oxidizing and reducing atmosphere. The Arrhenius plot of the electrical conductivity as a function of temperature measured in diluted hydrogen and air is presented in Figure 44, which shows a thermally activated type temperature dependence in both conditions.

Figure 44. Arrhenius plot of the total conductivity of $La_4BaMn_5O_{13\pm\delta}$ (x= 5) in air and 3% H_2/Ar

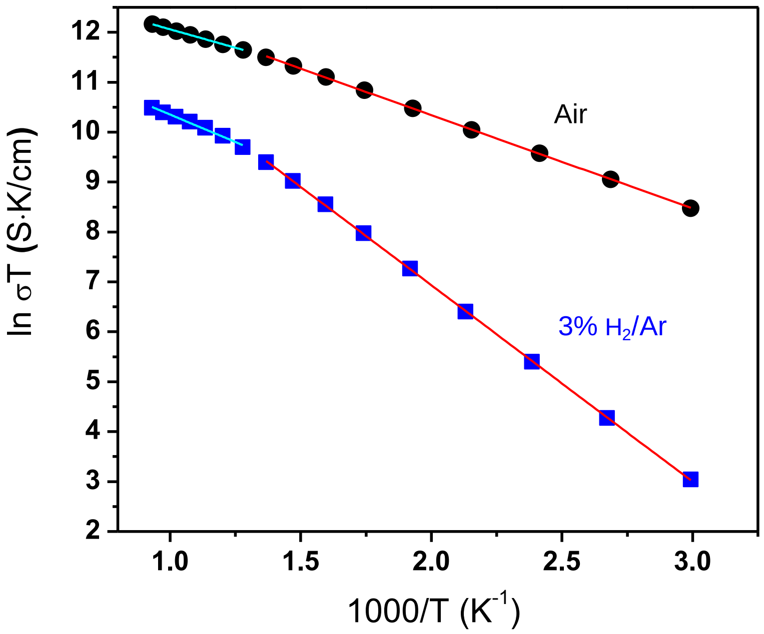

LBMn conductivity varies from 14 S cm^{-1} to 178 S cm^{-1} in air and from 0.06 S cm^{-1} to 33 S cm^{-1} in diluted hydrogen in the range 60–800 °C, meeting the requirements to that of electrode materials for SOFCs (> 1 S cm^{-1}). The Arrhenius plot shows a nearly perfect linear dependence over the entire temperature range studied, despite the change of structure evidenced at 475 °C. The activation energy values were taken from RT to 475 °C (light blue line-Rhombohedral structure) with E_{aR}= 0.13(8) and 0.19(9) eV for air and diluted hydrogen, respectively, and from 500 to 800 °C (red line-Cubic structure) with E_{aC}= 0.16(8) and 0.34(1) eV for air and diluted hydrogen, respectively; the increase of conductivity with temperature can be explained by a small polaron hopping transport mechanism, which attest for the semiconducting behavior. The above agrees with what is observed in doped perovskite manganites and is associated with the presence of the mixed valence Mn^{3+}/Mn^{4+} [145,147–151]. For example, Mizusaki reported this kind of semiconducting behavior in homologue $La_{1-x}Sr_xMnO_{3-\delta}$ (rhombohedral structure, x>3) when it does not pass the point of σ= 250 S cm^{-1} in air at 800 °C [107]; in our case the maximum is around 178 S cm^{-1} considering a semiconductor-type at the same temperature. These values on the other hand are higher than the recently reported by Hou *et al.* [147], and Choi *et al.* [152]; for example, $Sm_{0.5}Ba_{0.5}MnO_{3-\delta}$ presents a maximum conductivity in air and 5% H_2/Ar of 1.15 and 0.10 S cm^{-1} at 850 °C [147],respectively, and for $PrBa_{0.8}Ca_{0.2}Mn_2O_{5+\delta}$ 13.4 and 5.48 S cm^{-1} at 800 °C [152], respectively. In the first case, this can be explained due to the lower sintering temperature (950 °C) of the sample that leads to a higher porosity compared to the higher sintering temperature (1200 °C) used for LBMn.

Indeed, the conduction mechanism in the $La_{1-x}Ba_xMnO_3$ (LBMO) perovskite-manganites has been reported, with 0.15 < x < 0.2. The electronic properties are described by electron localization that leads to the formation of small polarons as mentioned above [153]. On the other hand, other authors agree that the conductivity is due to the mobile carriers holes localized at manganese and the hopping of the charge carrier (electrons); where electron holes are known to be the dominant charge carriers in $Ln_{1-x}A_xMnO_3$ (Ln: La, Sm, Pr, Nd and A: Ba, Sr, Ca) consisting in the nearest-neighbor hopping Mn cations, that is between pairs of Mn^{3+} and Mn^{4+} [145,151,154–156].

The drop-in conductivity observed in Figure 44 from air to reducing atmosphere is common in perovskite-like manganites; it is associated to the p-type conductivity and related to either the Mn^{3+}/Mn^{4+} or Mn^{3+}/Mn^{2+} mixed valence, the Mn^{3+} concentration decreasing during reduction in our case. However, and as already said, LBMn conductivity values in reducing atmosphere are sufficient for the application, and for example comparable to the conductivity level in the best MIEC anode $(La_{0.75}Sr_{0.25})_{0.95}Cr_{0.5}Mn_{0.5}O_{3-\delta}$ (LSCM), which is 20-35 S cm^{-1} in the range of 700-800 °C in oxidizing and moderate reducing conditions, respectively. [148].

4.5. ANALYSIS OF THE ELECTROCHEMICAL PROPERTIES (EIS) OF $La_4BaMn_5O_{13\pm\delta}$

The preliminary evaluation of the electrochemical behavior of $La_4BaMn_5O_{13\pm\delta}$ (LBMn) has been studied as a SOFC cathode in a symmetrical cell sintered at 950 °C. Unfortunately, the measurements in other sintering conditions as well as anode gas conditions were not possible. The electrochemical measurements were evaluated in air with no gas flow at 700, 750 and 800 °C. The impedance spectra were analyzed with an equivalent circuit with the interest to identify the processes that contribute to the polarization resistance (R_p), using Zview software [91] that allowed to condense the data into quantitative parameters, *i.e.* capacitance, characteristic frequency and the area specific resistance (ASR), following the equations described in section 2.2.5.2.1. In According to Table 17 and Figure 46 the area specific resistance (ASR) decreases as the temperature increases, at 800 °C obtaining a value of 2.2 Ω cm2; such ASR value is larger than that reported for LSM (0.43 Ω cm2 [121]) electrode of the state of art and much higher than for LBCo presented in this work. On the other hand, the polarization resistance value of LBMn at 750 °C reaches 9.6 Ω cm2 which is not far from the 8.67 Ω cm2 of Sm0.5Sr0.5MnO3 at the same temperature, the slight difference can be due to the sintering temperature used by Li et al., of 1020 °C for 2 hours. The activation energy obtained from the Arrhenius plot using the Log10 function as function of the reciprocal temperature [157] is 1.24(2) eV from the ASR value. This activation energy value is comparable to other perovskite manganites but lower than the disordered perovskite Sm0.5Sr0.5MnO3 (2.02 eV) and higher than La0.8Sr0.2MnO3 (0.79 eV) [120]. The resistive component of the low frequency arc (LF) in LBMn presents the highest contribution to the polarization resistance (Rp) as depicted in Figure 46(b). For example, the ASR value at 800 °C is ~95% constituted by the Warburg resistance contribution.

Figure 45 we can observe the impedance spectra obtained at 700, 750 and 800 °C, as well as the equivalent circuit used to fit each spectrum. The shape of each spectrum is similar, hence described by two limiting steps to explain the electrochemical process, making the equivalent circuit composed of an inductance (L) in series with an ohmic contribution (R_S), one (R_1 // CPE_1) element consisting of a resistance (R_1) in parallel with a constant phase element (CPE_1) and a Warburg (W_2) to be applied to all the range studied. The two present arcs were designated as high frequency (HF) for the constant phase element which is in the range of 10^3-10^2 Hz, and the low frequency to the Warburg element for the frequency range 10^1-10^{-3} Hz.

Table 17. Quantitative parameters for LBMn electrode sintered at 950 °C measured in air.

T	**R_S**	**LF1**			**LF**			**Rp**	**ASR**	**χ^2**
		R_1	**C_1**	***f***	**W_2**	**C_2**	***f***			
(°C)	**(Ω cm^2)**	**(Ω cm^2)**	**(F cm^{-2})**	**(Hz)**	**(Ω cm^2)**	**(F cm^{-2})**	**(Hz)**	**(Ω cm^2)**	**(Ω cm^2)**	
700	205.9	2.84	1.37E-05	4096.8	17.87	0.2391	0.05	20.71	10.355	1.2E-04
750	149	0.6755	5.09E-04	463.4	8.915	0.3997	0.08	9.5905	4.7952	5.4E-05
800	113.5	0.2291	1.84E-03	378.14	4.123	0.7384	0.11	4.3521	2.1761	7.7E-04

According to Table 17 and Figure 46 the area specific resistance (ASR) decreases as the temperature increases, at 800 °C obtaining a value of 2.2 Ω cm^2; such ASR value is larger than that reported for LSM (0.43 Ω cm^2 [121]) electrode of the state of art and much higher than for LBCo presented in this work. On the other hand, the polarization resistance value of LBMn at 750 °C reaches 9.6 Ω cm^2 which is not far from the 8.67 Ω cm^2 of $Sm_{0.5}Sr_{0.5}MnO_3$ at the same temperature, the slight difference can be due to the sintering temperature used by Li et al., of 1020 °C for 2 hours. The activation energy obtained from the Arrhenius plot using the Log_{10} function as function of the reciprocal temperature [157] is 1.24(2) eV from the ASR value. This activation energy value is comparable to other perovskite manganites but lower than the disordered perovskite $Sm_{0.5}Sr_{0.5}MnO_3$ (2.02 eV) and higher than $La_{0.8}Sr_{0.2}MnO_3$ (0.79 eV) [120]. The resistive component of the low frequency arc (LF) in LBMn presents the highest contribution to the polarization resistance (R_p) as depicted in Figure 46(b). For example, the ASR value at 800 °C is ~95% constituted by the Warburg resistance contribution.

Figure 45. Impedance spectra measured in air at (a) 700 °C, (b) 750 °C and (c) 800 °C for LBMn sintered at 950 °C. The serial resistance (R_S) has been removed[12].

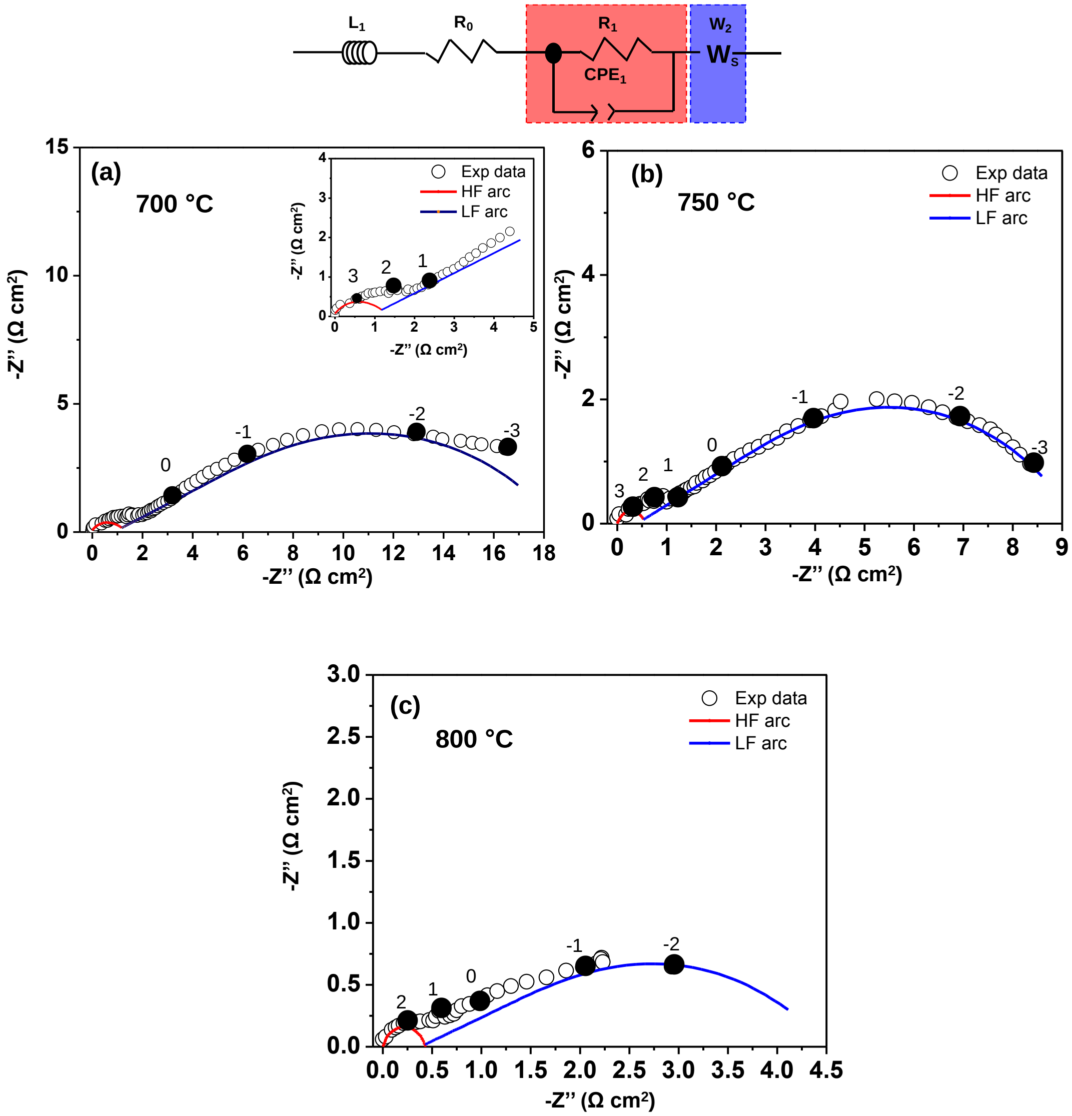

---

[12] To be able to compare easily the variation of R_p

Figure 46. Arrhenius plot of the (a) area specific resistance (ASR) and (b) individual resistances for LBMn sintered at 950 °C measured in air.

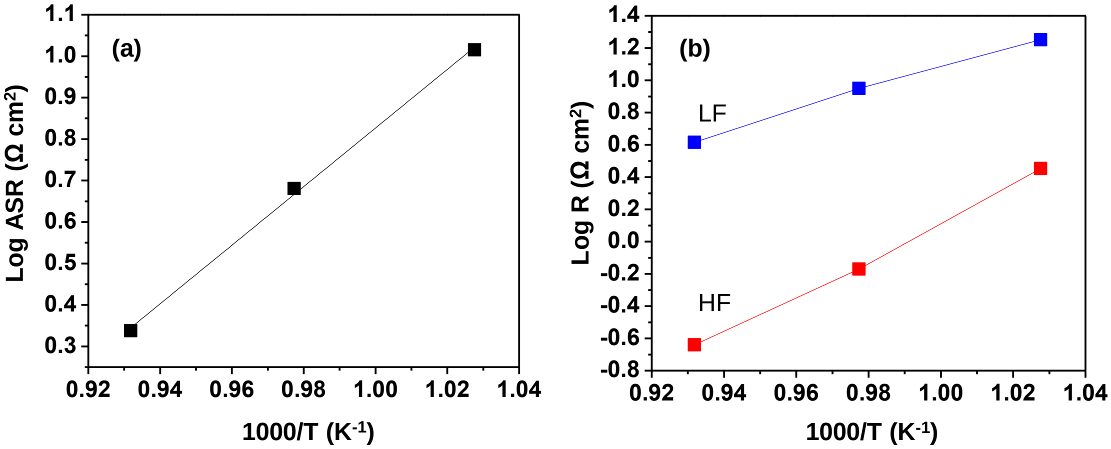

The capacitances of each process vary significantly with temperature; for the constant phase element (CPE) the values are in the range of 10^{-5}-10^{-3} F cm^{-2}, while for the Warburg element, the capacitance is in the order of 10^{-1} F cm^{-2}. According to the literature, the HF process could be associated either to a charge transfer that may be the electron transfer with ionic incorporation into the electrode or to a surface phenomenon as the dissociative adsorption of oxygen and/or surface diffusion of adsorbed oxygen Oad [92]. Tentatively the LF process can be related O^{2-} charge transfer in the electrode/electrolyte interface [92,120], this latter can be due to poor adherence between electrode and electrolyte due to low sintering temperature, as reported by some literature [158]. New measurements will be performed in the future, using for example higher sintering temperatures T ≥ 1000 °C. Additionally, the study of the pO_2 dependence on the EIS measurements will probably help to determine correctly the attribution of the limiting phenomena.

5. CONCLUSIONS

This work was focused on the synthesis, structural, electrical and electrochemical characterization of the ordered and disordered perovskites $La_4BaCu_{5-x}M_xO_{13\pm\delta}$ (M: Co, Mn), in order to determine their potential use as electrode materials for Symmetrical Solid Oxide Fuel Cells.

- Single phases compounds were obtained for x=0-2 and 5 in the $La_4BaCu_{5-x}Co_xO_{13\pm\delta}$ series, using a synthesis temperature of 950 °C/5h and, for $La_4BaCu_{5-x}Mn_xO_{13\pm\delta}$ family, x=0-1 and x=3-5 for a synthesis temperature of 950 °C and 1000 °C, respectively. Both families exhibit a tetragonal structure with space group *P*4/*m* for low substitution and a rhombohedral structure with space group $R\bar{3}c$ for high dopant concentration, with the coexistence of both structures for intermediate compositions.

- The $La_4BaCu_{5-x}Co_xO_{13\pm\delta}$ compounds are not stable in reducing atmosphere with partial destruction of the materials independently of the cobalt concentration, while, in contrast, $La_4BaCu_{5-x}Mn_xO_{13\pm\delta}$ (x= 4 and 5) are stable in reducing atmosphere maintaining the disordered $R\bar{3}c$ perovskite structure.

- $La_4BaCu_3Co_2O_{13\pm\delta}$ (LBCuCo2), $La_4BaCo_5O_{13\pm\delta}$ (LBCo) and $La_4BaMn_5O_{13\pm\delta}$ (LBMn) compositions were selected to be further studied in view of the application. The three compounds showed chemical compatibility with BCZY electrolyte in oxidizing atmosphere.

- The cobaltites present thermal expansions coefficients (TEC) that are relatively far from those of BCZY but conform to the expected values for cobaltites; interestingly, LBCuCo2 TEC value is the same as for Co-free LBCu ($La_4BaCu_5O_{13\pm\delta}$).

The Thermal Expansion Coefficient value for LBMn material matches better with BCZY electrolyte expansion coefficient, both in air and hydrogen conditions.

- $La_4BaCu_3Co_2O_{13\pm\delta}$ (LBCuCo2) and the perovskite-like manganite $La_4BaMn_5O_{13\pm\delta}$ (LBMn) presents a semiconducting behavior that suggests a temperature activated hole small polaronic mobility. The values are high enough to be used as electrode material for symmetrical SOFC.

- The preliminary impedance study for both LBCuCo2 and LBCo electrodes showed that the ASR (area specific resistance) decreases dramatically when the sintering temperature is increased from 950 to 1000 °C, due to a possibly better adhesion between the electrode and electrolyte. The elementary step that corresponds to the low frequencies changes from adsorption to gas diffusion through the pores.

- The comparison of the polarization resistance obtained for LBCo, LBCuCo2 and LBCu, confirm that an LBCo cathode would perform much better in a SOFC or IT SOFC since lower R_p values can be achieved.

- LBMn manganite presents an acceptable polarization resistance at 700 °C, the operation temperature of an IT-SOFC.

6. RECOMENDATIONS

For the study of stability of the materials in reducing medium it is recommended that the conditions of the flow of diluted hydrogen can be maintained a longer time in comparison with those worked in this thesis in order to evaluate the materials in conditions similar to those of operation of a SOFC cell.

Additionally, it is recommended to optimize the electrode electrochemical performance for the cobaltites and manganite by increasing the sintering temperature of the electrode to 1150 °C, as well as to perform the electrochemical measurements in anode conditions for the manganite (LBMn). Moreover, is also possible to explore the electrochemical performance with a deeper study of the pO_2 dependence on the EIS measurements that will probably help to determine correctly the attribution of all the limiting phenomena.

REFERENCES

[1] UPME, Balance de Gas Natural en Colombia 2015 - 2023, 2015, p 1–29.

[2] J.C. Ruiz-morales, J. Canales, PILAS DE COMBUSTIBLE DE OXIDOS SOLIDOS (SOFC), 2da Ed, CCPC, Santan Cruz de Tenerife, España, 2008.

[3] A. Atkinson, S. Barnett, R.J. Gorte, J.T.S. Irvine, Advanced anodes for high-temperature fuel cells., Nat. Mater. Vol 3 , 2004, p 17–27.

[4] A. Ovalle, J.C. Ruiz-Morales, J. Canales-Vázquez, D. Marrero-López, J.T.S. Irvine, Mn-substituted titanates as efficient anodes for direct methane SOFCs, Solid State Ionics. Vol 177, 2006, p 1997–2003.

[5] V. V Kharton, A.P. Viskup, E.N. Naumovich, F.M.B. Marques, Oxygen ion transport in La_2NiO_4 -based ceramics, J. Mater. Chem. Vol 9, 1999, p 2623–2629.

[6] S.J. Skinner, J.A. Kilner, Oxygen diffusion and surface exchange in $La_{2-x}Sr_xNiO_{4+\delta}$, Solid State Ionics. Vol 135, 2000, p 709–712.

[7] S. Choi, S. Park, J. Kim, T.-H. Lim, J. Shin, G. Kim, Electrochemical properties of an ordered perovskite $LaBaCo_2O_{5+\delta}$–$Ce_{0.9}Gd_{0.1}O_{2-\delta}$ composite cathode with strontium doping for intermediate-temperature solid oxide fuel cells, Electrochem. Commun. Vol 34, 2013, p 5–8.

[8] S. Pang, X. Jiang, X. Li, Z. Su, H. Xu, Q. Xu, C. Chen, Characterization of cation-ordered perovskite oxide $LaBaCo_2O_{5+\delta}$ as cathode of intermediate-temperature solid oxide fuel cells, Int. J. Hydrogen Energy. Vol 37, 2012, p 6836–6843.

[9] N. Li, Z. Lü, B. Wei, X. Huang, K. Chen, Y. Zhang, W. Su, Characterization of

$GdBaCo_2O_{5+\delta}$ cathode for IT-SOFCs, J. Alloys Compd. Vol 454, 2008, p 274–279.

[10] K. Zhang, L. Ge, R. Ran, Z. Shao, S. Liu, Synthesis, characterization and evaluation of cation-ordered $LnBaCo_2O_{5+\delta}$ as materials of oxygen permeation membranes and cathodes of SOFCs, Acta Mater. Vol 56, 2008, p 4876–4889.

[11] D. Chen, R. Ran, K. Zhang, J. Wang, Z. Shao, Intermediate-temperature electrochemical performance of a polycrystalline $PrBaCo_2O_{5+\delta}$ cathode on samarium-doped ceria electrolyte, J. Power Sources. Vol 188, 2009, p 96–105.

[12] J.H. Kim, A. Manthiram, Layered $LnBaCo_2O_{5+\delta}$ perovskite cathodes for solid oxide fuel cells: an overview and perspective, J. Mater. Chem. A. Vol 3, 2015, p 24195–24210.

[13] Y.N. Kim, A. Manthiram, Layered $LnBaCo_{2-x}Cu_xO_{5+\delta}$ „ $0 \leq x \leq 1.0$ Perovskite Cathodes for Intermediate-Temperature Solid Oxide Fuel Cells, J. Mater. Chem. Vol 1, 2011, p 276–282.

[14] J.-H. Kim, A. Manthiram, $LnBaCo_2O_{5+\delta}$ Oxides as Cathodes for Intermediate-Temperature Solid Oxide Fuel Cells, J. Electrochem. Soc. Vol 155, 2008, p B385.

[15] X. Che, Y. Shen, H. Li, T. He, Assessment of $LnBaCo_{1.6}Ni_{0.4}O_{5+\delta}$ (Ln = Pr, Nd, and Sm) double-perovskites as cathodes for intermediate-temperature solid-oxide fuel cells, J. Power Sources. Vol 222, 2013, p 288–293.

[16] C. Michel, L. Er-Rakho, B. Raveau, The oxygen defect perovskite $BaLa_4Cu_5O_{13.4}$, a metallic conductor, Mater. Res. Bull. Vol 20, 1985, p 667–671.

[17] L. Suescun, B. Dabrowski, S. Remsen, J. Mais, Synthesis and structural characterization of $La_xSr_{1-x}MnO_{2.6+\delta}$ (0.1<x<0.4) compounds displaying compressed

octahedral coordination of $Mn^{(4-5x)+}$, J. Solid State Chem. Vol 182, 2009, p 187–195.

[18] L. Suescun, Manganitas de estroncio y cupratos de lantano de formula general ABO_3 . Estructura y potenciales aplicaciones como c á todos de IT-SOFC. Seminario Invitado en Centro Atómico Bariloche, Bariloche, 2013.

[19] N. Hikosaka, Fuel cells: current technology challenges and future research needs, 1st Ed, Elsevier, London, United Kingdom, 2012.

[20] W.Z. Zhu, S.C. Deevi, A review on the status of anode materials for solid oxide fuel cells, Mater. Sci. Eng. A. Vol 362, 2003, p 228–239.

[21] A. Kirubakaran, S. Jain, R.K. Nema, A review on fuel cell technologies and power electronic interface, Renew. Sustain. Energy Rev. Vol 13, 2009, p 2430–2440.

[22] N. Mahato, A. Banerjee, A. Gupta, S. Omar, K. Balani, Progress in material selection for solid oxide fuel cell technology: A review, Prog. Mater. Sci. Vol 72, 2015, p 141–337.

[23] M.D. Gross, J.M. Vohs, R.J. Gorte, Recent progress in SOFC anodes for direct utilization of hydrocarbons, J. Mater. Chem. Vol 17, 2007, p 3071.

[24] C. Sun, U. Stimming, Recent anode advances in solid oxide fuel cells, J. Power Sources. Vol 171, 2007, p 247–260.

[25] U.C. Castillo, Generación de electricidad limpia y eficiente via electroquímica, Boletín lie, 1999.

[26] J. Larminie, A. Dicks, Fuel cell systems explained, 2nd Ed, Wiley, London, United Kingdom, 2003.

[27] Y.-H. Huang, R.I. Dass, Z.-L. Zing, J.B. Goodenough, Double Perovskites as Anode Materials for Solid-Oxide Fuel Cells, Science Vol 312, 2006, p 254–257.

[28] J.C. Ruiz-Morales, J. Canales-Vázquez, J. Peña-Martínez, D.M. López, P. Núñez, On the simultaneous use of $La_{0.75}Sr_{0.25}Cr_{0.5}Mn_{0.5}O_{3-\delta}$ as both anode and cathode material with improved microstructure in solid oxide fuel cells, Electrochim. Acta. Vol 52, 2006, p 278–284.

[29] J. Canales-Vázquez, J.C. Ruiz-Morales, D. Marrero-López, J. Peña-Martínez, P. Núñez, P. Gómez-Romero, Fe-substituted $(La,Sr)TiO_3$ as potential electrodes for symmetrical fuel cells (SFCs), J. Power Sources. Vol 171, 2007, p 552–557.

[30] F. Napolitano, A.L. Soldati, J. Geck, D.G. Lamas, A. Serquis, Electronic and structural properties of $La_{0.4}Sr_{0.6}Ti_{1-y}Co_yO_{3\pm\delta}$ electrode materials for symmetric SOFC studied by hard X-ray absorption spectroscopy, Int. J. Hydrogen Energy. Vol 38, 2013, p 8965–8973.

[31] R. Martínez-Coronado, A. Aguadero, D. Pérez-Coll, L. Troncoso, J.A. Alonso, M.T. Fernández-Díaz, Characterization of $La_{0.5}Sr_{0.5}Co_{0.5}Ti_{0.5}O_{3-\delta}$ as symmetrical electrode material for intermediate-temperature solid-oxide fuel cells, Int. J. Hydrogen Energy. Vol 37, 2012, p 18310–18318.

[32] M. Mogensen, N.M. Sammes, G.A. Tompsett, Physical, chemical and electrochemical properties of pure and doped ceria, Solid State Ionics. Vol 129, 2000, p 63–94.

[33] C. Déportes, M. Duclot, P. Fabry, J. Fouletier, Electrochimie Des Solides, Grenoble, 1994.

[34] H. Shinawi, Synthesis and Characterization of Cobalt-containing Perovskite-type Oxides, The university of Birmingham, 2010.

[35] J. Smith, William & Hashemi, Fundamentos de la ciencia e ingenieria de materiales, 4ta Ed, Mc Graw Hill, México, D.F., 2006.

[36] L. Zhu, R. Ran, M. Tad, W. Wang, Z. Shao, Perovskite materials in energy storage and conversion, Asia-Pacific J. Chem. Eng. Vol 11, 2016, p 338-369.

[37] M. Mogensen, SOFC fuel electrode kinetics and mechanisms, Solid State Electrochem Vol 100, 2005, p 5166.

[38] S. McIntosh, R.J. Gorte, Direct hydrocarbon solid oxide fuel cells, Chem. Rev. Vol 104, 2004, p 4845–4865.

[39] B. Steele, Fuel-cell technology: Running on natural gas, Nature. Vol 400, 1999, p 619–621.

[40] G. Pudmich, B.A. Boukamp, M. Gonzalez-Cuenca, W. Jungen, W. Zipprich, F. Tietz, Chromite/titanate based perovskites for application as anodes in solid oxide fuel cells, Solid State Ionics. Vol 135, 2000, p 433–438.

[41] S. Tao, J.T.S. Irvine, Synthesis and Characterization of $(La_{0.75}Sr_{0.25})Cr_{0.5}Mn_{0.5}O_{3-\delta}$, a Redox-Stable, Efficient Perovskite Anode for SOFCs, J. Electrochem. Soc. Vol 151, 2004, p A252–A259.

[42] S. Zha, P. Tsang, Z. Cheng, M. Liu, Electrical properties and sulfur tolerance of $La_{0.75}Sr_{0.25}Cr_{1-x}Mn_xO_3$ under anodic conditions, J. Solid State Chem. Vol 178, 2005, p 1844–1850.

[43] E. Lay, G. Gauthier, S. Rosini, C. Savaniu, J.T.S. Irvine, Ce-substituted LSCM as new anode material for SOFC operating in dry methane, Solid State Ionics. Vol 179, 2008, p 1562–1566.

[44] T. Delahaye, T. Jardiel, O. Joubert, R. Laucournet, G. Gauthier, M.T. Caldes, Electrochemical properties of novel SOFC dual electrode $La_{0.75}Sr_{0.25}Cr_{0.5}Mn_{0.3}Ni_{0.2}O_{3-\delta}$, Solid State Ionics. Vol 184, 2011, p 39–41.

[45] E. Lay, G. Gauthier, L. Dessemond, Preliminary studies of the new Ce-doped La/Sr chromo-manganite series as potential SOFC anode or SOEC cathode materials, Solid State Ionics. Vol 189, 2011, p 91–99.

[46] S. Tao, J.T.S. Irvine, A redox-stable efficient anode for solid-oxide fuel cells., Nat. Mater. Vol 2, 2003, p 320–323.

[47] S. Hashimoto, L. Kindermann, F.W. Poulsen, M. Mogensen, A study on the structural and electrical properties of lanthanum-doped strontium titanate prepared in air, J. Alloys Compd. Vol 397, 2005, p 245–249.

[48] M.R. Pillai, I. Kim, D.M. Bierschenk, S.A. Barnett, Fuel-flexible operation of a solid oxide fuel cell with $Sr_{0.8}La_{0.2}TiO_3$ support, J. Power Sources. Vol 185, 2008, p 1086–1093.

[49] O.A. Marina, N.L. Canfield, J.W. Stevenson, Thermal, electrical, and electrocatalytical properties of lanthanum-doped strontium titanate, Solid State Ionics. Vol 149, 2002, p 21–28.

[50] J. Canales-Vázquez, J.T.S. Irvine, W. Zhou, “Synthesis and characterization of n=5, 6 members of the $La_4Sr_{n-4}Ti_nO_{3n+2}$ series with layered structure based upon perovskite,” J. Solid State Chem. Vol 177, 2004, p 2039–2043.

[51] C. Périllat-Merceroz, G. Gauthier, P. Roussel, M. Huve, P. Gelin, R.N. Vannier, Synthesis and Study of a Ce-Doped La/Sr Titanate for Solid Oxide Fuel Cell Anode Operating Directly on Methane edric P, Chem. Mater. Vol 23, 2011, p 1539–1550.

[52] E. Siebert, A. Hammouche, M. Kleitz, Impedance spectroscopy analysis of $La_{1-x}Sr_xMnO_{3-\delta}$ yttria-stabilized zirconia electrode kinetics, Electrochim. Acta. Vol 40, 1995, p1741–1753.

[53] Y. Teraoka, H.M. Zhang, K. Okamoto, N. Yamazoe, Mixed ionic-electronic conductivity of $La_{1-x}Sr_xCo_{1-y}Fe_yO_{3-\delta}$ perovskite-type oxides, Mater. Res. Bull. Vol 23, 1988, p 51–58.

[54] K.T. Lee, a. Manthiram, Characterization of $Nd_{1-x}Sr_xCoO_{3-\delta}$ ($0 \le x \le 0.5$) Cathode Materials for Intermediate Temperature SOFCs, J. Electrochem. Soc. Vol 152, 2005, p A197.

[55] S. Park, S. Choi, J. Shin, G. Kim, Electrochemical investigation of strontium doping effect on high performance $Pr_{1-x}Sr_xCoO_{3-\delta}$ (x=0.1, 0.3, 0.5, and 0.7) cathode for intermediate-temperature solid oxide fuel cells, J. Power Sources. Vol 210, 2012, p 172–177.

[56] C. Xia, W. Rauch, F. Chen, M. Liu, $Sm_{0.5}Sr_{0.5}CoO_3$ cathodes for low-temperature SOFCs, Solid State Ionics. Vol 149, 2002, p 11–19.

[57] O. Gwon, S. Yoo, J. Shin, G. Kim, Optimization of $La_{1-x}Sr_xCoO_{3-\delta}$ perovskite cathodes for intermediate temperature solid oxide fuel cells through the analysis of crystal structure and electrical properties, Int. J. Hydrogen Energy. Vol 39, 2014, p 20806–20811.

[58] D. Huang, Q. Xu, W. Chen, H. Wang, Preparation Methods and Applications of Perovskite- type Composite Oxides $La_{1-x}Sr_xFe_{1-y}Co_yO_3$, Seminar: J. Nanjing Univ. Sci. Techonology.,2006

[59] Z. Shao, S.M. Haile, A high-performance cathode for the next generation of solid-oxide fuel cells., Nature. Vol 431, 2004, p 170–173.

[60] K. Efimov, Q. Xu, A. Feldhoff, Transmission Electron Microscopy Study of $Ba_{0.5}Sr_{0.5}Co_{0.8}Fe_{0.2}O_{3-\delta}$ Perovskite Decomposition at Intermediate Temperatures, Chem. Mater. vol 22, 2010, p 5866–5875.

[61] N.P. Bansal, T. Ishihara, Perovskite Oxide for Solid Oxide Fuel Cells, Media, 2009.

[62] B. Wang, G. Long, Y. Li, Y. Ji, Characterization of $SmBa_{0.5}Sr_{0.5}CoCuO_{5+\delta}$ cathode based on GDC and LSGM electrolyte for intermediate-temperature solid oxide fuel cells, Int. J. Hydrogen Energy. Vol 41, 2016, p 13603–13610.

[63] S. Lü, G. Long, Y. Ji, X. Meng, H. Zhao, C. Sun, $SmBaCoCuO_{5+\delta}$ as cathode material based on GDC electrolyte for intermediate-temperature solid oxide fuel cells, J. Alloys Compd. Vol 509, 2011, p 2824–2828.

[64] S.L. Pang, X.N. Jiang, X.N. Li, Q. Wang, Q.Y. Zhang, Structural stability and high-temperature electrical properties of cation-ordered/disordered perovskite LaBaCoO, Mater. Chem. Phys. Vol 131, 2012, p 642–646.

[65] T. Nakajima, M. Ichihara, Y. Ueda, New A-site ordered perovskite cobaltite $LaBaCo_2O_6$: Synthesis, structure, physical property and cation order-disorder effect, J. Phys. Soc. Japan. Vol 74, 2005, p 1572–1577.

[66] S.L. Pang, X.N. Jiang, X.N. Li, H.X. Xu, L. Jiang, Q.L. Xu, Y.C. Shi, Q.Y. Zhang, Structure and properties of layered-perovskite $LaBa_{1-x}Co_2O_{5+\delta}$ (x = 0-0.15) as intermediate-temperature cathode material, J. Power Sources. Vol 240, 2013, p 54–59.

[67] H. Yu, K. Fung, $La_{1-x}Sr_xCuO_{2.5-\delta}$ as new cathode materials for intermediate temperature solid oxide fuel cells, Mater. Res. Bull. Vol 38, 2003, p 231–239.

[68] H.-C. Yu, K.-Z. Fung, T.-C. Guo, W.-L. Chang, Syntheses of perovskite oxides nanoparticles $La_{1-x}Sr_xMO_{3-\delta}$ (M = Co and Cu) as anode electrocatalyst for direct methanol fuel cell, Electrochim. Acta. Vol 50, 2004, p 811–816.

[69] A. Berenov, J. Wei, H. Wood, R. Rudkin, A. Atkinson, Effect of aliovalent doping on the transport properties of lanthanum cuprates, J. Solid State Electrochem. Vol 11, 2007, p 482–489.

[70] F. Li, R. Zeng, L. Jiang, T. Wei, X. Lin, Y. Xu, Y. Huang, ScienceDirect Enhanced electrochemical activity in $Ca_3Co_2O_6$ cathode for solid-oxide fuel cells by Cu substitution, J. Mater. Vol 1, 2015, p 60–67.

[71] C. Michel, L.E. Rakho, M. Hervieu, J. Pannetier, B. Raveau, $BaLa_4Cu_5O_{13+\delta}$, an oxygen-deficient perovskite built up from corner-sharing CuO6 octahedra and CuO5 pyramids, J. Solid State Chem.Vol 68, 1987, p 143–152.

[72] P.K. Davies, C.M. Katzan, Oxidation and reduction of $BaLa_4Cu_5O_{13+\delta}$, J. Solid State Chem. Vol 88, 1990, p 368–383.

[73] P.S. Anderson, C.A. Kirk, J.M.S. Skakle, A.R. West, Synthesis and characterization of $La_4BaCu_5O_{13+\delta}$ and $La_4BaCu_{5-x}M_xO_{13+\delta}$: M=Fe, Co, Ni, Zn, J. Solid State Chem. Vol 170, 2003, p 1–8.

[74] M.A. Macias, M. V. Sandoval, N.G. Martinez, S. Vázquez-Cuadriello, L. Suescun, P. Roussel, K. Świerczek, G.H. Gauthier, Synthesis and preliminary study of $La_4BaCu_5O_{13+\delta}$ and $La_{6.4}Sr_{1.6}Cu_8O_{20\pm\delta}$ ordered perovskites as SOFC/PCFC electrode materials, Solid State Ionics. Vol 288, 2016, p 68–75.

[75] J.F. Basbus, M.D. Arce, F.D. Prado, A. Caneiro, L.V. Mogni, A high temperature study on thermodynamic, thermal expansion and electrical properties of $BaCe_{0.4}Zr_{0.4}Y_{0.2}O_{3-\delta}$ proton conductor, J. Power Sources. Vol 329, 2016, p 262–267.

[76] G. Taillades, P. Batocchi, M. Taillades, D. Jones, Chemically Stable Electrolytes and Adnvanced Electrode Architectures for Efficient Proton Ceramin Fuel Cells, Electrochem. Soc. Vol 35, 2011, p 805–811.

[77] K. Katahira, Y. Kohchi, T. Shimura, H. Iwahara, Protonic conduction in Zr-substituted $BaCeO_3$, Solid State Ionics. Vol 138, 2000, p 91–98.

[78] S. Hossain, A.M. Abdalla, S.N.B. Jamain, J.H. Zaini, A.K. Azad, A review on proton conducting electrolytes for clean energy and intermediate temperature-solid oxide fuel cells, Renew. Sustain. Energy Rev. Vol 79, 2017, p 750–764.

[79] C. Shivakumara, M.S. Hegde, H. Rajagopal, A. Sequiera, Neutron diffraction studies of $La_4BaCu_4MO_{13}$ (M = Ni and Co) oxides, Mater. Res. Bull. Vol 35, 2000, p 2063–2068.

[80] C. Shivakumara, Rapid Synthesis and Characterization of an Oxygen-Deficient Defect Perovskite $La_4BaCu_4MO_{13+\delta}$ Phase, ISRN Ceram.Vol 2011, 2011, p 1–4.

[81] M.L. Ruiz-González, R. Cortés-Gil, J.M. Alonso, A. Hernando, M. Vallet-Regí, J.M. González-Calbet, Structural ordering and ferromagnetism in $La_4Mn_4O_{11}$, Chem.

Mater. Vol 18, 2006, p 5756–5763.

[82] A. Kopp Alves, C.P. Bergmann, F.A. Berutti, Novel Synthesis and Characterization of Nanostructured Materials, 2013.

[83] M. Kakihana, Invited review “sol-gel” preparation of high temperature superconducting oxides, J. Sol-Gel Sci. Technol. Vol 6, 1996, p 7–55.

[84] M. Galceran, M.C. Pujol, M. Aguiló, F. Díaz, Sol-gel modified Pechini method for obtaining nanocrystalline $KRE(WO_4)_2$ (RE = Gd and Yb), J. Sol-Gel Sci. Technol. Vol 42, 2007, p 79–88.

[85] X. Zhang, J. Zhou, Y. Wang, Novel layered perovskite $GdBaCuFeO_{5+x}$ as a potential cathode for proton-conducting solid oxide fuel cells, Ionics Vol 19, 2013, p 941–945.

[86] J. Rodríguez-Carvajal, Recent advances in magnetic structure determination by neutron powder diffraction, Phys. B Condens. Matter. Vol 192, 1993, p 55–69.

[87] J. Rodríguez-Carvajal, WinPLOTR, Comimssion Powder Diffr. Newsl. Vol 26, 2001, p 12–19.

[88] S. Ricote, N. Bonanos, A. Manerbino, W.G. Coors, Conductivity study of dense $BaCe_xZr_{(0.9-x)}Y_{0.1}O_{(3-\delta)}$ prepared by solid state reactive sintering at 1500 °C, Int. J. Hydrogen Energy. Vol 37,2012, p 7954–7961.

[89] S.D. Zahid M., Arul Raj I., Tietz F., Lersch P., Electrical conductivity of perovskites in the quasi-ternary system $La_{0.8}Sr_{0.2}MnO_3$ - $La_{0.8}Sr_{0.2}CoO_3$ - $La_{0.8}Sr_{0.2}FeO_3$ for application as cathode-interconnect contact layer in sofc, Proc. - Electrochem. Soc.,Vol 7, 2005, p 1708–16.

[90] C. Setevich, L. Mogni, A. Caneiro, F. Prado, Characterization of the $La_{1-x}Ba_xCoO_{3-\delta}$ ($0 \leq x \leq 1$) System as Cathode Material for IT-SOFC, J. Electrochem. Soc. Vol 159, 2012, p B73.

[91] D. Johnson, Zview: a Software Program for IES Analysis, version 3.4c, Scribner Assoc. Inc., South. Pines, NC., 2004, 8886.

[92] L. Baqué, Preparación y caracterización de cátodos de alto rendimiento para Celdas de Combustible de Óxido Sólido de Temperatura Intermedia, Tesis de grado Universidad Nacional de Cuyo, 2011.

[93] C. Martínez, Propiedades de las perovskitas ABO3 (A=La,Ba y B=Co,Fe) como material de catodo en celdas de combustible IT-SOFC, Tesis de grado Universidad Nacional del Sur, 2014.

[94] E. Chinarro, J.R. Jurado, F.M. Figueiredo, J.R. Frade, Bulk and grain boundary conductivity of $Ca_{0.97}Ti_{1-x}Fe_xO_{3-\delta}$ materials, Solid State Ionics. Vo 160, 2003, p 161–168.

[95] P. Hjalmarsson, M. Søgaard, M. Mogensen, Electrochemical behaviour of $(La_{1-x}Sr_x)_sCo_{1-y}Ni_yO_{3-\delta}$ as porous SOFC cathodes, Solid State Ionics. Vol 180, 2009, p 1395–1405.

[96] W. Luo, F. Wang, Powder X-ray diffraction and Rietveld analysis of $La_{1-x}Ba_xCoO_3$ ($0<X<0.5$), Powder Diffr. Vol 21, 2006, p 304–306.

[97] W. Luo, F. Wang, Phase separation in the spin-state transition system of $La_{1-x}Ba_xCoO_3$, J. Solid State Chem. Vol 182, 2009, p 3171–3176.

[98] P. Granger, V. Parvulescu, S. Kaliaguine, Perovskites and Related Mixed Oxides: Concepts and Applications, Wiley-VCH, 2015.

[99] K. Xie, S. Tao, S. Tao, Conductivity and redox stability of new perovskite oxides $SrFe_{0.7}TM_{0.2}Ti_{0.1}O_{3-\delta}$ (TM?=?Mn, Fe, Co, Ni, Cu), Solid State Ionics. Vol 301, 2017, p 99–105.

[100] S.M. Bukhari, J.B. Giorgi, Effect of cobalt substitution on thermal stability and electrical conductivity of $Sm_{0.95}Ce_{0.05}FeO_{3-\delta}$ in oxidizing and reducing conditions, Solid State Ionics. Vol 181, 2010, p 392–401.

[101] R.E. Taylor, C.Y. Ho, Thermal Expansion of Solids, ASM International, Materials Park (OH), USA, 1998.

[102] G.A. Tompsett, N.M. Sammes, O. Yamamoto, Ceria-yttria-stabilized zirconia composite ceramic systems for applications as low-temperature electrolytes, J. Am. Ceram. Soc. Vol 80, 1997, p 3181–3186.

[103] H. Hayashi, T. Saitou, N. Maruyama, H. Inaba, K. Kawamura, M. Mori, Thermal expansion coefficient of yttria stabilized zirconia for various yttria contents, Solid State Ionics. Vol 176, 2005, p 613–619.

[104] Z. Naiqing, S. Kening, Z. Derui, J. Dechang, Study on Properties of LSGM Electrolyte Made by Tape Casting Method and Applications in SOFC, J. Rare Earths. Vol 24, 2006, p 90–92.

[105] F. Tietz, Thermal expansion of SOFC materials, Ionics Vol 5, 1999, p 129–139.

[106] C.F. Setevich, L. V. Mogni, A. Caneiro, F.D. Prado, Optimum cathode

configuration for IT-SOFC using $La_{0.4}Ba_{0.6}CoO_{3-\delta}$ and $Ce_{0.9}Gd_{0.1}O_{1.95}$, Int. J. Hydrogen Energy. Vol 37, 2012, p 14895–14901.

[107] J. Mizusaki, Nonstoichiometry, diffusion, and electrical properties of perovskite-type oxide electrode materials, Solid State Ionics. Vol 52, 1992, p 79–91.

[108] B. Dabrowski, K. Rogacki, X. Xiong, P.W. Klamut, R. Dybzinski, J. Shaffer, Synthesis and properties of the vacancy-free $La_{1-x}Ba_xMnO_3$, Phys. Rev. B. Vol 58, 1998, p 2716–2723.

[109] M. Gao, C.J. Li, C.X. Li, G.J. Yang, S.Q. Fan, Microstructure, oxygen stoichiometry and electrical conductivity of flame-sprayed $Sm_{0.7}Sr_{0.3}CoO_{3-\delta}$, J. Power Sources. Vol 191, 2009, p 275–279.

[110] T. Ishihara, S. Fukui, H. Nishiguchi, Y. Takita, Mixed electronic-oxide ionic conductor of $BaCoO_3$ doped with La for cathode of intermediate-temperature-operating solid oxide fuel cell, Solid State Ionics. Vol 152–153, 2002, p 609–613.

[111] E. Mitberg, High-temperature electrical conductivity and thermopower in nonstoichiometric $La_{1-x}Sr_xCoO_{3-\delta}$ (x=0.6), Solid State Ionics. Vol 130, 2000, p 325–330.

[112] J. Hjelm, M. Sogaard, R. Knibbe, A. Hagen, M. Mogensen, Electrochemical characterization of planar anode supported SOFC with strontium-doped lanthanum Cobalt Oxide Cathodes, ECS Trans. Vol 13, 2008, p 285–299.

[113] R. Amin, K. Karan, Characterization of $La_{0.5}Ba_{0.5}CoO_{3-\delta}$ as a SOFC Cathode Material, J. Electrochem. Soc. Vol 157, 2010, p B285.

[114] Y. Guo, H. Shi, R. Ran, Z. Shao, Performance of $SrSc_{0.2}Co_{0.8}O_{3-\delta}$ +

$Sm_{0.5}Sr_{0.5}CoO_{3-\delta}$ mixed-conducting composite electrodes for oxygen reduction at intermediate temperatures, Int. J. Hydrogen Energy. Vol 34, 2009, p 9496–9504.

[115] R.D. Shannon, Revised effective ionic radii and systematic studies of interatomic distances in Halides and Chalcogenides, Acta Cryst. Vol 32, 1976, p 751–945.

[116] A. Tarancón, D. Marrero-lópez, J. Peña-martínez, J.C. Ruiz-morales, P. Núñez, Effect of phase transition on high-temperature electrical properties of $GdBaCo_2O_{5+x}$ layered perovskite, Solid State Ionics Vol 179, 2008, p 611–618.

[117] S. Streule, A. Podlesnyak, D. Sheptyakov, E. Pomjakushina, M. Stingaciu, K. Conder, M. Medarde, M. V Patrakeev, I.A. Leonidov, V.L. Kozhevnikov, J. Mesot, High-temperature order-disorder transition and polaronic conductivity in $PrBaCo_2O_5$. Solid State Ionics Vol 48, 2006, p 3–7.

[118] M. Kriener, C. Zobel, a. Reichl, J. Baier, M. Cwik, K. Berggold, H. Kierspel, O. Zabara, a. Freimuth, T. Lorenz, Structure, magnetization, and resistivity of $La_{1-x}M_xCoO_3$ (M=Ca, Sr, and Ba), Phys. Rev. B. Vol 69, 2004, p 94417.

[119] F. Tietz, I. Arul Raj, M. Zahid, D. Stöver, Electrical conductivity and thermal expansion of $La_{0.8}Sr_{0.2}(Mn,Fe,Co)O_{3-\delta}$ perovskites, Solid State Ionics. Vol 177, 2006, p 1753–1756.

[120] W. Li, J. Pu, B. Chi, L. Jian, $Sm_{0.5}Sr_{0.5}MnO_3$ as a potential cathode material for intermediate temperature solid oxide fuel cells, Electrochim. Acta. Vol 141, 2014, p 189–194.

[121] E.C. Thomsen, G.W. Coffey, L.R. Pederson, O.A. Marina, Performance of lanthanum strontium manganite electrodes at high pressure, J. Power Sources. Vol

191, 2009, p 217–224.

[122] M.J.L. Ostergard, M.B. Mogensen, ac Impedance study of the oxygen reduction mechanism on LSM in SOFC, Electrochim. Acta. Vol 38, 1993, p 2015–2020.

[123] H.C. Yu, K.Z. Fung, Electrode properties of $La_{1-x}Sr_xCuO_{2.5-\delta}$ as new cathode materials for intermediate-temperature SOFCs, J. Power Sources. Vol 133, 2004, p 162–168.

[124] S. Vázquez, J. Basbus, A.L. Soldati, F. Napolitano, A. Serquis, L. Suescun, Effect of the symmetric cell preparation temperature on the activity of $Ba_{0.5}Sr_{0.5}Fe_{0.8}Cu_{0.2}O_{3-\delta}$ as cathode for intermediate temperature solid oxide fuel cells, J. Power Sources. Vol 274, 2015, p 318–323.

[125] A.A. Taskin, A.N. Lavrov, Y. Ando, Fast oxygen diffusion in A-site ordered perovskites, Prog. Solid State Chem. Vol 35, 2007, p 481–490.

[126] X. Ding, C. Cui, L. Guo, Thermal expansion and electrochemical performance of $La_{0.7}Sr_{0.3}CuO_{3-\delta}$ -$Sm_{0.2}Ce_{0.8}O_{2-\delta}$ composite cathode for IT-SOFCs, J. Alloys Compd. Vol 481, 2009, p 845–850.

[127] Y.P. Wang, Q. Xu, D.P. Huang, K. Zhao, M. Chen, B.H. Kim, Survey on electrochemical properties of $La_{2-x}Sr_xNiO_{4\pm\delta}$ ($x=0.2$ and 0.8, $\delta>0$) cathodes related with structural stability under cathodic polarization conditions, Int. J. Hydrogen Energy. Vol 42, 2017, p 6290–6302.

[128] L. Mogni, N. Grunbaum, F. Prado, A. Caneiro, Oxygen Reduction Reaction on Ruddlesden–Popper Phases Studied by Impedance Spectroscopy, J. Electrochem. Soc. Vol 158, 2011, p B202.

[129] J. Nielsen, J. Hjelm, Impedance of SOFC electrodes: A review and a comprehensive case study on the impedance of LSM:YSZ cathodes, Electrochim. Acta. Vol 115, 2014, p 31–45.

[130] N. Hildenbrand, P. Nammensma, D.H.A. Blank, H.J.M. Bouwmeester, B.A. Boukamp, Influence of configuration and microstructure on performance of $La_2NiO_{4+\delta}$ intermediate-temperature solid oxide fuel cells cathodes, J. Power Sources. Vol 238, 2013, p 442–453.

[131] A. Chang, S.J. Skinner, J.A. Kilner, Electrical properties of $GdBaCo_2O_{5+x}$ for ITSOFC applications, Solid State Ionics. Vol 177, 2006, p 2009–2011.

[132] J.H. Kim, Y. Kim, P.A. Connor, J.T.S. Irvine, J. Bae, W. Zhou, Structural, thermal and electrochemical properties of layered perovskite $SmBaCo_2O_{5+\delta}$, a potential cathode material for intermediate-temperature solid oxide fuel cells, J. Power Sources. Vol 194, 2009, 704–711.

[133] A. Esquirol, N.P. Brandon, J.A. Kilner, M. Mogensen, Electrochemical characterization of $La_{0.6}Sr_{0.4}Co_{0.2}Fe_{0.8}O_3$ cathodes for intermediate-temperature SOFCs, J. Electrochem. Soc. Vol 151, 2004, p A1847–A1855.

[134] A. Ringued, J. Fouletier, Oxygen reaction on strontium-doped lanthanum cobaltite dense electrodes at intermediate temperatures, Solid State Ionics. Vol 139, 2001, p 167–177.

[135] S. Pang, X. Jiang, X. Li, Q. Wang, Z. Su, A comparative study of electrochemical performance of $La_{0.5}Ba_{0.5}CoO_{3-\delta}$ and $La_{0.5}Ba_{0.5}CoO_{3-\delta}$–$Gd_{0.1}Ce_{0.9}O_{1.95}$ cathodes, Int. J. Hydrogen Energy. Vol 37, 2012, p 2157–2165.

[136] D.A. Garcés, Estudio de perovskitas $LaBaCo_2O_{6-\delta}$: Propiedades de alta temperatura y su evaluación como potenciales materiales para celdas de combustible o electrolíticas de óxido sólido., Tesis de grado Universidad Nacional de Cuyo, 2012.

[137] R. Dhama, C. Nayek, C. Thirmal, P. Murugavel, Enhanced magnetic properties in low doped $La_{1-x}Ba_xMnO_{3+\delta}$ (x=0, 0.1 and 0.2) nanoparticles, J. Magn. Magn. Mater. Vol 364, 2014, p 125–128.

[138] S. V. Trukhanov, Magnetic and magnetotransport properties of $La_{1-x}Ba_xMnO_{3-x/2}$ perovskite manganites, J. Mater. Chem. Vol 13, 2003, p 347–352.

[139] S. Balamurugan, K.S.A. Mini, T.S.G. Raja, P. Parthiban, Mechano-Thermal Synthesis and Characterization of $BaMnO_3$; Nano-Needles, J. Nanosci. Nanotechnol. Vol 15, 2015, 5978–5986.

[140] F. Tonus, M. Bahout, V. Dorcet, G. Gauthier, S. Paofai, R.I. Smith, S.J. Skinner, Redox behavior of the SOFC electrode candidate $NdBaMn_2O_{5+d}$ investigated by high-temperature in situ neutron diffraction: first characterisation in real time of an LnBaMn2O5.5, J. Mater. Chem. A. Vol 4, 2016, p 11635–11647.

[141] M. V. Sandoval, C. Pirovano, E. Capoen, R. Jooris, F. Porcher, P. Roussel, G.H. Gauthier, In-depth study of the Ruddlesden-Popper $La_xSr_{2-x}MnO_{4\pm\delta}$ family as possible electrode materials for symmetrical SOFC, Int. J. Hydrogen Energy. Vol 42, 2017, 1–14.

[142] A. Faes, A. Nakajo, A. Hessler-Wyser, D. Dubois, A. Brisse, S. Modena, J. Van herle, RedOx study of anode-supported solid oxide fuel cell, J. Power Sources. Vol 193, 2009, p 55–64.

[143] D. Waldbillig, A. Wood, D.G. Ivey, Thermal analysis of the cyclic reduction and oxidation behaviour of SOFC anodes, Solid State Ionics. Vol 176, 2005, p 847–859.

[144] Y. Shirai, S.I. Hashimoto, K. Sato, K. Yashiro, K. Amezawa, J. Mizusaki, T. Kawada, Crystal structure and thermal expansion behavior of oxygen stoichiometric lanthanum strontium manganite at high temperature, Solid State Ionics. Vol 256, 2014, p 83–88.

[145] A.N. Demina, K.P. Polovnikova, E.A. Filonova, A.N. Petrov, A.K. Demin, E.Y. Pikalova, Thermal expansion and electrical conductivity of $La_{0.7}Sr_{0.3}Mn_{1-y}Cr_yO_3$, Inorg. Mater. Vol 43, 2007, p 430–435.

[146] O.L. Pineda, Z.L. Moreno, P. Roussel, Ś. Konrad, G.H. Gauthier, Synthesis and preliminary study of the double perovskite $NdBaMn_2O^{5+\delta}$ as symmetric SOFC electrode material, Vol 5, 2016, p 1–7.

[147] N. Hou, P. Li, T. Lv, T. Yao, X. Yao, T. Gan, L. Fan, P. Mao, Y. Zhao, Y. Li, $Sm_{0.5}Ba_{0.5}MnO_{3-\delta}$ anode for solid oxide fuel cells with hydrogen and methanol as fuels, J Catal. Today. Vol 298, 2017, p 33-39.

[148] V. V. Kharton, E. V. Tsipis, I.P. Marozau, A.P. Viskup, J.R. Frade, J.T.S. Irvine, Mixed conductivity and electrochemical behavior of $(La_{0.75}Sr_{0.25})_{0.95}Cr_{0.5}Mn_{0.5}O_{3-\delta}$, Solid State Ionics. Vol 178, 2007, p 101–113.

[149] V.L. Kozhevnikov, I.A. Leonidov, E.B. Mitberg, M. V. Patrakeev, Y.M. Baikov, V.S. Zakhvalinskii, E. Lähderanta, High-temperature thermopower and conductivity of $La_{1-x}Ba_xMnO_3$ ($0.02 \le x \le 0.35$), J. Solid State Chem. Vol 172, 2003, p 1–5.

[150] I.A. Leonidov, E.I. Konstantinova, M. V. Patrakeev, A.A. Markov, V.L.

Kozhevnikov, Electrical conductivity and carrier mobility in $Ca_{1-x}Pr_xMnO_{3-\delta}$ manganites, Inorg. Mater. Vol 53, 2017, p 589–594.

[151] I. Mansuri, D. Varshney, Structure and electrical resistivity of $La_{1-x}Ba_xMnO_3$ ($0.25 \leq x \leq 0.35$) perovskites, J. Alloys Compd. Vol 513, 2012, p 256–265.

[152] S. Choi, S. Sengodan, S. Park, Y.-W. Ju, J. Kim, J. Hyodo, H.Y. Jeong, T. Ishihara, J. Shin, G. Kim, A robust symmetrical electrode with layered perovskite structure for direct hydrocarbon solid oxide fuel cells: $PrBa_{0.8}Ca_{0.2}Mn_2O_{5+\delta}$, J. Mater. Chem. A. Vol 4, 2016, p 1747–1753.

[153] R. Laiho, K.G. Lisunov, E. Lähderanta, M.A. Shakhov, V.N. Stamov, V.S. Zakhvalinskii, V.L. Kozhevnikov, I.A. Leonidov, E.B. Mitberg, M. V Patrakeev, Mechanisms of hopping conductivity in weakly doped $La_{1-x}Ba_xMnO_3$, J. Phys. Condens. Matter. Vol 17, 2005, p 3429–3444.

[154] E. Markiewicz, R. Bujakiewicz-Koronska, A. Budziak, A. Kalvane, D.M. Nalecz, Impedance spectroscopy studies of $SrMnO_3$,$BaMnO_3$ and $Ba_{0.5}Sr_{0.5}MnO_3$ ceramics, Phase Transitions. Vol 87, 2014, p 1060–1072.

[155] A.K. Kundu, Magnetic Perovskites: Synthesis, Structure and Physical Properties, India, 2016.

[156] J.F. Jurado, J.A. Játiva, Metal-insulator transition and hopping conduction mechanisms in the $La_{0.7}Ba_{0.3}MnO_3$ compound, J. Magn. Magn. Mater. Vol 335, 2013, p 6–10.

[157] E. Schouler, Study of oxide electrolyte based cells by the complex impedance techinique-application to the accurate measurement of conductivity and to the study of the oxygen electrode reaction, France, 1979.

[158] S. Sunde, Calculations of impedance of composite anodes for solid oxide fuel cells, Electrochim. Acta. Vol 42, 1997, p 2637–2648.

[159] J. Rodríguez-Carvajal, FULLPROF: A program for Rietveld Refinement and Pattern Matching AnalysisAbstracts of the Satellite Meeting on Powder Diffraction of the XV Congress of the IUCr., Phys. B Condens. Matter. Vol 192, 1990, p 127.

[160] R. Macdonald, Impedance spectroscopy, Ann. Biomed. Eng. Vol 20, 1992, p 289–305.

[161] V. Sense, Electrochemical Impedance Spectroscopy (EIS): A Powerful and Cost- Effective Tool for Fuel Cell Diagnostics, J. Mat. Cell. Vol 35, 1990, p 1–5.

BIBLIOGRAPHY

Amin R., Karan K. Characterization of $La_{0.5}Ba_{0.5}CoO_{3-\delta}$ as a SOFC Cathode Material, J. Electrochem. Soc. Vol 157, 2010, B285.

Anderson P.S., Kirk C.A., Skakle J.M., West A.R., Synthesis and characterization of $La_4BaCu_5O_{13+\delta}$ and $La_4BaCu_{5-x}M_xO_{13+\delta}$: M=Fe, Co, Ni, Zn, J. Solid State Chem. Vol 170, 2003, p 1–8.

Atkinson A., Barnett S., Gorte R., Irvine J. Advanced anodes for high-temperature fuel cells., Nat. Mater. Vol 3, 2004, p 17–27.

Balamurugan S., Mini K.S.A.,. Raja T.S.G, Parthiban P., Mechano-Thermal Synthesis and Characterization of $BaMnO_3$; Nano-Needles, J. Nanosci. Nanotechnol. Vol 15, 2015, p 5978–5986.

Bansal N.P., Ishihara T., Perovskite Oxide for Solid Oxide Fuel Cells, Media.,2009.

Baqué L., Preparación y caracterización de cátodos de alto rendimiento para Celdas de Combustible de Óxido Sólido de Temperatura Intermedia, Universidad Nacional de Cuyo, 2011.

Basbus J.F., Arce M.D., Prado F.D., Caneiro A., Mogni L.V., A high temperature study on thermodynamic, thermal expansion and electrical properties of $BaCe_{0.4}Zr_{0.4}Y_{0.2}O_{3-\delta}$ proton conductor, J. Power Sources. Vol 329, 2016, p 262–267.

Berenov A., Wei J., Wood H., Rudkin R., Atkinson A., Effect of aliovalent doping on the transport properties of lanthanum cuprates, J. Solid State Electrochem. Vol 11, 2007, p 482–489.

Bukhari S.M., Giorgi J.B., Effect of cobalt substitution on thermal stability and electrical conductivity of $Sm_{0.95}Ce_{0.05}FeO_{3-\delta}$ in oxidizing and reducing conditions, Solid State Ionics. Vol 181, 2010, p 392–401.

Canales-Vázquez J., Irvine J.T.S., Zhou W., Synthesis and characterization of n=5, 6 members of the $La_4Sr_{n-4}Ti_nO_{3n+2}$ series with layered structure based upon perovskite, J. Solid State Chem. Vol 177, 2004, p 2039–2043.

Canales-Vázquez J., Ruiz-Morales J.C., Marrero-López D., Peña-Martínez J., Núñez P., Gómez-Romero P., Fe-substituted (La,Sr)TiO_3 as potential electrodes for symmetrical fuel cells (SFCs), J. Power Sources. Vol 171, 2007, p 552–557.

Castillo U.C., Generación de electricidad limpia y eficiente via electroquímica, Boletín lie, 1999.

Chang A., Skinner S.J., Kilner J.A., Electrical properties of $GdBaCo_2O_{5+x}$ for ITSOFC applications, Solid State Ionics. 177 (2006) 2009–2011.

Che X., Shen Y., Li H., He T., Assessment of $LnBaCo_{1.6}Ni_{0.4}O_{5+\delta}$ (Ln = Pr, Nd, and Sm) double-perovskites as cathodes for intermediate-temperature solid-oxide fuel cells, J. Power Sources. Vol 222, 2013, p 288–293.

Chen D., Ran R., Zhang K., Wang J., Shao Z., Intermediate-temperature electrochemical performance of a polycrystalline $PrBaCo_2O_{5+\delta}$ cathode on samarium-doped ceria electrolyte, J. Power Sources. Vol 188, 2009, p 96–105.

Chinarro E., Jurado J.R., Figueiredo F.M., Frade J.R., Bulk and grain boundary conductivity of $Ca_{0.97}Ti_{1-x}Fe_xO_{3-\delta}$ materials, Solid State Ionics. Vol 160, 2003, 161–168.

Choi S., Park S., Kim J., Lim T., Shin J., Kim G., Electrochemical properties of an ordered perovskite $LaBaCo_2O_{5+\delta}$–$Ce_{0.9}Gd_{0.1}O_{2-\delta}$ composite cathode with strontium doping for intermediate-temperature solid oxide fuel cells, Electrochem. Commun. Vol 34, 2013, p 5–8.

Choi S., Sengodan S., Park S., Ju W., Kim J., Hyodo J., Jeong H.Y., Ishihara T., Shin J., Kim G., A robust symmetrical electrode with layered perovskite structure for direct hydrocarbon solid oxide fuel cells: $PrBa_{0.8}Ca_{0.2}Mn_2O_{5+\delta}$, J. Mater. Chem. A. Vol 4, 2016, p 1747–1753.

Dabrowski B., Rogacki K., Xiong X., Klamut P.W., Dybzinski R., Shaffer J., Synthesis and properties of the vacancy-free $La_{1-x}Ba_xMnO_3$, Phys. Rev. B. Vol 58, 1998, p 2716–2723.

Davies P.K., Katzan C.M., Oxidation and reduction of $BaLa_4Cu_5O_{13+\delta}$, J. Solid State Chem. Vol 88, 1990, p 368–383.

Delahaye T., Jardiel T., Joubert O., Laucournet R., Gauthier G., Caldes M.T., Electrochemical properties of novel SOFC dual electrode $La_{0.75}Sr_{0.25}Cr_{0.5}Mn_{0.3}Ni_{0.2}O_{3-\delta}$, Solid State Ionics. Vol 184, 2011, p 39–41.

Demina A.N., Polovnikova K.P., Filonova E.A., Petrov A.N., Demin A.K., Pikalova E.Y., Thermal expansion and electrical conductivity of $La_{0.7}Sr_{0.3}Mn_{1-y}Cr_yO_3$, Inorg. Mater. Vol 43, 2007, p 430–435.

Déportes C., Duclot M., Fabry P., Fouletier J., Electrochimie Des Solides, Grenoble, 1994.

Dhama R., Nayek C., Thirmal C., Murugavel P., Enhanced magnetic properties in low doped $La_{1-x}Ba_xMnO_{3+\delta}$ (x=0, 0.1 and 0.2) nanoparticles, J. Magn. Magn. Mater.

Vol 364, 2014, p 125–128.

Ding X., Cui C., Guo L., Thermal expansion and electrochemical performance of $La_{0.7}Sr_{0.3}CuO_{3-\delta}$ -$Sm_{0.2}Ce_{0.8}O_{2-\delta}$ composite cathode for IT-SOFCs, J. Alloys Compd. Vol 481, 2009, p 845–850.

Efimov K., Xu Q., Feldhoff A., Transmission Electron Microscopy Study of $Ba_{0.5}Sr_{0.5}Co_{0.8}Fe_{0.2}O_{3-\delta}$ Perovskite Decomposition at Intermediate Temperatures, Chem. Mater. Vol 22, 2010, p 5866–5875.

Esquirol A., Brandon N.P., Kilner J.A., Mogensen M., Electrochemical characterization of $La_{0.6}Sr_{0.4}Co_{0.2}Fe_{0.8}O_3$ cathodes for intermediate-temperature SOFCs, J. Electrochem. Soc. Vol 151, 2004, p A1847–A1855.

Faes A., Nakajo A., Hessler-Wyser A., Dubois D., Brisse A., Modena S., Van herle J., RedOx study of anode-supported solid oxide fuel cell, J. Power Sources. Vol 193, 2009, p 55–64.

Galceran M., Pujol M.C., Aguiló M., Díaz F., Sol-gel modified Pechini method for obtaining nanocrystalline $KRE(WO_4)_2$ (RE = Gd and Yb), J. Sol-Gel Sci. Technol. Vol 42, 2007, p 79–88.

Gao M., Li C.J., Li C.X., Yang G.J., Fan S.Q., Microstructure, oxygen stoichiometry and electrical conductivity of flame-sprayed $Sm_{0.7}Sr_{0.3}CoO_{3-\delta}$, J. Power Sources. Vol 191, 2009, p 275–279.

Garcés D.A., Estudio de perovskitas $LaBaCo_2O_{6-\delta}$: Propiedades de alta temperatura y su evaluación como potenciales materiales para celdas de combustible o electrolíticas de óxido sólido., Tesis de grado Universidad Nacional de Cuyo, 2012.

Granger P., Parvulescu V., Kaliaguine S., Perovskites and Related Mixed Oxides: Concepts and Applications, Wiley-VCH, 2015.

Gross M.D., Vohs J.M., Gorte R.J., Recent progress in SOFC anodes for direct utilization of hydrocarbons, J. Mater. Chem. Vol 17, 2007, p 3071.

Guo Y., Shi H., Ran R., Shao Z., Performance of $SrSc_{0.2}Co_{0.8}O_{3-\delta}$ + $Sm_{0.5}Sr_{0.5}CoO_{3-\delta}$ mixed-conducting composite electrodes for oxygen reduction at intermediate temperatures, Int. J. Hydrogen Energy. Vol 34, 2009, p 9496–9504.

Gwon O., Yoo S., Shin J., Kim G., Optimization of $La_{1-x}Sr_xCoO_{3-\delta}$ perovskite cathodes for intermediate temperature solid oxide fuel cells through the analysis of crystal structure and electrical properties, Int. J. Hydrogen Energy. Vol 39, 2014, p 20806–20811.

Hashimoto S., Kindermann L., Poulsen F.W., Mogensen M., A study on the structural and electrical properties of lanthanum-doped strontium titanate prepared in air, J. Alloys Compd. Vol 397, 2005, p 245–249.

Hayashi H., Saitou T., Maruyama N., Inaba H., Kawamura K., Mori M., Thermal expansion coefficient of yttria stabilized zirconia for various yttria contents, Solid State Ionics. Vol 176, 2005, p 613–619.

Hikosaka N., Fuel cells: current technology challenges and future research needs, 1st Ed, Elsevier, London, United Kingdom, 2012.

Hildenbrand N., Nammensma P., Blank D.H.A., Bouwmeester H.J.M., Boukamp B.A., Influence of configuration and microstructure on performance of $La_2NiO_{4+\delta}$ intermediate-temperature solid oxide fuel cells cathodes, J. Power Sources. Vol 238, 2013, p 442–453.

Hjalmarsson P., Søgaard M., Mogensen M., Electrochemical behaviour of $(La_{1-x}Sr_x)_sCo_{1-y}Ni_yO_{3-\delta}$ as porous SOFC cathodes, Solid State Ionics. Vol180, 2009, p 1395–1405.

Hjelm J., Sogaard M., Knibbe R., Hagen A., Mogensen M., Electrochemical characterization of planar anode supported SOFC with strontium-doped lanthanum Cobalt Oxide Cathodes, ECS Trans. Vol 13, 2008, p 285–299.

Hossain S., Abdalla A.M., Jamain S.N.B., Zaini J.H., Azad A.K., A review on proton conducting electrolytes for clean energy and intermediate temperature-solid oxide fuel cells, Renew. Sustain. Energy Rev. Vol 79, 2017, p 750–764.

Hou N., Li P., $Sm_{0.5}Ba_{0.5}MnO_{3-\delta}$ anode for solid oxide fuel cells with hydrogen and methanol as fuels, J. Catal. Vol 298, 2017, p 33-39.

Huang D., Xu Q., Chen W., Wang H., Preparation Methods and Applications of Perovskite- type Composite Oxides $La_{1-x}Sr_xFe_{1-y}Co_yO_3$, J. Nanjing Univ. Sci. Techonology, 2006.

Huang Y.H., Dass R.I., Zing Z.L., Goodenough J.B., Double Perovskites as Anode Materials for Solid-Oxide Fuel Cells, Science Vol 312, 2006, p 254–257.

Ishihara T., Fukui S., Nishiguchi H., Takita Y., Mixed electronic-oxide ionic conductor of $BaCoO_3$ doped with La for cathode of intermediate-temperature-operating solid oxide fuel cell, Solid State Ionics. Vol 152–153, 2009, p 609–613.

Johnson D., Zview: a Software Program for IES Analysis, version 3.4c, Scribner Assoc. Inc., South. Pines, NC., 2004, 8886.

Jurado J.F., Játiva J.A., Metal-insulator transition and hopping conduction mechanisms in the $La_{0.7}Ba_{0.3}MnO_3$ compound, J. Magn. Magn. Mater. Vol 335, 2013, p 6–10.

Katahira K., Kohchi Y., Shimura T., Iwahara H., Protonic conduction in Zr-substituted $BaCeO_3$, Solid State Ionics. Vol 138, 2000, p 91–98.

Kakihana M., Invited review “sol-gel” preparation of high temperature superconducting oxides, J. Sol-Gel Sci. Technol. Vol 6, 1996, p 7–55.

Kharton V. V, Viskup A.P., Naumovich E.N., Marques F.M.B., Oxygen ion transport in La_2NiO_4 -based ceramics, J. Mater. Chem. Vol 9, 1999, p 2623–2629.

Kharton V. V., Mixed conductivity and electrochemical behavior of $(La_{0.75}Sr_{0.25})_{0.95}Cr_{0.5}Mn_{0.5}O_{3-\delta}$, Solid State Ionics. Vol 178, 2007, p 101–113.

Kim J.H., A. Manthiram A., $LnBaCo_2O_{5+\delta}$ Oxides as Cathodes for Intermediate-Temperature Solid Oxide Fuel Cells, J. Electrochem. Soc. Vol 155, 2008, p B385.

Kim J.H., Structural, thermal and electrochemical properties of layered perovskite $SmBaCo_2O_{5+\delta}$, a potential cathode material for intermediate-temperature solid oxide fuel cells, J. Power Sources. Vol 194, 2009, p 704–711.

Kim J.H., Manthiram A., Layered $LnBaCo_2O_{5+\delta}$ perovskite cathodes for solid oxide fuel cells: an overview and perspective, J. Mater. Chem. A. Vol 3, 2015, p 24195–24210.

Kim Y.N., Manthiram A., Layered $LnBaCo_{2-x}Cu_xO_{5+\delta}$ „ $0\leq x\leq 1.0$ Perovskite Cathodes for Intermediate-Temperature Solid Oxide Fuel Cells, J. Mater. Chem. A. Vol 2, 2011, p 276–282.

Kirubakaran A., Jain S., Nema R.K., A review on fuel cell technologies and power electronic interface, Renew. Sustain. Energy Rev. Vol 13, 2009, p 2430–2440.

Kopp Alves A., Bergmann C.P., Berutti F.A., Novel Synthesis and Characterization of Nanostructured Materials, 2013.

Kozhevnikov V.L., High-temperature thermopower and conductivity of $La_{1-x}Ba_xMnO_3$ ($0.02 \leq x \leq 0.35$), J. Solid State Chem. Vol 172, 2003, p 1–5.

Kriener M., Structure, magnetization, and resistivity of $La_{1-x}M_xCoO_3$ (M=Ca, Sr, and Ba), Phys. Rev. B. Vol 69, 2004, p 94417.

Kundu A.K., Magnetic Perovskites: Synthesis, Structure and Physical Properties, India, 2016.

Laiho R., Mechanisms of hopping conductivity in weakly doped $La_{1-x}Ba_xMnO_3$, J. Phys. Condens. Matter. Vol 17, 2005, p 3429–3444.

Larminie J., Dicks A., Fuel cell systems explained, 2nd Ed, Wiley, London, United Kingdom, 2003.

Lay E., Gauthier G., Rosini S., Savaniu C., Irvine J.T.S., Ce-substituted LSCM as new anode material for SOFC operating in dry methane, Solid State Ionics. Vol 179, 2008, p 1562–1566.

Lay E., Gauthier G., Dessemond L., Preliminary studies of the new Ce-doped La/Sr chromo-manganite series as potential SOFC anode or SOEC cathode materials, Solid State Ionics. Vol 189, 2011, p 91–99.

Li N., et al. Characterization of $GdBaCo_2O_{5+\delta}$ cathode for IT-SOFCs, J. Alloys Compd. Vol 454, 2008, p 274–279.

Li W., Pu J., Chi B., Jian L., $Sm_{0.5}Sr_{0.5}MnO_3$ as a potential cathode material for intermediate temperature solid oxide fuel cells, Electrochim. Acta. Vol 141, 2014, p 189–194.

Lee K.T., Manthiram A., Characterization of $Nd_{1-x}Sr_xCoO_{3-\delta}$ ($0 \le x \le 0.5$) Cathode Materials for Intermediate Temperature SOFCs, J. Electrochem. Soc. Vol 152, 2005, p A197.

Leonidov I.A., Electrical conductivity and carrier mobility in $Ca_{1-x}Pr_xMnO_{3-\delta}$ manganites, Inorg. Mater. Vol 53, 2017, p 589–594.

Lü S., Long G., Ji Y., Meng X., Zhao H., Sun C., $SmBaCoCuO_{5+\delta}$ as cathode material based on GDC electrolyte for intermediate-temperature solid oxide fuel cells, J. Alloys Compd. Vol 509, 2011, p 2824–2828.

Luo W., Wang F., Powder X-ray diffraction and Rietveld analysis of $La_{1-x}Ba_xCoO_3$ ($0<X<0.5$), Powder Diffr. Vol 21, 2006, p 304–306.

Luo W., Wang F., Phase separation in the spin-state transition system of $La_{1-x}Ba_xCoO_3$, J. Solid State Chem. Vol 182, 2009, p 3171–3176.

Macdonald R., Impedance spectroscopy, Ann. Biomed. Eng. Vol 20, 1992, p 289–305.

Macias M.A., Sandoval M., Synthesis and preliminary study of $La_4BaCu_5O_{13+\delta}$ and $La_{6.4}Sr_{1.6}Cu_8O_{20\pm\delta}$ ordered perovskites as SOFC/PCFC electrode materials, Solid State Ionics. Vol 288, 2016, p 68–75.

Mahato N., Banerjee A., Gupta A., Omar S., Balani K., Progress in material selection for solid oxide fuel cell technology: A review, Prog. Mater. Sci. Vol 72, 2015, p 141–337.

Mansuri I., Varshney D., Structure and electrical resistivity of $La_{1-x}Ba_xMnO_3$ ($0.25 \leq x \leq 0.35$) perovskites, J. Alloys Compd. Vol 513, 2012, p 256–265.

Marina O.A., Canfield N.L., Stevenson J.W., Thermal, electrical, and electrocatalytical properties of lanthanum-doped strontium titanate, Solid State Ionics. Vol 149, 2002, p 21–28.

Markiewicz E., Impedance spectroscopy studies of $SrMnO_3$,$BaMnO_3$ and $Ba_{0.5}Sr_{0.5}MnO_3$ ceramics, Phase Transitions.Vol 87, 2014, p 1060–1072.

Martínez-Coronado R., Characterization of $La_{0.5}Sr_{0.5}Co_{0.5}Ti_{0.5}O_{3-\delta}$ as symmetrical electrode material for intermediate-temperature solid-oxide fuel cells, Int. J. Hydrogen Energy. Vol 37, 2012, p 18310–18318.

Martínez C., Propiedades de las perovskitas ABO3 (A=La,Ba y B=Co,Fe) como material de catodo en celdas de combustible IT-SOFC, Tesis de grado Universidad Nacional del Sur, 2014.

McIntosh S., Gorte R.J., Direct hydrocarbon solid oxide fuel cells, Chem. Rev. Vol 104, 2004, p 4845–4865.

Michel C., Er-Rakho L., Raveau B., The oxygen defect perovskite $BaLa_4Cu_5O_{13.4}$, a metallic conductor, Mater. Res. Bull. Vol 20,1985, p 667–671

Michel C., Rakho L.E., Hervieu M., Pannetier J., $BaLa_4Cu_5O_{13+\delta}$, an oxygen-deficient perovskite built up from corner-sharing CuO6 octahedra and CuO5 pyramids, J. Solid State Chem. Vol 68, 1987, p 143–152.

Mitberg E., High-temperature electrical conductivity and thermopower in nonstoichiometric $La_{1-x}Sr_xCoO_{3-\delta}$ (x=0.6), Solid State Ionics. Vol 130, 2000, p 325–330.

Mizusaki J., Nonstoichiometry, diffusion, and electrical properties of perovskite-type oxide electrode materials, Solid State Ionics.Vol 52, 1992, p 79–91.

Mogensen M., Sammes N.M., Tompsett G.A., Physical, chemical and electrochemical properties of pure and doped ceria, Solid State Ionics. Vol 129, 2000, p 63–94.

Mogensen M., SOFC fuel electrode kinetics and mechanisms, Solid State Electrochem. Vol 100, 2005, p 5166.

Mogni L., Grunbaum N., Prado F., Caneiro A., Oxygen Reduction Reaction on Ruddlesden–Popper Phases Studied by Impedance Spectroscopy, J. Electrochem. Soc. Vol 158, 2011, p B202.

Nakajima T., Ichihara M., Ueda Y., New A-site ordered perovskite cobaltite $LaBaCo_2O_6$: Synthesis, structure, physical property and cation order-disorder effect, J. Phys. Soc. Japan. Vol 74, 2005, p 1572–1577.

Napolitano F., Soldati A.L., Geck J., Electronic and structural properties of $La_{0.4}Sr_{0.6}Ti_{1-y}Co_yO_{3\pm\delta}$ electrode materials for symmetric SOFC studied by hard X-ray absorption spectroscopy, Int. J. Hydrogen Energy. Vol 38, 2013, p 8965–8973.

Nielsen J., Hjelm J., Impedance of SOFC electrodes: A review and a comprehensive case study on the impedance of LSM:YSZ cathodes, Electrochim. Acta. Vol 11, 2014, p 31–45.

Ostergard M.J.L., Mogensen M.B., AC Impedance study of the oxygen reduction mechanism on LSM in SOFC, Electrochim. Acta. Vol 38, 1993, p 2015–2020.

Ovalle A., Mn-substituted titanates as efficient anodes for direct methane SOFCs, Solid State Ionics. Vo 177, 2006, p 1997–2003.

Pang S., Characterization of cation-ordered perovskite oxide $LaBaCo_2O_{5+\delta}$ as cathode of intermediate-temperature solid oxide fuel cells, Int. J. Hydrogen Energy. Vol 37, 2012, p 6836–6843.

Pang S., Jiang X., Li X., A comparative study of electrochemical performance of $La_{0.5}Ba_{0.5}CoO_{3-\delta}$ and $La_{0.5}Ba_{0.5}CoO_{3-\delta}$–$Gd_{0.1}Ce_{0.9}O_{1.95}$ cathodes, Int. J. Hydrogen Energy. Vol 37, 2012, p 2157–2165.

Pang S.L., Structural stability and high-temperature electrical properties of cation-ordered/disordered perovskite LaBaCoO, Mater. Chem. Phys. Vol 131, 2012, p 642–646.

Pang S.L., Structure and properties of layered-perovskite $LaBa_{1-x}Co_2O_{5+\delta}$ (x = 0-0.15) as intermediate-temperature cathode material, J. Power Sources. Vol 240, 2013, p 54–59.

Park S., Choi S., Shin J., Electrochemical investigation of strontium doping effect on high performance $Pr_{1-x}Sr_xCoO_{3-\delta}$ (x=0.1, 0.3, 0.5, and 0.7) cathode for intermediate-temperature solid oxide fuel cells, J. Power Sources. Vol 210, 2012, p 172–177.

Périllat-Merceroz C., Synthesis and Study of a Ce-Doped La/Sr Titanate for Solid

Oxide Fuel Cell Anode Operating Directly on Methane edric P, Chem. Mater. Vol 23, 2011, p 1539–1550.

Pillai M.R., Fuel-flexible operation of a solid oxide fuel cell with $Sr_{0.8}La_{0.2}TiO_3$ support, J. Power Sources. Vol 185, 2008, p 1086–1093.

Pineda O.L., et al. Synthesis and preliminary study of the double perovskite $NdBaMn_2O^{5+\delta}$ as symmetric SOFC electrode material, Int. J. Hydrogen Energy. Vol 5, 2016, p 1–7.

Pudmich G., Chromite/titanate based perovskites for application as anodes in solid oxide fuel cells, Solid State Ionics. Vol 135, 2000, p 433–438.

Ricote S., Bonanos N., Manerbino A., Conductivity study of dense $BaCe_xZr_{(0.9-x)}Y_{0.1}O_{(3-\delta)}$ prepared by solid state reactive sintering at 1500 °C, Int. J. Hydrogen Energy. Vol 37, 2012, p 7954–7961.

Ringued A., Fouletier J., Oxygen reaction on strontium-doped lanthanum cobaltite dense electrodes at intermediate temperatures, Solid State Ionics. Vol 139, 2001, p 167–177.

Rodríguez-Carvajal J., FULLPROF: A program for Rietveld Refinement and Pattern Matching AnalysisAbstracts of the Satellite Meeting on Powder Diffraction of the XV Congress of the IUCr., Phys. B Condens. Matter. Vol 192, 1990, p 127.

Rodríguez-Carvajal J., Recent advances in magnetic structure determination by neutron powder diffraction, Phys. B Condens. Matter. Vol 192, 1993, p 55–69.

Rodríguez-Carvajal J., WinPLOTR, Comimssion Powder Diffr. Newsl. Vol 26, 2001, p 12–19.

Ruiz-Morales J.C., On the simultaneous use of $La_{0.75}Sr_{0.25}Cr_{0.5}Mn_{0.5}O_{3-\delta}$ as both anode and cathode material with improved microstructure in solid oxide fuel cells, Electrochim. Acta. Vol 52, 2006, p 278–284.

Ruiz-González M.L., Structural ordering and ferromagnetism in $La_4Mn_4O_{11}$, Chem. Mater. Vol 18, 2006, p 5756–5763.

Ruiz J.C. y Canales J. Pilas de combustible de óxidos sólidos (SOFC), 2nd Ed., CCPC, Santa Cruz de Tenerife, España, 2008.

Sandoval M.V., In-depth study of the Ruddlesden-Popper $La_xSr_{2-x}MnO_{4\pm\delta}$ family as possible electrode materials for symmetrical SOFC, Int. J. Hydrogen Energy. Vol 42, 2017, p 1–14.

Schouler E., Study of oxide electrolyte based cells by the complex impedance techinique-application to the accurate measurement of conductivity and to the study of the oxygen electrode reaction, France, 1979.

Sense. V, Electrochemical Impedance Spectroscopy (EIS): A Powerful and Cost-Effective Tool for Fuel Cell Diagnostics, J. Mat. Cell. Vol 35, 1990, p 1–5.

Setevich C., Mogni L., Caneiro A., Characterization of the $La_{1-x}Ba_xCoO_{3-\delta}$ ($0 \leq x \leq 1$) System as Cathode Material for IT-SOFC, J. Electrochem. Soc. Vol 159, 2012, p B73.

Shannon R.D., Revised effective ionic radii and systematic studies of interatomic distances in Halides and Chalcogenides, Acta Cryst. Vol 32, 1976, p 751–945.

Shao Z., Haile S.M., A high-performance cathode for the next generation of solid-oxide fuel cells., Nature. Vol 431, 2004, p 170–173.

Shirai Y., Crystal structure and thermal expansion behavior of oxygen stoichiometric lanthanum strontium manganite at high temperature, Solid State Ionics. Vol 256, 2014, p 83–88.

Shivakumara C., Hegde M.S., Rajagopal H., Neutron diffraction studies of $La_4BaCu_4MO_{13}$ (M = Ni and Co) oxides, Mater. Res. Bull. Vol 35, 2000, p 2063–2068.

Shivakumara C., Rapid Synthesis and Characterization of an Oxygen-Deficient Defect Perovskite $La_4BaCu_4MO_{13+\delta}$ Phase, ISRN Ceram. Vol 2011, 2011, p 1–4.

Siebert E., Hammouche A., Kleitz M., Impedance spectroscopy analysis of $La_{1-x}Sr_xMnO_{3-\delta}$ yttria-stabilized zirconia electrode kinetics, Electrochim. Acta. Vol 40, 1995, p 1741–1753.

Skinner S.J., Kilner J.A., Oxygen diffusion and surface exchange in $La_{2-x}Sr_xNiO_{4+\delta}$, Solid State Ionics. Vol 135, 2000, p 709–712.

Smith J., William & Hashemi, Fundamentos de la ciencia e ingenieria de materiales, 4ta Ed, Mc Graw Hill, México, D.F., 2006.

Steele B., Fuel-cell technology: Running on natural gas, Nature. Vol 400, 1999, p 619–621.

Streule S., High-temperature order-disorder transition and polaronic conductivity in $PrBaCo_2O_5$ .J. Mat. Vol 48, 2006, p 3–7.

Suescun L., Dabrowski B., Remsen S., Synthesis and structural characterization of $La_xSr_{1-x}MnO_{2.6+\delta}$ (0.1<x<0.4) compounds displaying compressed octahedral coordination of $Mn^{(4-5x)+}$, J. Solid State Chem. Vol 182, 2009, p 187–195.

Suescun L., Manganitas de estroncio y cupratos de lantano de formula general ABO_3 . Estructura y potenciales aplicaciones como c á todos de IT-SOFC. Seminario Invitado en Centro Atómico Bariloche, Bariloche, 2013.

Sunde S., Calculations of impedance of composite anodes for solid oxide fuel cells, Electrochim. Acta.Vol 42, 1997, p 2637–2648.

Taillades G., Batocchi P., Taillades M., Jones D., Chemically Stable Electrolytes and Adnvanced Electrode Architectures for Efficient Proton Ceramin Fuel Cells, Electrochem. Soc. Vol 35, 2011, p 805–811.

Tao S., Irvine J.T.S., A redox-stable efficient anode for solid-oxide fuel cells., Nat. Mater. Vol 2, 2003, p 320–323.

Tao S., Irvine J.T.S., Synthesis and Characterization of $(La_{0.75}Sr_{0.25})Cr_{0.5}Mn_{0.5}O_{3-\delta}$, a Redox-Stable, Efficient Perovskite Anode for SOFCs, J. Electrochem. Soc. Vol 151, 2004, p A252–A259.

Tarancón A., Marrero-lópez D., Effect of phase transition on high-temperature electrical properties of $GdBaCo_2O_{5+x}$ layered perovskite, Solid State Ionics Vol 179, 2008, p 611–618.

Taskin A.A., Lavrov A.N., Ando Y., Fast oxygen diffusion in A-site ordered perovskites, Prog. Solid State Chem. Vol 35, 2007, p 481–490.

Taylor R.E., Ho C.Y., Thermal Expansion of Solids, ASM International, Materials Park (OH), USA, 1998.

Teraoka Y., Mixed ionic-electronic conductivity of $La_{1-x}Sr_xCo_{1-y}Fe_yO_{3-\delta}$ perovskite-type oxides, Mater. Res. Bull. Vol 23, 1988, p 51–58.

Thomsen E.C., Coffey G.W., Performance of lanthanum strontium manganite electrodes at high pressure, J. Power Sources. Vol 191, 2009, p 217–224.

Tietz F., Thermal expansion of SOFC materials, Solid State Ionics, Vol 5, 1999, p 129–139.

Tietz F., Arul Raj I., Zahid M., Electrical conductivity and thermal expansion of $La_{0.8}Sr_{0.2}(Mn,Fe,Co)O_{3-\delta}$ perovskites, Solid State Ionics. Vol 177, 2006, p 1753–1756.

Tompsett G.A., Sammes N.M., Yamamoto O., Ceria-yttria-stabilized zirconia composite ceramic systems for applications as low-temperature electrolytes, J. Am. Ceram. Soc. Vol 80, 1997, p 3181–3186.

Tonus F., Bahout M., Dorcet V., Redox behavior of the SOFC electrode candidate $NdBaMn_2O_{5+d}$ investigated by high-temperature in situ neutron diffraction: first characterisation in real time of an LnBaMn2O5.5, J. Mater. Chem. A. Vol 4, 2016, p 11635–11647.

Trukhanov S. V., Magnetic and magnetotransport properties of $La_{1–x}Ba_xMnO_{3–x/2}$ perovskite manganites, J. Mater. Chem. Vol 13, 2003, p 347–352.

UPME, Balance de Gas Natural en Colombia 2015 - 2023, 2015, p 1–29

Vázquez S., et al. Effect of the symmetric cell preparation temperature on the activity of $Ba_{0.5}Sr_{0.5}Fe_{0.8}Cu_{0.2}O_{3-\delta}$ as cathode for intermediate temperature solid oxide fuel cells, J. Power Sources. Vol 274, 2015, p 318–323.

Waldbillig D., Wood A., Ivey D.G., Thermal analysis of the cyclic reduction and oxidation behaviour of SOFC anodes, Solid State Ionics. Vol 176, 2005, p 847–859.

Wang B., Long G., Li Y., Characterization of $SmBa_{0.5}Sr_{0.5}CoCuO_{5+\delta}$ cathode based on GDC and LSGM electrolyte for intermediate-temperature solid oxide fuel cells, Int. J. Hydrogen Energy. Vol 41, 2016, p 13603–13610.

Wang Y.P., Xu Q., Huang D.P., Survey on electrochemical properties of $La_{2-x}Sr_xNiO_{4\pm\delta}$ (x=0.2 and 0.8, δ>0) cathodes related with structural stability under cathodic polarization conditions, Int. J. Hydrogen Energy. Vol 42, 2017, p 6290–6302.

Xia C., Rauch W., $Sm_{0.5}Sr_{0.5}CoO_3$ cathodes for low-temperature SOFCs, Solid State Ionics. Vol 149, 2002, p 11–19.

Xie K., Tao S., Conductivity and redox stability of new perovskite oxides $SrFe_{0.7}TM_{0.2}Ti_{0.1}O_{3-\delta}$ (TM?=?Mn, Fe, Co, Ni, Cu), Solid State Ionics. Vol 301, 2017, p 99–105.

Yu H., Fung K., $La_{1-x}Sr_xCuO_{2.5-\delta}$ as new cathode materials for intermediate temperature solid oxide fuel cells, Mater. Res. Bull. 38 (2003) 231–239.

Yu H., Fung K., Syntheses of perovskite oxides nanoparticles $La_{1-x}Sr_xMO_{3-\delta}$ (M = Co and Cu) as anode electrocatalyst for direct methanol fuel cell, Electrochim. Acta. Vol 50, 2004, p 811–816.

Yu H., Fung K., Electrode properties of $La_{1-x}Sr_xCuO_{2.5-\delta}$ as new cathode materials for intermediate-temperature SOFCs, J. Power Sources. Vol 133, 2004, p 162–168.

Zhang K., Ge L., Synthesis, characterization and evaluation of cation-ordered $LnBaCo_2O_{5+\delta}$ as materials of oxygen permeation membranes and cathodes of SOFCs, Acta Mater. Vol 56, 2008, p 4876–4889.

Zhu W.Z., Deevi S.C., A review on the status of anode materials for solid oxide fuel cells, Mater. Sci. Eng. A. Vol 362, 2003, p 228–239.

Zhu L., Ran R., Perovskite materials in energy storage and conversion, Asia-Pacific J. Chem. Eng. Vol 11, 2016, p 338-369.

Zha S., Tsang P., Cheng Z., Electrical properties and sulfur tolerance of $La_{0.75}Sr_{0.25}Cr_{1-x}Mn_xO_3$ under anodic conditions, J. Solid State Chem. Vol 178, 2005, p 1844–1850.

Zhang X., Zhou J., Wang Y., Novel layered perovskite $GdBaCuFeO_{5+x}$ as a potential cathode for proton-conducting solid oxide fuel cells, Ionics Vol 19, 2013, p 941–945.

Zahid S.D., Arul Raj I., Tietz F., Lersch P., Electrical conductivity of perovskites in the quasi-ternary system $La_{0.8}Sr_{0.2}MnO_3$ - $La_{0.8}Sr_{0.2}CoO_3$ - $La_{0.8}Sr_{0.2}FeO_3$ for application as cathode-interconnect contact layer in sofc, Proc. - Electrochem. Soc.,. Vol 7, 2005, p 1708–16.

ANNEXES

ANNEX A. Generalities of the Fullprof program

The Fullprof program has been designed primarily to perform the Rietveld analysis of neutron powder or X-ray diffraction data collected at constant or variable steps in the 2θ scattering angle or using the neutron flight time technique (TOF).

RIETVELD METHOD

The rietveld method [159] it is a complex minimization procedure that allows to slightly modify a preconceived model based on prior external knowledge, in order to adjust it to an experimental pattern. The starting parameters for this model must be similar to the final values, bearing in mind that the sequence in which the different parameters are refined have a marked influence on the final result. This method is a process of structural refinement that uses each point of the pattern as an observation data.

The adjustment of the diffraction profiles is carried out point by point in the diffractogram, allowing to perform an iterative adjustment process until reaching a convergence between the theoretical and the experimental. In this thesis, the refinements were made using the Fullprof program [159] and its WinPLOTR graphical interface. The values of standard deviations were calculated taking into account the correction of the Berar and Lelann equations.

The algorithms implemented to the Rietveld method use all the information contained in the diffractogram, including the one that is outside the diffraction peaks, some of these very useful variables are:

- The characteristics of the instrument (the resolution curve of the diffractometer, displacement parameters concerning the imbalances of the goniometer, experimental geometry, characteristics of the detector).
- Structural parameters (unit cell parameters, atomic positions, atomic occupations, atomic displacements).

- Microstructural parameters (average crystalline size and microtensions, structural defects).
- Parameters of the sample (preferential orientation, residual stress, eccentricity, thickness, transparency, absorption and phase fractions). The refined parameters were: background function, zero point position, scale factor, unit cell parameters, contribution to peak shape, U, V, W parameters and asymmetric coefficients.

The Rietveld method is based on a least squares function, which seeks to find the lowest possible value of the waste S_y which is defined as:

$$S_y = \sum_i w_i (y_i - y_{ci})^2 \quad (1)$$

Where; $w_i = \frac{1}{y_i}$, y_i is the experimental intensity observed in the *i* step of the diffractogram and y_{ci} in the intensity calculated for the *i* step. The mathematic definition of y_{ci} is shown in equation (2), which includes all the data that determine the intensity of a signal and that depend on the refined parameters.

$$y_{ci} = y_{bi} + \sum_{f=1}^{N} S_f \sum_{k=k1}^{k2} j_{fk} \cdot Lp_{fk} \cdot O_{fk} \cdot M \cdot \left|F_{fk}\right|^2 \cdot \Omega_{ifk} \quad (2)$$

Where:

y_{bi}= represents the intensity of the background at the point 2Ө.

S_f = represents the scale factor of phase f.

j_{fk}= is the Multiplicity factor of the k_i reflection.

Lp_{fk}= contains the correction factors of Lorentz-Polarization.

O_{fk}= it is a correction factor of absorption and / or microabsorption

$\left|F_{fk}\right|$= is the structure factor corresponding to the peak k of phase f

Ω_{ifk}= describes the shape function of the peaks

The first sum corresponds to all the crystalline phases present in the sample and the second summation to all the reflections k_1 to k_2 that contribute to the *i* step.

Peak parameters

The shape of the peak is an important factor when studying a sample by powder diffraction. The correct refinement of the peak shape is fundamental not only for a reasonable visual adjustment between the calculated and the observed intensity, but also so that the values of the structural parameters of the sample, dependent on the integrated intensity, have a physical sense. Although, in a diffraction profile it is observed that H (the maximum width at the average height of the peak) is a function of the dispersion vector module, in the absence of anisotropy by crystal size or reticular stresses, the H function can be modeled empirically. This means that the H parameter of each peak is not one of the variables in the adjustment, instead the coefficients of the equations that describe the variation of the maximum width to the average height of the peak are adjusted 2θ. For example, the case of the equation of Cagliotti, Pauletti and Ricci that describes the variation of H with θ for Gaussian profiles (3):

$$(FWHM)_G = H_k^2 = Utan^2(\theta) + Vtan(\theta) + W \tag{3}$$

Rietveld's refinement employs a profile function that models the diffraction peaks, by means of width at average height, asymmetry, preferential orientation, background, etc., the most commonly used functions are Gaussian (G), Lorentzian (L), Pseudo-Voigt and Pearson VII.

Generally, the practical procedure used to adjust the model to the data and avoid false minimums requires working with increasingly complex partial models where a series of reasonable values $(x_1, \ldots x_{m-n})_0$ of the initial parameters are left fixed, allowing the subset $(x_{m-n+1}, \ldots x_m)$ to vary until reaching the minimum. The model expands as the adjustment improves and the minimization function approaches the absolute minimum until, in a reasonable way, all the parameters of the model can be free to vary simultaneously in a stable manner. The selection of the different structural models of the respective phases to be refined by the Rietveld method, can be taken from the different databases of crystalline structures, such as the ICSD (International Centre Structural Database) (see http://barns.ill.fr/dif/icsd/), the Cambridge Structural Database System (see www.ccdc.cam.ac.uk) y la IUCr (International Unión Crystallographic) (http://www.iucr.ac.uk/iucr-top/comm/cpd/QARR/data-kit.htm).

Adjustment/Fix criteria

To achieve a precise adjustment of the measured intensities, it is necessary that the model used takes into account all the factors involved in the formation of the diffraction profile. The use of an incomplete model will inevitably lead to incorrect parameters $(x_1, \dots x_{m-n})$. However, even with an adequate model, the experimental errors in the measurement produce imbalances that can not be avoided. To advise on the degree of adjustment of the model to the data, it is necessary to use a series of numbers that indicate different relationships between the intensities observed (y_i) and those calculated (y_{cal}). This series of numbers are called refinement adjustment criteria, and are calculated from the residual values R_p (R-pattern), R_{wp} (R-weight pattern), R_{exp} (R-experimental), and x^2 whose expressions are shown below:

$$R_p = \sum |y_i - y_{ci}| / \sum |y_i| \tag{4}$$

$$R_{wp} = [\sum w_i (y_i - y_{ci})^2 / \sum w_i {y_i}^2]^{1/2} \tag{5}$$

$$R_{exp} = [(N - P) / \sum w_i {y_i}^2]^{1/2} \tag{6}$$

$$x^2 = GOF = \left[S_y/(N-P)\right]^{1/2} \tag{7}$$

R_p represents the direct relationship between the intensities observed and the experimental ones without any kind of weight between them. It is a very reliable parameter to observe during the minimization process since it responds to small changes in the degree of adjustment both in the background and in the maxima, however its value is always low since it is not heavy and usually represents more than the background (most of the points in a diffraction profile) than to the diffraction maxima.

R_{wp} is the main parameter of adjustment to be observed since in its numerator is the function that is minimized by the least squares method. Unlike the R_p it includes a function of weight on the intensities that gives greater importance to the imbalances in the high intensities (the diffraction peaks) than in the low ones (the background). It is the most significant parameter that is usually reported when publishing the results, since it gives us an indication of how good the refinement of the diffraction pattern.

R_{exp} is the so-called R expected, is the quotient between the degrees of freedom of the system and the sum of the standard deviations of the intensities. It is a lower bound of R_{wp} when the quality of the diffraction data is good.

x^2 is the parameter used to perform the goodness of fit test (GOF: goodness of fit). Numerically equal to the square root of S_y divided by the difference in the number of observations (N) and the number of adjusted parameters (P). Its expression is related to the parameters R_{wp} and R_e. This value tends to 1 when the adjustment is perfect, but when it takes values lower than 1 it can be concluded that the quality of the data (count statistics in each point, number of points, etc.) is insufficient to describe the number of parameters what is trying to adjust. You should opt for a simpler model or obtain a data set that is more appropriate to the model. In addition to the adjustment parameters mentioned above, there are others, such as R_B (R Factor - Bragg) and R_F (R Factor –estructure) which are calculated to advise the experimenter on the adjustment of the calculated intensities I_c (by integrating the curve adjusted to the experimental maximums) to the observed intensities I_o (determined by the numerical integration of the peaks in the region determined by the model).

$$R_B = \sum |I_O - I_C| / \sum |I_O| \tag{8}$$

$$R_F = \sum \left| {I_O}^{1/2} - {I_C}^{1/2} \right| / \sum \left| {I_O}^{1/2} \right| \tag{9}$$

These two parameters of adjustment do not take into account the intensities of the diffractogram zones where there are no diffraction maxima, therefore they are biased in favor of the structure, that is, it gives an indication of whether the chosen model has been correct. When the adjustment of the maxima is bad; but the measured and calculated intensities coincide, the value of these parameters is low, however, the other adjustment parameters of the diffraction profile are high. Therefore, the latter can only be used to compare the adjustment qualities of a structure to a data set if the adjustment parameters of the complete profile are comparable.

Although 6 numerical parameters have been mentioned that advise on the quality of the adjustment, the best indication of this can be obtained during the experiment, that is, by visual inspection of the curve y_i vs. 2θ when it is represented along with the curve y_{ci} vs. 2 θ, which also allows to analyze details of it in specific regions of the diffractogram. Additionally, it is very useful to represent the intensity difference curve $(y_i - y_{ci})$ vs. 2θ. In the latter, it is very easy to detect errors in the adjustment of the intensity, the shape of the peak, the background, etc., in specific regions of the diffraction profile that little affect the global adjustment parameters. Therefore, all the Rietveld refinement programs have a graphic program that updates the result of each refinement cycle automatically. [13]

---

[13] *SANDOVAL, Mónica V., Notas Personales (UIS, 2012).*

ANNEX B. Fundamentals of Electrochemical Impedance Spectroscopy (EIS)

Electrochemical Impedance Spectroscopy (EIS) is a powerful technique for fuel cell analysis allowing to extract information of oxygen reduction reaction (ORR), mass transfer or physicochemical properties of the system [160]. This is electrochemical method usually provides data measurement as real (Z’) and imaginary (Z’’) parts of the impedance and can be either represented as a Nyquist or Bode diagram ( ).

Figure B1. Nyquist and bode diagram for a Warburg and R//CPE elements impedance spectrum.

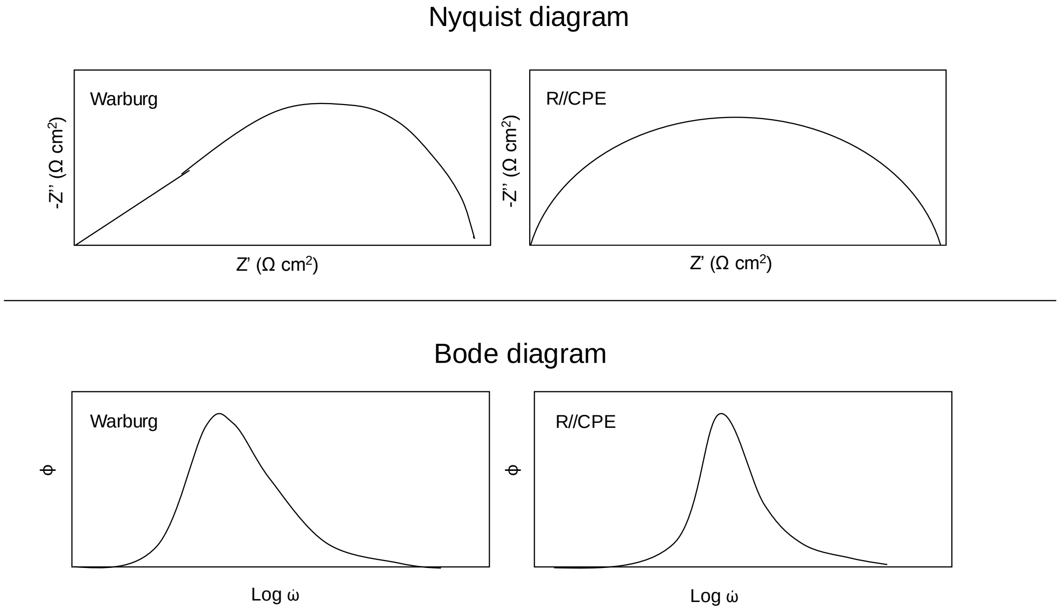

The Nyquist plot is the most used representation system and the information obtained from it is based on the shape adopted by the spectra, where the imaginary part(Z’’) is multiplied by -1 in the *y* axis while the real part (Z’) is graph in the *x* axis. On the other hand, the information based on a Bode plot is in order to observe the behavior of the frequency (ω), represented by the phase change (ϕ) as function of the frequency logarithm (Log ω). The interpretation of the EIS spectrums requires the selection of an adequate model, through the model, the measurements obtained using this technique provide information related to the resistance of the cell, the resistance and the capacitance of different polarization processes. The resistance of the cell is obtained at high frequencies and the data acquired at low frequencies give information on the kinetics of the reaction [161].

In the case of the Nyquist diagram, each point represents the impedance value at a frequency. The data at low frequencies are on the right side of the diagram, while the data at high frequencies are on the left of it. For instance, a Warburg element generates a different response shape from a parallel circuit R//CPE, the latter being generates a semicircle while the Warburg element starts with a straight line and ends in a semicircle as depicted in Figure #. In the case of the R//CPE, which impedance is:

$$Z_{CPE} = 1 / (T(jw)^{P}) \quad (1)$$

The value of *P* can be in the range of 0 to 1, when is between 0.9 and 1 it is usually related to porous systems, while at 0.5 is related with diffusive processes and 1 is an ideal capacitor. On the other hand, the fix parameters on the Warburg element are R_w, WT and WP, if WP = 0.5 the straight-line slope is of 45 ° and is usually used for diffusional processes [92]. Ultimately, to evaluate the global performance of the cell assembly, the area specific resistance (ASR) is deduce from the following formula:

$$ASR = \frac{R_p S}{2} \quad (2)$$

Where R_p is the polarization resistance and S is the surface area of the electrode (cm^2).

ANNEX C. Graphical results of Rietveld refinement of $La_4BaCu_{5-x}Co_xO_{13\pm\delta}$ series

Figure C1. Graphical result of Rietveld refinement of $La_4BaCu_5O_{13\pm\delta}$ (x= 0) synthesized.

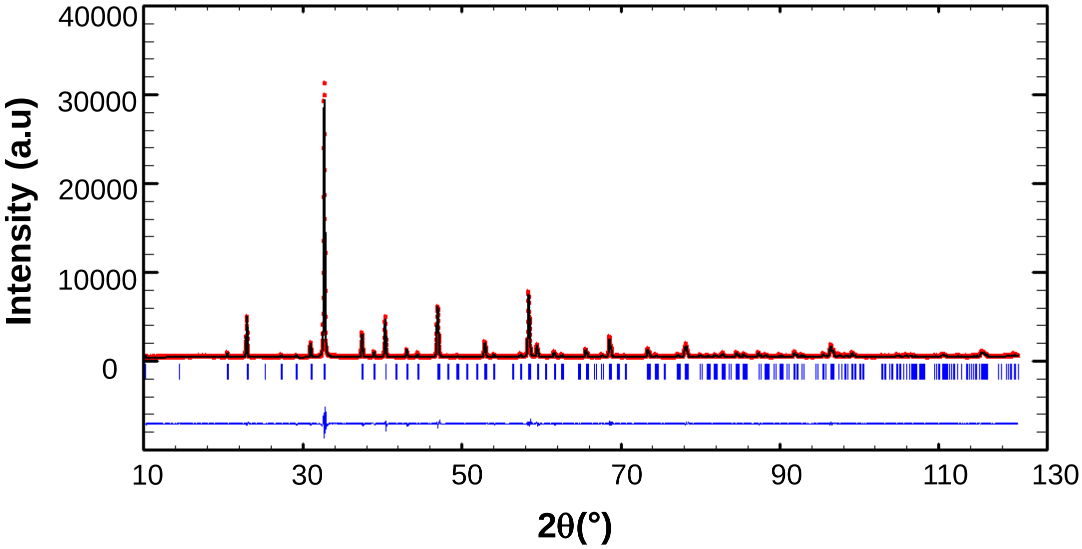

Figure C2. Graphical result of Rietveld refinement of $La_4BaCu_4CoO_{13\pm\delta}$ (x= 1) synthesized.

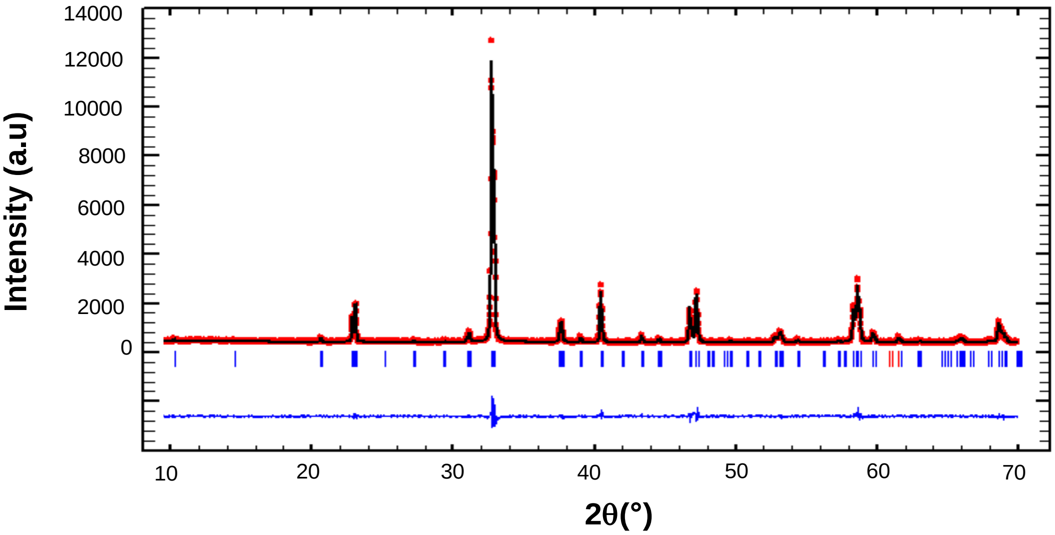

Figure C3.Graphical result of Rietveld refinement of $La_4BaCu_3Co_2O_{13\pm\delta}$ (x= 2) synthesized.

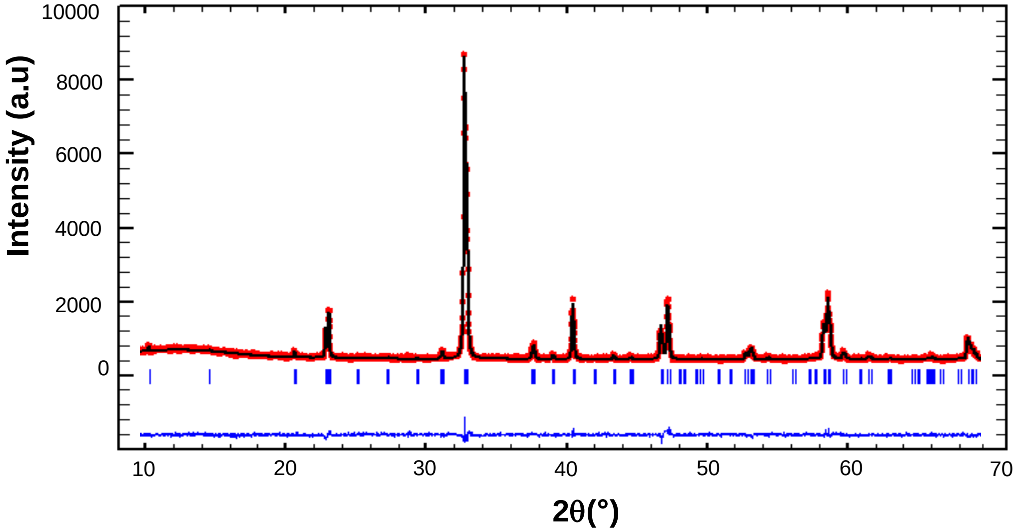

Figure C4.Graphical result of Rietveld refinement of $La_4BaCu_2Co_3O_{13\pm\delta}$ (x= 3) synthesized.

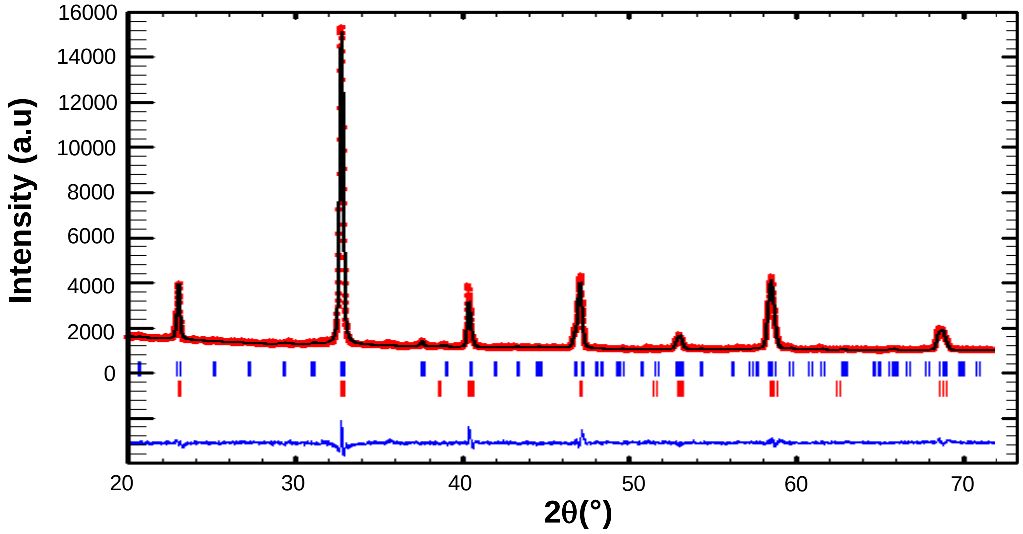

Figure C5. Graphical result of Rietveld refinement of $La_4BaCuCo_4O_{13\pm\delta}$ (x= 4) synthesized.

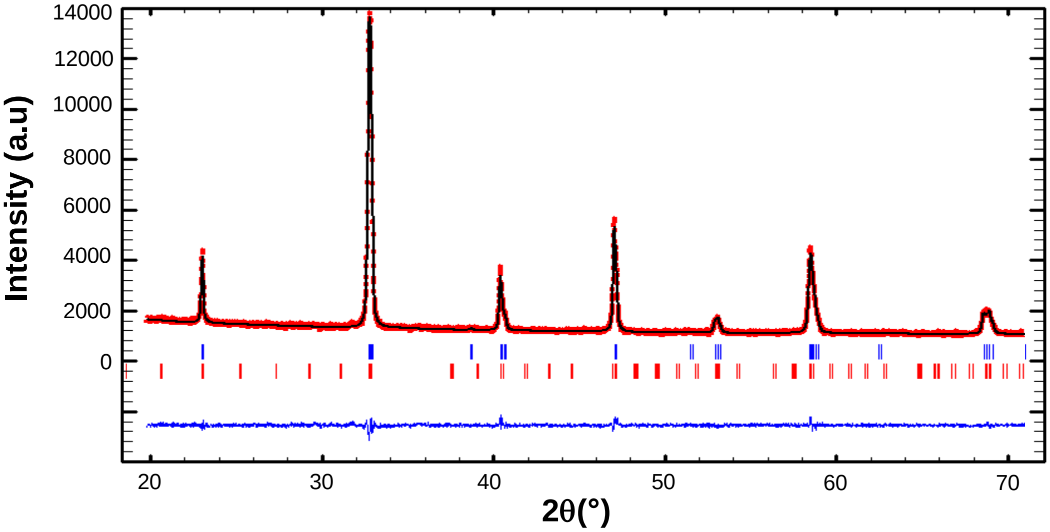

Figure C6. Graphical result of Rietveld refinement of $La_4BaCo_5O_{13\pm\delta}$ (x= 5) synthesized.

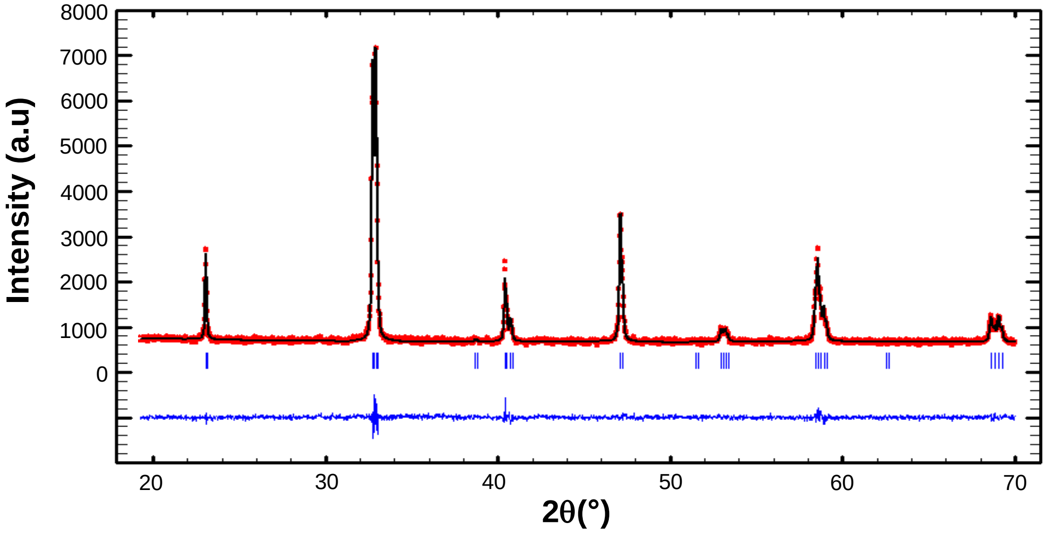

ANNEX D. Graphical result of Rietveld refinement of $La_4BaCu_{5-x}Co_xO_{13\pm\delta}$ + BCZY electrolyte

Figure D1. Graphical result of Rietveld refinement of the mixture LBCuCo2 + BCZY before heat treatment in air.

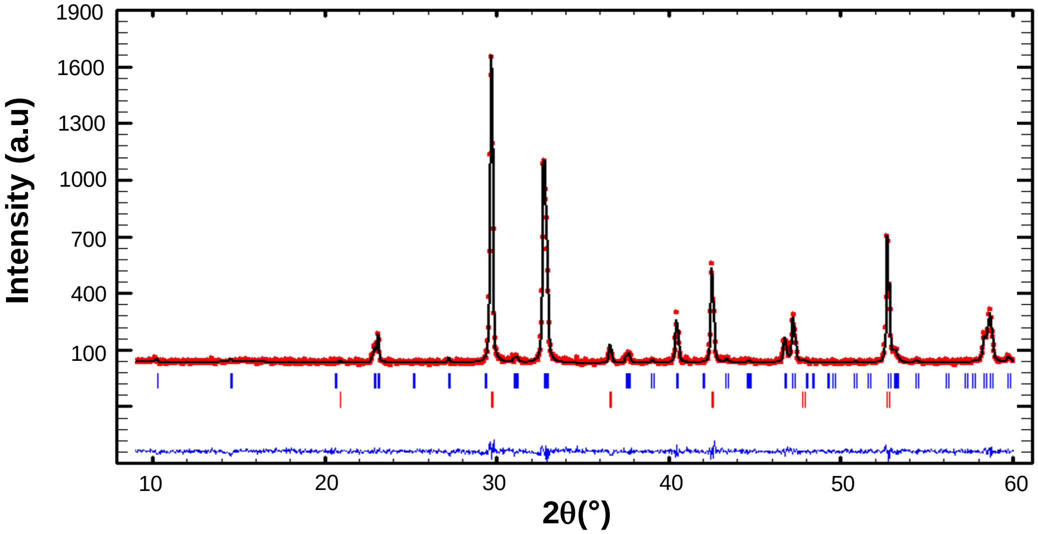

Figure D2.Graphical result of Rietveld refinement of the mixture LBCuCo2 + BCZY after heat treatment in air.

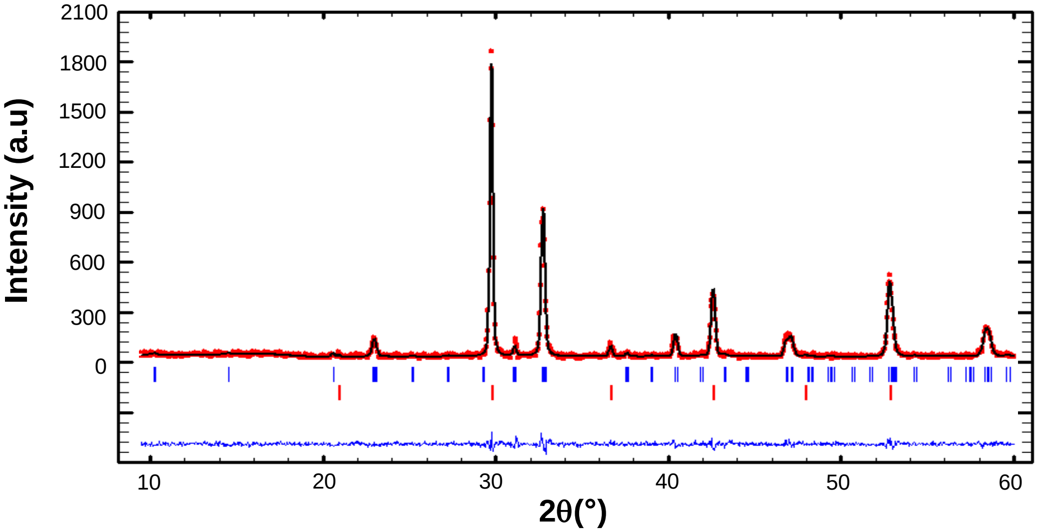

Figure D3.Graphical result of Rietveld refinement of the mixture LBCo + BCZY before heat treatment in air.

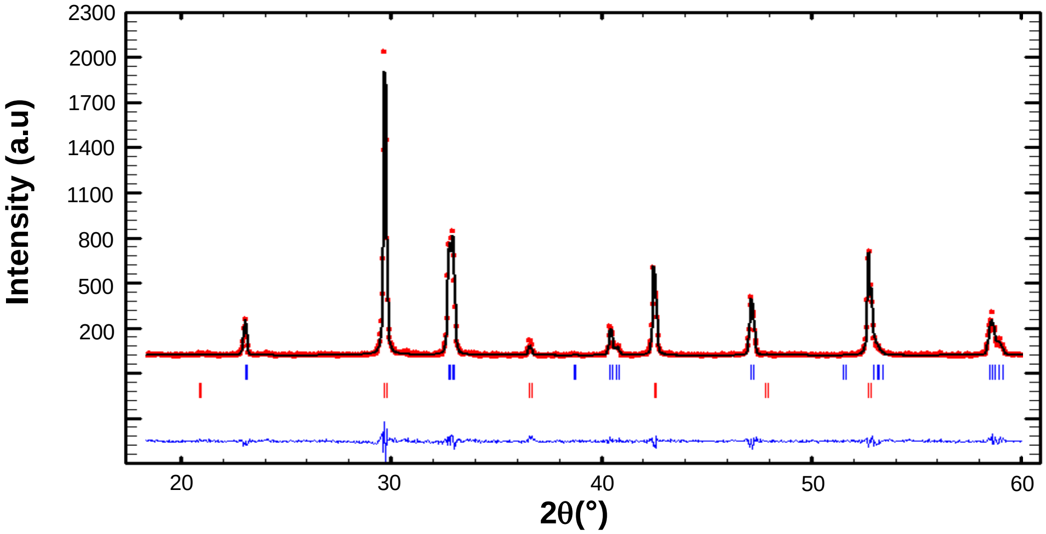

Figure D4.Graphical result of Rietveld refinement of the mixture LBCo + BCZY after heat treatment in air.

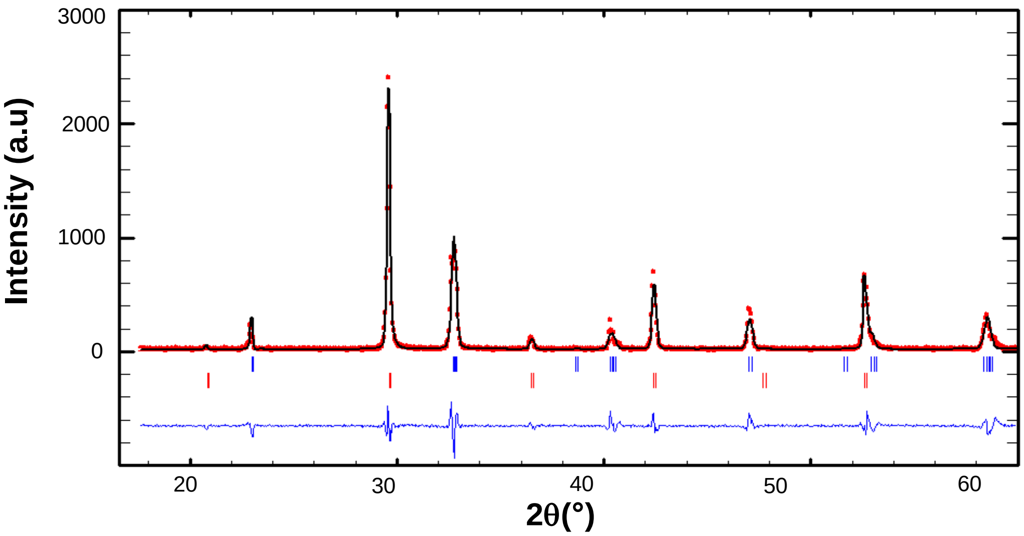

Figure D5. XRD patterns of $La_4BaCu_3Co_2O_{13\pm\delta}$ (x= 2) after treatment at 1050°C/5h in air.

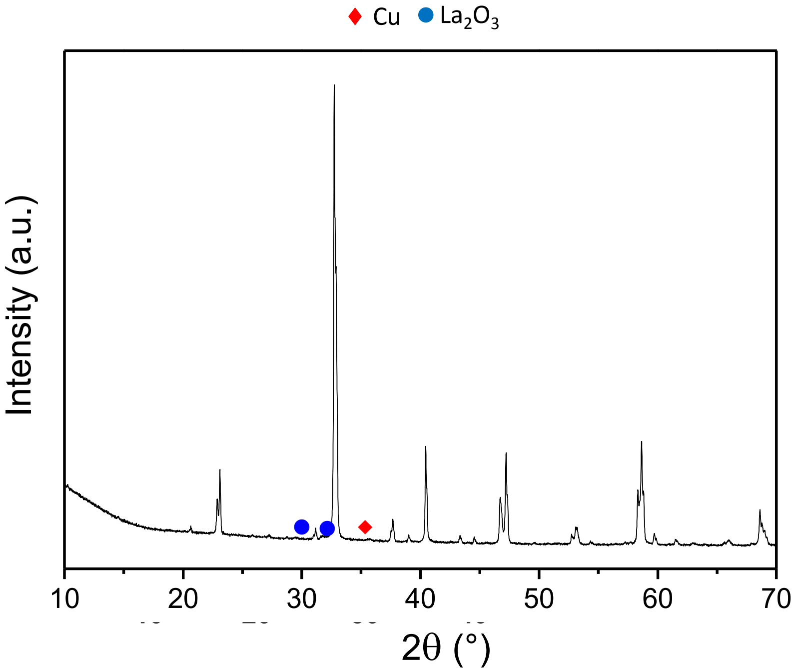

ANNEX E. Experimental and simulated impedance spectra measured at (a) 600, (b) 700, (c) 750 and (d) 800°C in air for LBCu cathode sintered at 950 °C. The numbers correspond to the logarithm of frequency.

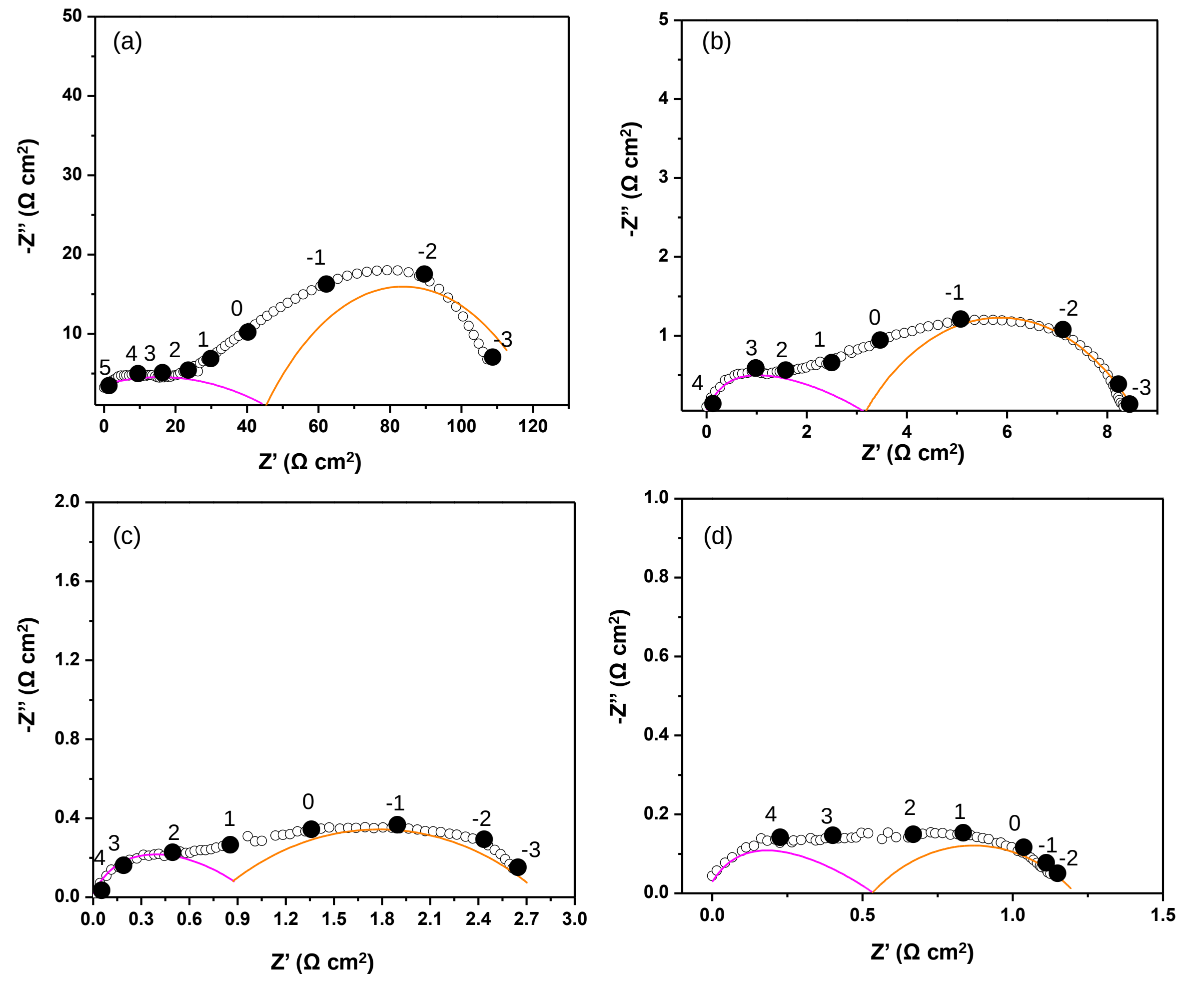

ANNEX F. Experimental and simulated impedance spectra measured at (a) 600, (b) 700, (c) 750 and (d) 800°C in air for LBCuCo2 cathode sintered at 950 °C. The numbers correspond to the logarithm of frequency.

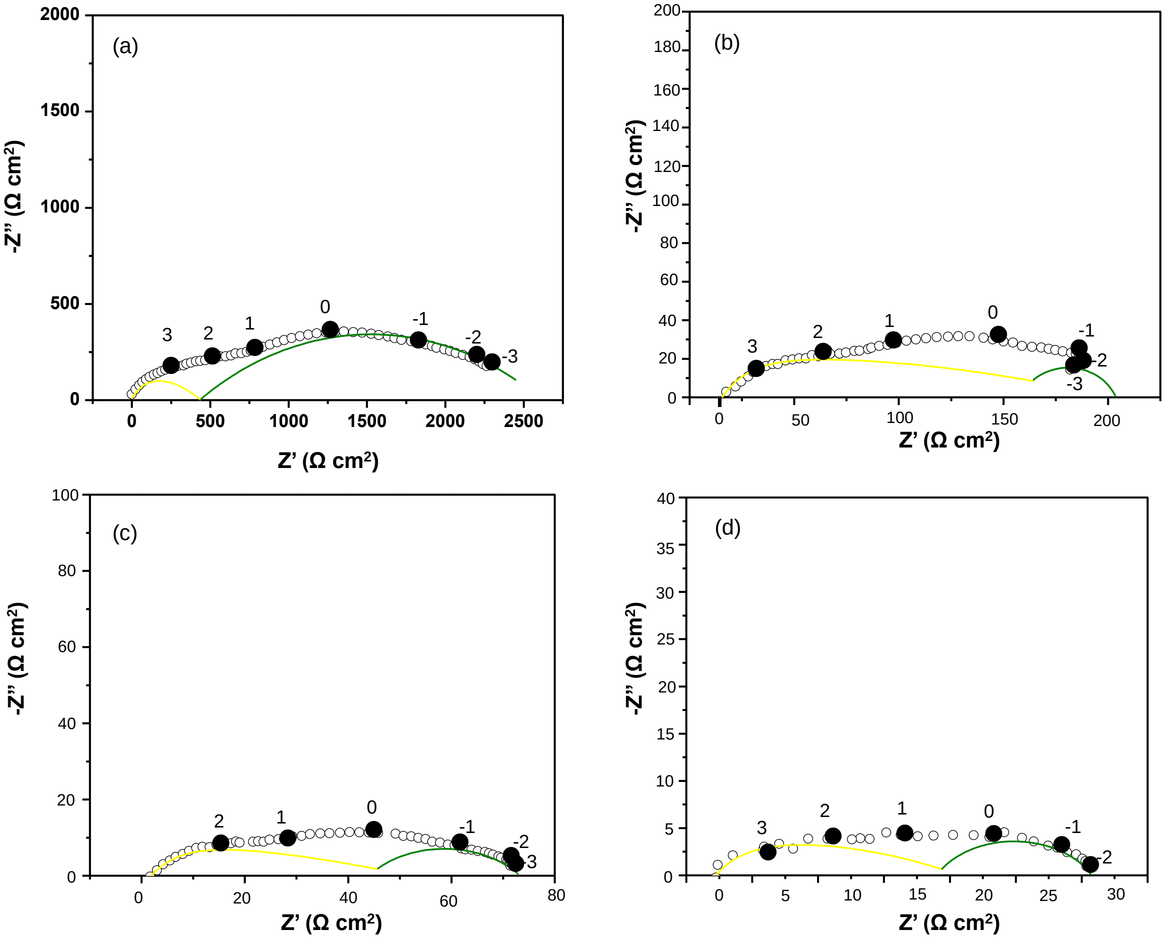

ANNEX G. Experimental and simulated impedance spectra measured at (a) 600, (b) 700, (c) 750 and (d) 800°C in air for LBCuCo2 cathode sintered at 1000 °C. The numbers correspond to the logarithm of frequency.

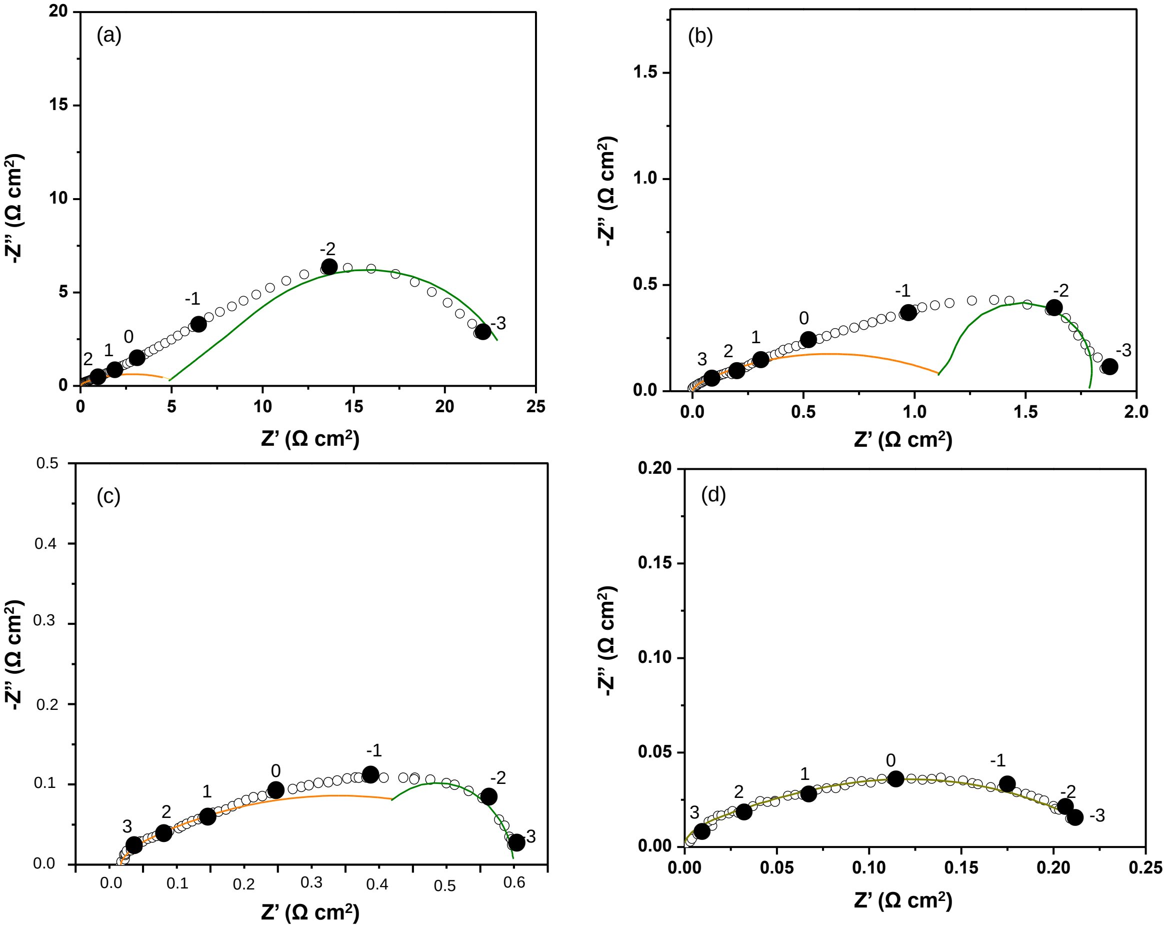

ANNEX H. Experimental and simulated impedance spectra measured at (a) 600, (b) 700, (c) 750 and (d) 800°C in air for LBCo cathode sintered at 950 °C. The numbers correspond to the logarithm of frequency.

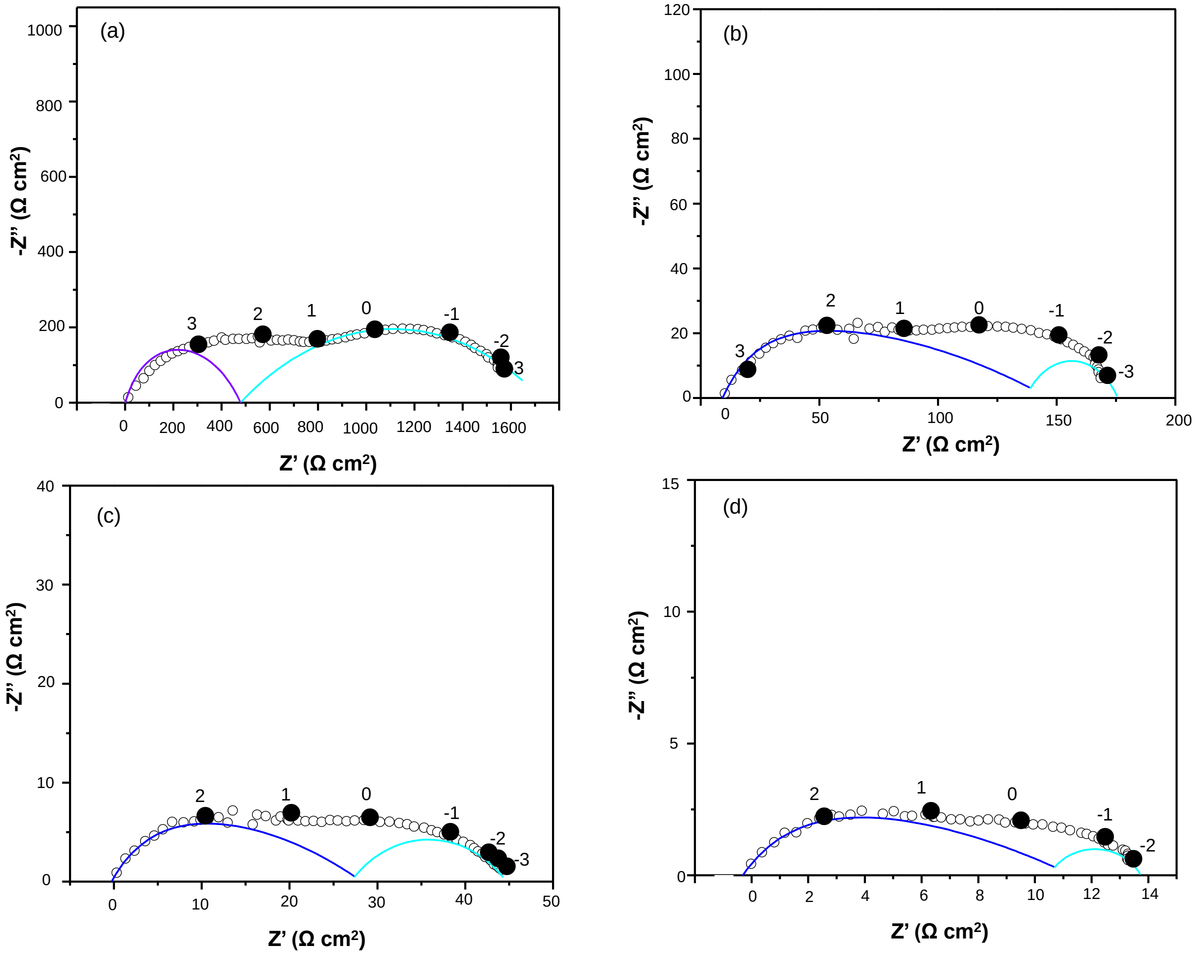

ANNEX I. Experimental and simulated impedance spectra measured at (a) 600, (b) 650, (c) 700 and (d) 750°C in air for LBCo cathode sintered at 1000 °C. The numbers correspond to the logarithm of frequency

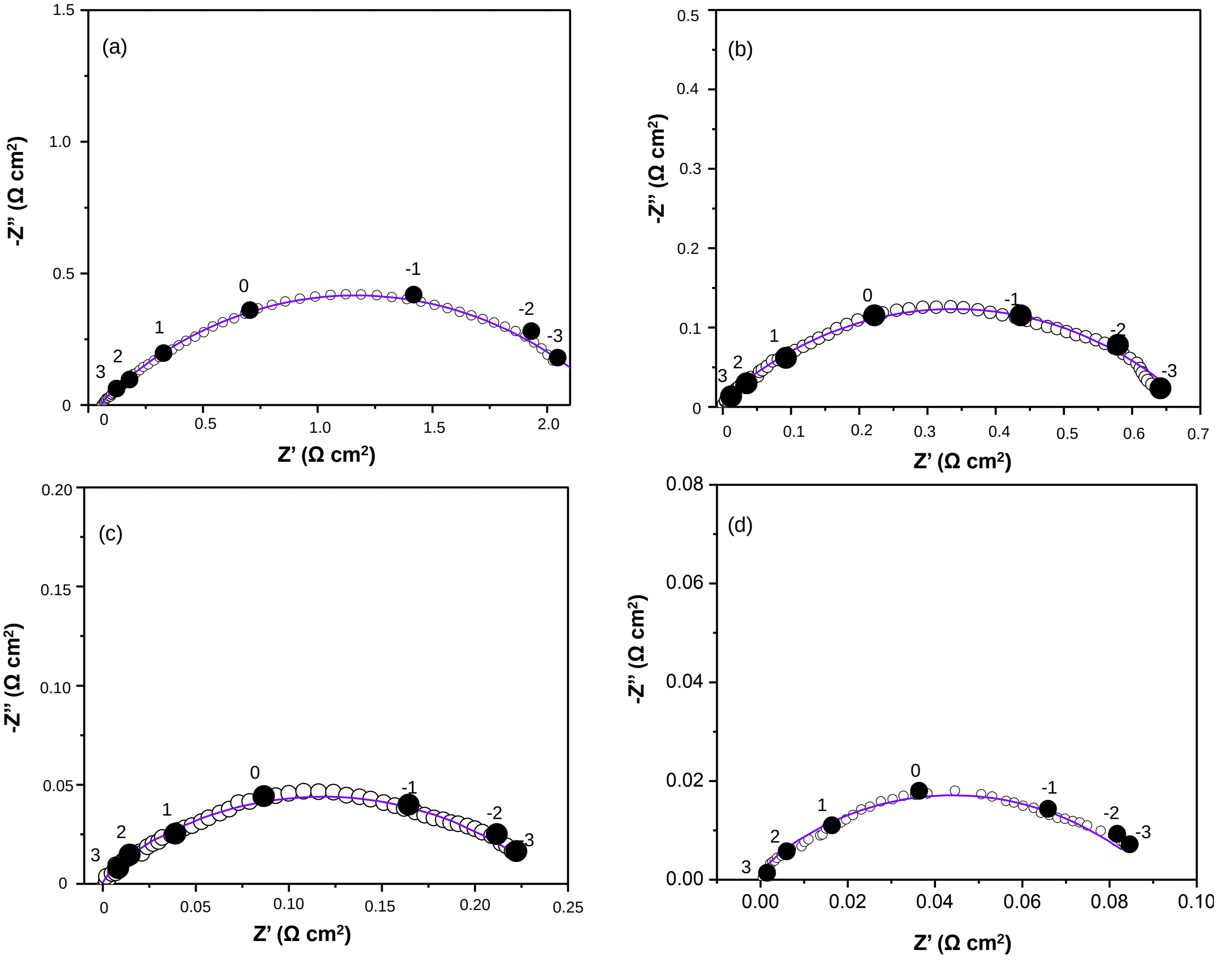

ANNEX J. Graphical results of Rietveld refinement of $La_4BaCu_{5-x}Mn_xO_{13\pm\delta}$ series sintered at 950 °C/5h

Figure J1. Graphical result of Rietveld refinement of $La_4BaCu_4MnO_{13\pm\delta}$ (x= 1) synthesized.

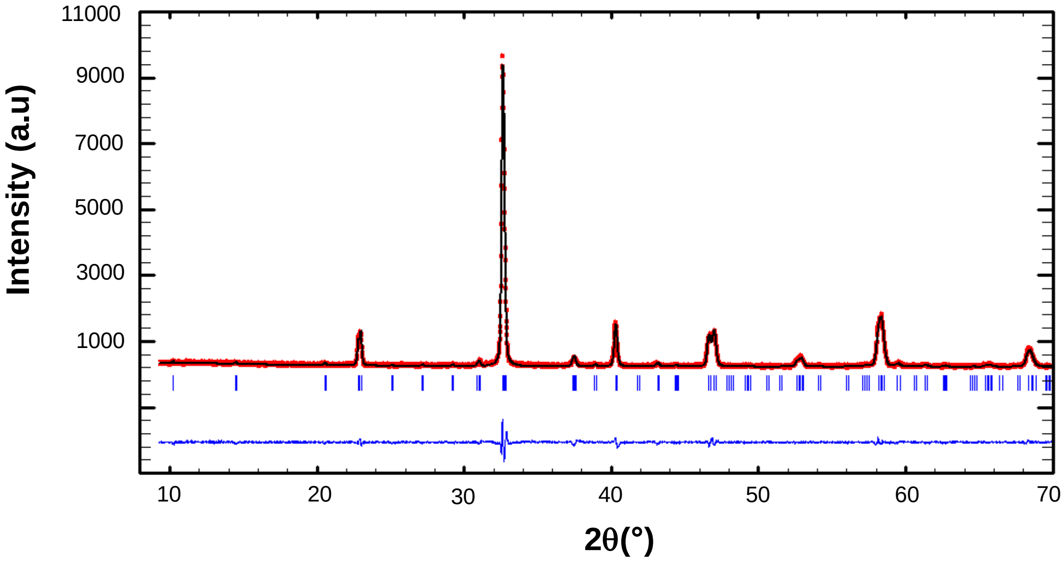

Figure J2. Graphical result of Rietveld refinement of $La_4BaCu_3Mn_2O_{13\pm\delta}$ (x= 2) synthesized.

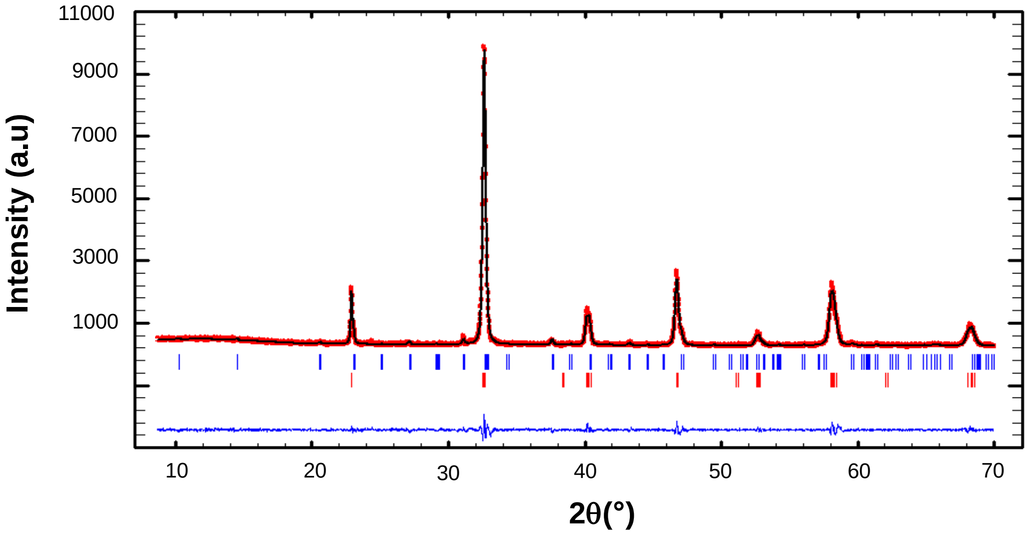

Figure J3. Graphical result of Rietveld refinement of $La_4BaCu_2Mn_3O_{13\pm\delta}$ (x= 3) synthesized.

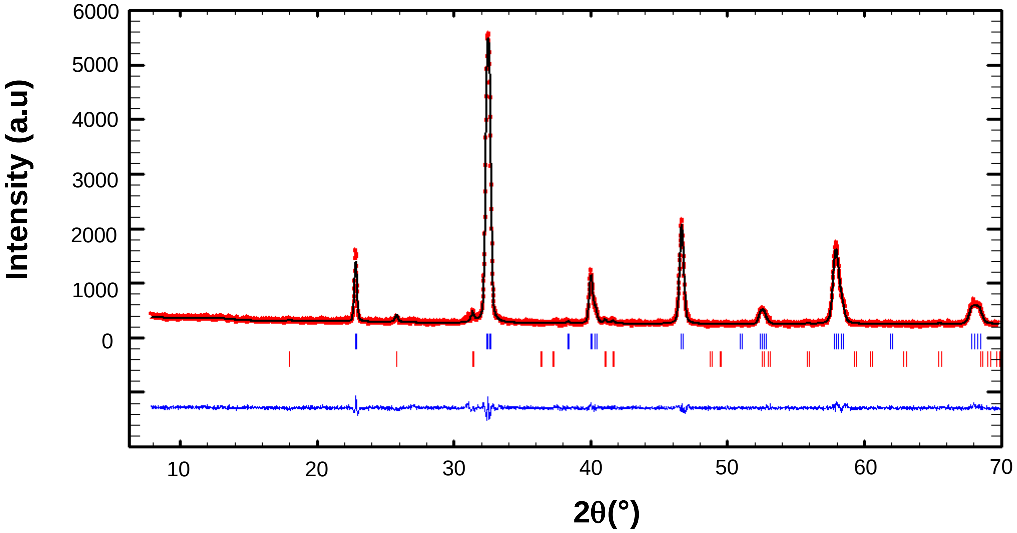

Figure J4. Graphical result of Rietveld refinement of $La_4BaCuMn_4O_{13\pm\delta}$ (x= 4) synthesized.

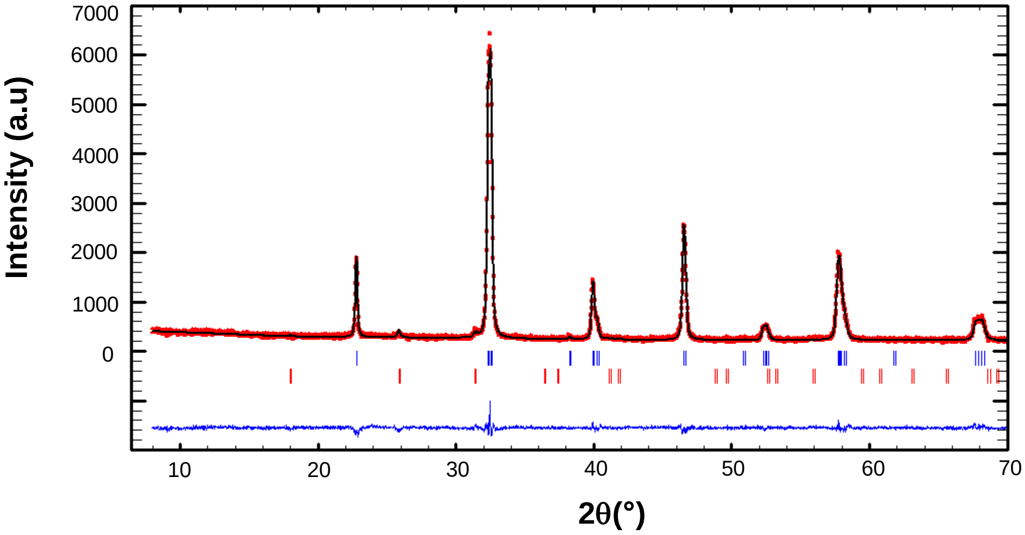

Figure J5. Graphical result of Rietveld refinement of $La_4BaMn_5O_{13\pm\delta}$ (x= 5) synthesized.

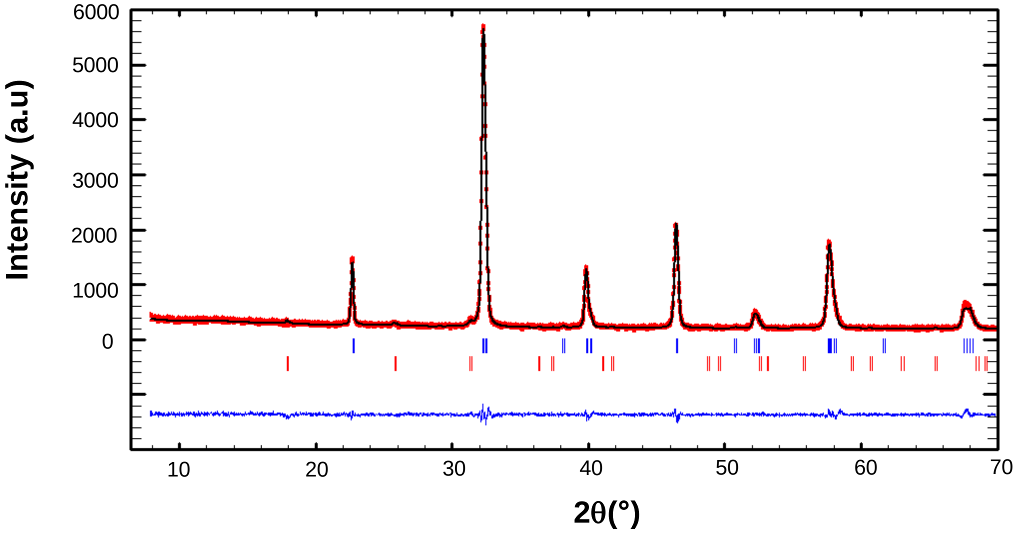

ANNEX K. Graphical results of Rietveld refinement of $La_4BaCu_{5-x}Mn_xO_{13\pm\delta}$ (x= 3, 4 and 5) sintered at 1000 °C/5h

Figure K1. Graphical result of Rietveld refinement of $La_4BaCu_2Mn_3O_{13\pm\delta}$ (x= 3) synthesized.

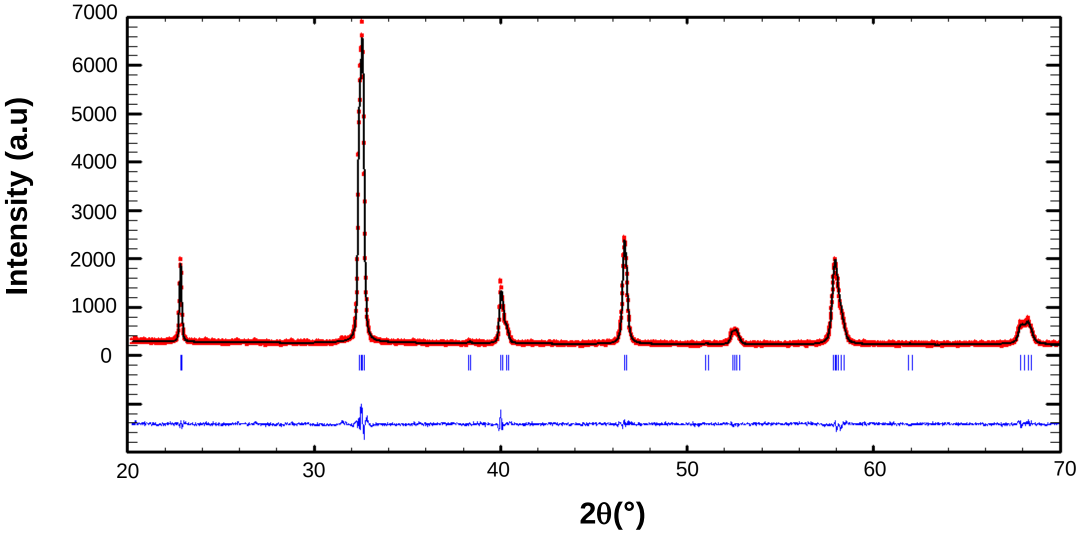

Figure K2. Graphical result of Rietveld refinement of $La_4BaCuMn_4O_{13\pm\delta}$ (x= 4) synthesized.

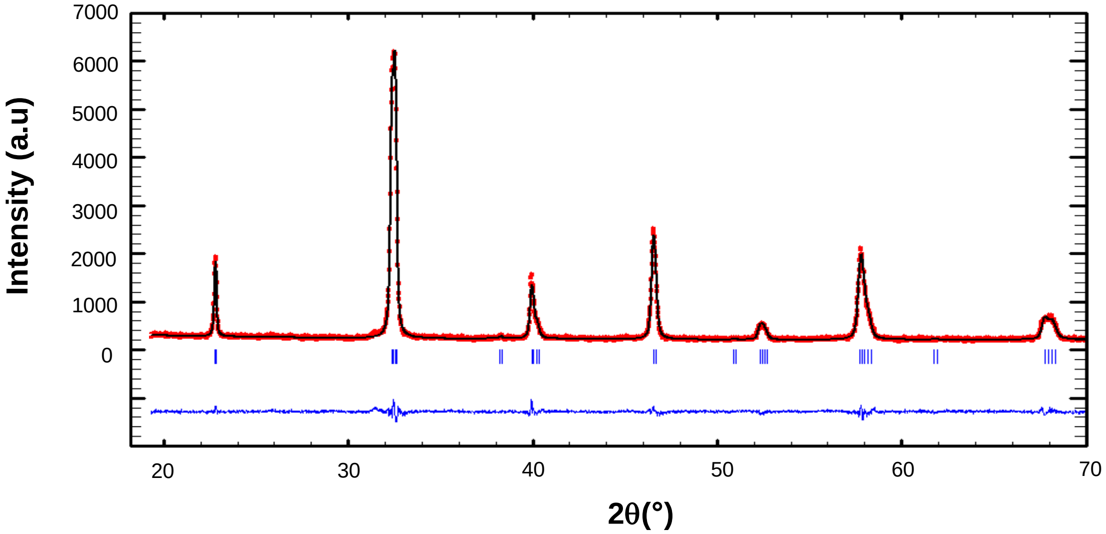

Figure K3. Graphical result of Rietveld refinement of $La_4BaMn_5O_{13\pm\delta}$ (x= 5) synthesized.

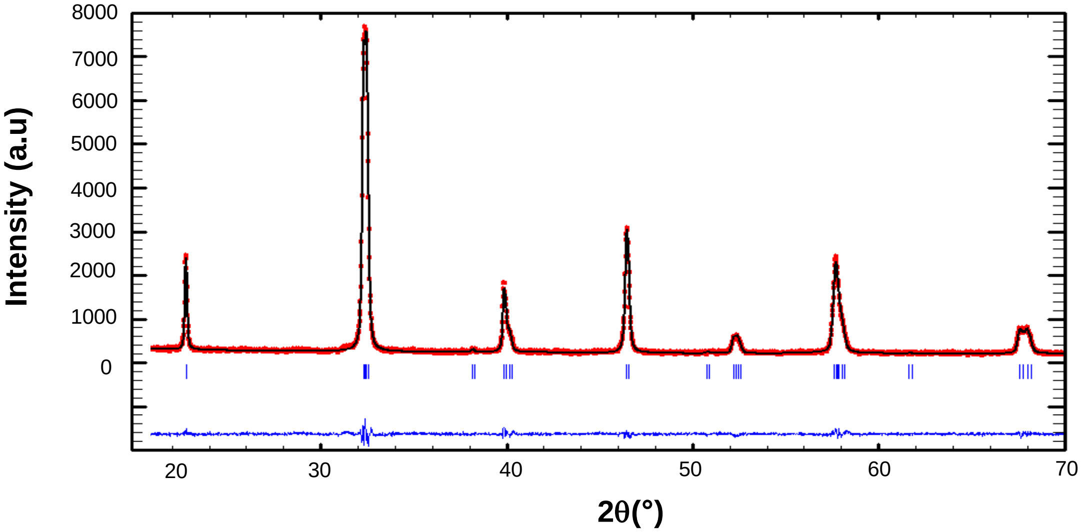

ANNEX L. Comparative graphics before and after heat treatment $La_4BaCu_{5-x}Mn_xO_{13\pm\delta}$ series in 3% H_2/N_2 at 850 °C/6 h.

Figure L1. XRD patterns of $La_4BaCu_3Mn_2O_{13\pm\delta}$ (x= 2) before and after reduction at 850°C/6h

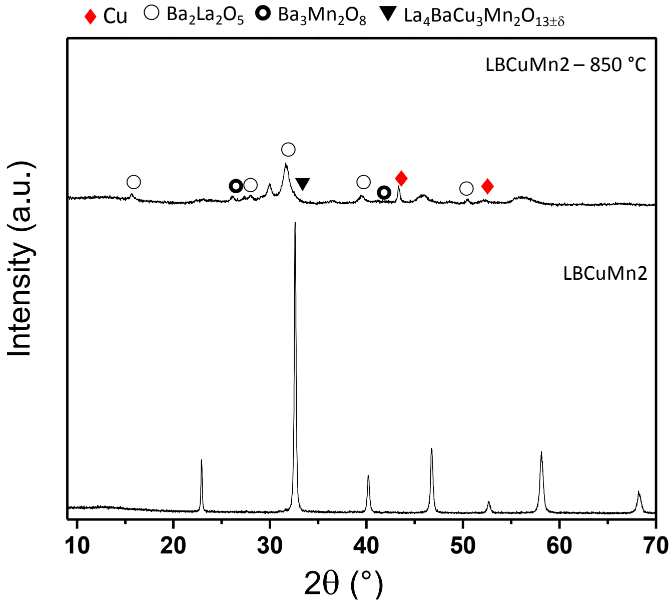

Figure L2. XRD patterns of $La_4BaMnO_{13\pm\delta}$ (x= 5) before and after reduction at 850°C/6h

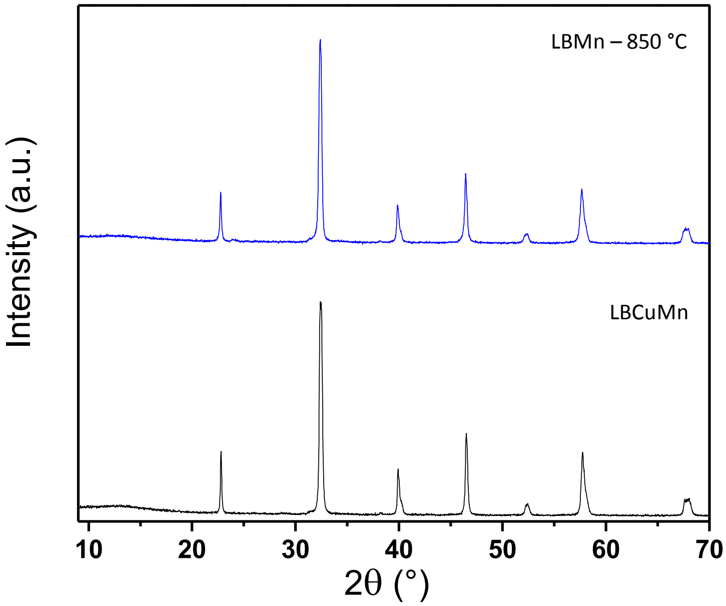

ANNEX M. Graphical result of rietveld refinement oF $La_4BaMn_5O_{13\pm\delta}$ (LBMn) in 3% H_2/N_2 at 850 °c/6 h

Figure M1. Graphical result of Rietveld refinement of $La_4BaMn_5O_{13\pm\delta}$ (x= 5) after heat treatment in 3% H_2/N_2 at 850 °C/6h.

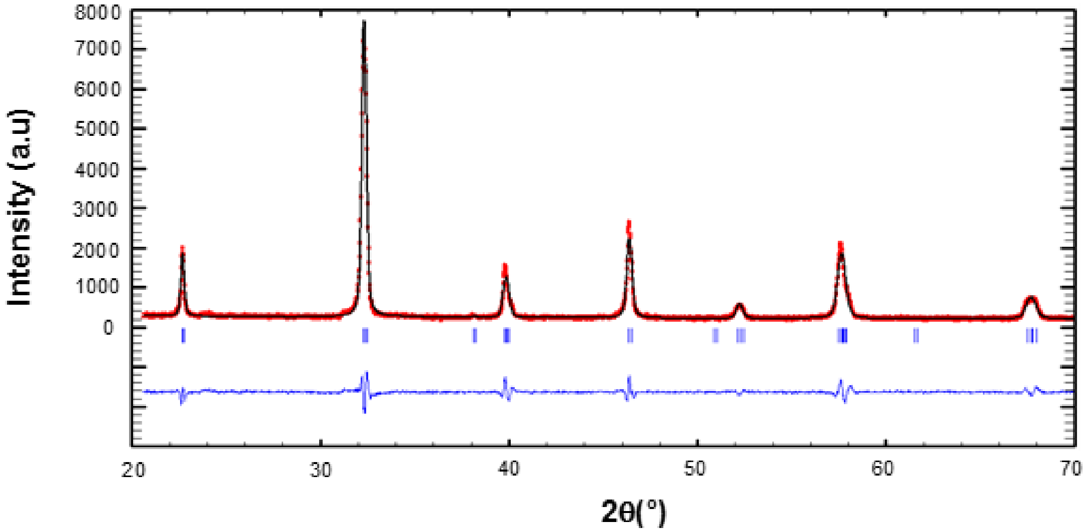

Table M1. Structural parameters of $La_4BaMn_5O_{13\pm\delta}$ (x= 5) before and after the test in 3% H2/N2, calculated by Rietveld refinement using XRD data.

	Before treatment	**After treatment**
		850 °C
	LBMn	LBMn-H2
a = b (Å)	5.5382(9)	5.521(3)
c (Å)	13.464(3)	13.59(1)
V (Å^3)	357.6(1)	358.9(4)
R_p	4.62	6.36
R_{wp}	6.07	8.32
χ^2	1.36	1.96

ANNEX N. Graphical result of Rietveld refinement of $La_4BaMn_5O_{13\pm\delta}$ (LBMn) chemical compatibility with BCZY electrolyte

Figure N1. Graphical result of Rietveld refinement of mixture LBMn + BCZY before heat treatment in air

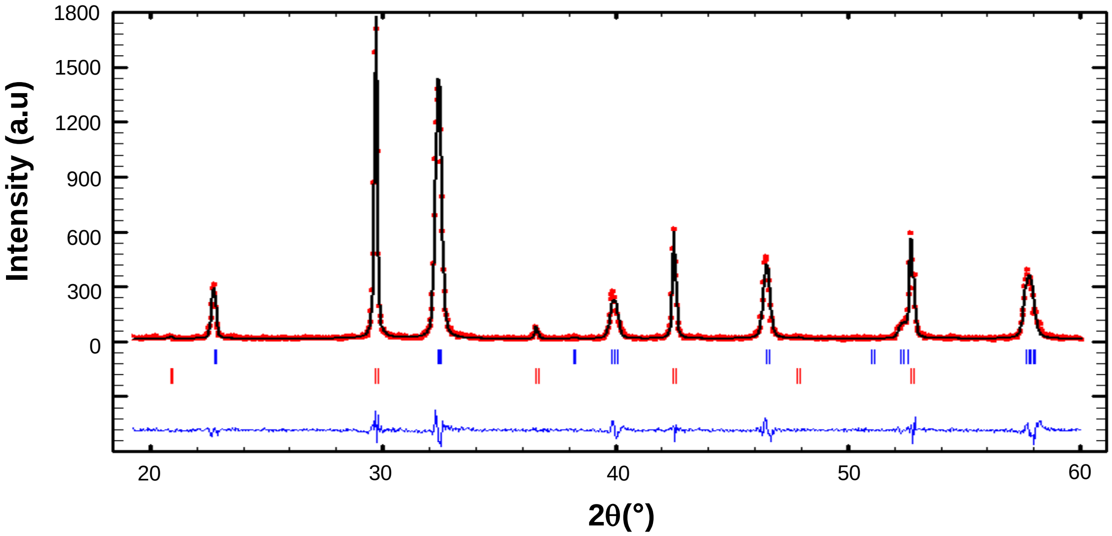

Figure N2. Graphical result of Rietveld refinement of mixture LBMn + BCZY after heat treatment in air